COMPUTATIONAL FLUID DYNAMICS ANALYSIS OF NON-COHESIVE SEDIMENT TRANSPORT IN OPEN CHANNEL FLOW

A Dissertation

by

HAN SANG KIM

Submitted to the Office of Graduate and Professional Studies of
Texas A&M University
in partial fulfillment of the requirements for the degree of

DOCTOR OF PHILOSOPHY

Chair of Committee,	Hamn-Ching Chen
Committee Members,	Kuang-An Chang
	Robert Randall
	Wilford Gardner
Head of Department,	Robin Autenrieth

August 2017

Major Subject: Civil Engineering

ABSTRACT

Predicting sediment transport has numerous implications in Civil Engineering and related fields. When there is excess sediment deposit in waterways, ships that move people and goods cannot navigate them. Loss of sediment that surrounds hydraulic support structures (e.g., bridge piers) may cause structural hazards. In the present dissertation research, computational fluid dynamics (CFD) was applied to improve the prediction capability of sediment transport in turbulent environments, with a focus on open channel flows.

The CFD tool used is FANS3D (Finite Analytic Navier-Stokes code for 3D flow), which solves the Reynolds-Averaged form of Navier-Stokes equations in general curvilinear coordinate systems. The code was coupled with sediment transport models to solve the hydrodynamics and the resulting transport phenomena. For flows in domains with complex geometries, the overset grid technique was adopted, wherein multiple blocks with different shapes and structures form the mesh. The wall function approach was implemented to account for roughness effects of the physical domain's boundary surfaces. After validation with experimental results, the coupled model was utilized in four practical applications: transport of suspended sediment in a channel bend, scour around abutment, backfilling of scour hole under a unidirectional flow, and scour around an offshore wind turbine support structure.

ACKNOWLEDGEMENTS

I would like to express my sincere gratitude for my advisor and committee chair, Dr. Hamn-Ching Chen, for his guidance, wisdom, and patience. I am very fortunate to have been taken under his wings to work on computational fluid dynamics with FANS3D which he developed. I am forever grateful.

I want to thank Dr. Kuang-An Chang for sharing his valuable insight on experimental designs, which helped me understand and interpret measurement data. It is also during my role as a TA in his classroom that I found joy and interest in teaching.

I would like to thank Dr. Robert Randall for teaching dredging, and how sediment transport can have very practical implications in the field. I have also much enjoyed my time at Haynes Coastal Engineering Laboratory.

I am also thankful to Dr. Wilford Gardner. His course on sediment dynamics provided invaluable knowledge critical for my dissertation. The laboratory section was especially helpful in understanding the physics.

Special thanks go to Dr. Jean-Louis Briaud, who has introduced me to the very interesting process of scour and backfilling. I am thankful for the opportunities.

Finally, I am very much indebted to friends and family, near and far, for their love and support.

CONTRIBUTORS AND FUNDING SOURCES

Contributors

This work was supervised by the dissertation committee consisting of Dr. Hamn-Ching Chen, Dr. Kuang-An Chang, and Dr. Robert Randall of the Department of Civil Engineering, and Dr. Wilford Gardner of the Department of Oceanography.

All work for the dissertation was completed by the student, under the advisement of Dr. Hamn-Ching Chen of the Department of Civil Engineering. Work involving scour and backfilling was completed under the advisement of Dr. Hamn-Ching Chen and Dr. Jean-Louis Briaud of the Department of Civil Engineering.

Funding Sources

The graduate study was made possible in parts by (in chronological order): Harold J. “Bill” Haynes ’46 Fellowship, Teaching Assistantship from the Department of Civil Engineering, Research Assistantship from the Department of Civil Engineering, term employment at Haynes Coastal Engineering Laboratory, Teaching Assistantship from the College of Engineering, funding from the Massachusetts Department of Transportation, funding from Korea Railroad Research Institute (KRRI), funding from Korea Institute of Civil Engineering and Building Technology (KICT), and the Graduate Teaching Fellows Program of the College of Engineering. The computational resources were provided by Texas A&M High Performance Research Computing Facility.

TABLE OF CONTENTS

Page

LIST OF FIGURES

Figure Page

LIST OF TABLES

1. INTRODUCTION

1.1. Motivation and Objective

In Civil Engineering and related fields, sediment transport is of a great interest due to its far-reaching implications. For instance, severe scour may lead to structural failure of bridges, and high turbidity in rivers and streams due to suspended particles may harm the aquatic ecosystem. For engineers to accurately predict the transport processes and take necessary measures, numerical simulation has become a widely-adopted approach.

However, limitations often exist for when the physical environment to be modeled involves a complex geometry. The reason is that many of the numerical tools available today are suitable only for geometrically simple domains, such as those with prismatic or cylindrical shapes. In such cases, the effectiveness of the numerical tools is confined to idealized problems.

Thus, through the dissertation research presented herein, a computational fluid dynamics (CFD) tool was developed to accurately simulate the flow and sediment transport in turbulent flow, with a focus on non-cohesive materials (e.g., sand). It was achieved by coupling the flow solver FANS3D (Finite Analytic Navier-Stokes code for 3D flow) with sediment transport models. Overset grid technique was adopted to represent complex physical domains with a set of geometrically simple blocks. The coupled tool was applied to analyze four practical engineering applications: transport of suspended sediment in a channel bend, scour around abutment, backfilling of scour hole under a unidirectional flow, and scour around an offshore wind turbine support structure.

1.2. Method

Here, the major steps taken to conduct and complete the present investigation are summarized. For each of these steps, the reader is guided to the part within this dissertation where in-depth discussions are further given.

1.2.1. Model Selection

The research effort was embarked upon with a literature review to survey the available sediment transport models. The goal was to identify the set of models that are appropriate or necessary for the problems to be considered. For instance, analysis of scour in front of a cylindrical pier would be best served by a model that describes the incipient motion of a particle based on the local shear stress, rather than the depth-averaged flow velocity. The literature surveyed and the models selected are discussed in Section 1.3 and Section 2, respectively.

1.2.2. Code Development

After selecting suitable models, they were coupled with FANS3D in the form of Fortran codes. The sediment transport modules were implemented as a set of subroutines that make use of the flow solutions in determining the sediment mechanics. Section 3 discusses the numerical methods in greater detail.

1.2.3. Validation

The coupled solver was validated with test cases. These are well-documented experimental studies with results that can be used to ensure that the numerical tool can accurately simulate the physics under a given flow environment and setup. The validations are presented in Section 4.

1.2.4. Simulation and Analysis

Four different engineering applications are discussed in Section 5: suspended sediment transport in channel bend, scour around two different abutment types, scour hole backfilling under a unidirectional flow, and scour around a hybrid offshore wind turbine support structure. In each of these applications, variations in the flow environment (e.g., abutment or pier geometry) and/or the sediment characteristics (e.g., particle size) helped understand sediment mechanics.

The applications were chosen on the basis of novelty and potential contributions. That is, those cases that effectively demonstrate the capabilities of the present numerical tool, but which haven't been discussed in the open literature, were considered. The graphical representations of the simulation results were generated using MATLAB and the CFD post-processor Tecplot.

1.3. Literature Review

Discussed below are an overview of sediment transport modeling from the literature. Application-specific materials are presented with greater details in Section 5.

1.3.1. Sediment Modeling Approaches

There are mainly two approaches for modeling sediment transport in a moving body of water: multi-phase models and diffusion models. The multi-phase models determine the interactions between the transport of sediment and hydrodynamics (Hsu et al., 2003; Hsu et al., 2004; Amoudry and Liu, 2009). They are widely adopted for many applications including sheet flow (Amoudry, 2009; Cheng and Hsu, 2014), suspended sediment transport (Muste et al., 2005; Jha et al., 2010; Shi and Yu, 2015), and particle dynamics modeling (Finn et al., 2016; Simeonov and Calantoni, 2012). While such studies provide well-resolved modeling results, they are computationally costly, especially when the flow environment is large and/or complex (Wu, 2008).

Diffusion models, on the other hand, treat sediment as a passive scalar, much like heat. In other words, it is assumed that the hydrodynamics is not affected by the presence of sediment particles in the water column (Villaret and Davies, 1995). In fact, Bagnold (1956) found that a sediment-fluid mixture will remain Newtonian for volumetric sediment concentrations less than 0.6. Since only one set of continuity and momentum equations is solved, diffusion models have an economic advantage over the multi-phase counterparts. Thus, for the present dissertation research, for which the goal is to bring contributions to the society with practical means of modeling sediment transport, diffusion models were adopted.

1.3.2. Brief History

In the early stages of sediment transport modeling, the flow and transport environments considered were relatively simple in nature, partly because the computing resources available then were extremely expensive by today's standard (Nordhaus, 2001). Kerssens et al. (1979) developed a one-dimensional model for prediction of the suspended sediment concentration in a stretch of river. The assumption was that the diffusion coefficient for momentum follows a parabolic profile over the depth. One-dimensional bed load was modeled by van Rijn (1984), who also investigated the effect of bed form roughness. On the other hand, Delft Hydraulics Laboratory (1980) simulated the downstream shift of a dredged channel due to both suspended and bed loads, and compared the results with a set of flume experiments. The flow was two-dimensional (width-averaged) and semi-empirical relations were used to correct the prediction models. Van Rijn (1981) developed a two-dimensional transport model to predict sediment concentration due to entrainment from the bed. Two-dimensional suspended transport was further investigated by Wang and Ribberink (1986), for a case where sediment is introduced at the inlet. They used a flume with holes on the bottom surface such that re-suspension does not occur.

With increase in computing performances, the modeling capacity also improved, aided in part by the concurrent advancement in turbulence modeling (Pope, 2000). Lin and Falconer (1995) simulated the sediment flux in estuarine waters using a depth-integrated finite difference model ULTIMATE QUICKEST. Wu et al. (2000) utilized a three-dimensional model FAST3D with k-ε turbulence closure to simulate channel bed

deformation. However, depth-integration was required for some quantities, such as the suspended load.

From the early 2000s and on, many researchers have utilized three-dimensional CFD models to simulate complex sediment transport processes which involve deformable boundaries. Jia et al. (2002) simulated the scour around a cylindrical pier in an open channel. The numerical model applied was CCHE3D, developed at the National Center for Computational Hydrodynamics and Engineering. Roulund et al. (2005) investigated the flow and scour around a circular pile with EllipSys3D. They also conducted a set of flume experiments and compared the results with the simulation. The authors noted that a single test required computational time spanning 2.5 months. Khosronejad et al. (2012) simulated scour around piers of different shapes using FSI-CURVIB and compared the result with experiments. Three different pier shapes were used: cylindrical, rectangular, and diamond. Open-source software solvers are also adopted, as in the work by Sumer et al. (2014), who used OpenFOAM with k-ω turbulence model to study backfilling due to waves.

Recently, technological advances such as parallel computing and graphics processing units (GPU) are increasingly being utilized for considerable reduction in computing time (Zhang and Jia, 2013; Fourtakas and Rogers, 2016; Hou et al., 2016; Sun and Xiao, 2016). It is predicted that these tools will make multi-phase approaches and higher-accuracy turbulence modeling more practical and accessible in the near future, thus contributing to our understanding of the complex physical phenomena.

2. GOVERNING EQUATIONS*

2.1. Hydrodynamics Equations

2.1.1. Reynolds-Averaged Navier-Stokes (RANS) Equations

FANS3D solves three-dimensional unsteady, incompressible RANS equations in non-staggered, general curvilinear coordinate system. The governing equations in tensor form are as follows (Wu et al., 2000):

$$\frac{\partial u_i}{\partial x_i} = 0 \tag{2.1}$$

$$\frac{\partial u_i}{\partial t} + \frac{\partial \left(u_i u_j\right)}{\partial x_j} = -\frac{1}{\rho}\frac{\partial p}{\partial x_i} + \frac{1}{\rho}\frac{\partial \tau_{ij}}{\partial x_j} + F_i, \tag{2.2}$$

where u_i = mean velocities; ρ = fluid density; p = pressure; τ_{ij} = deviatoric stresses; and F_i = external force (e.g., one due to the gravity). The deviatoric stresses are defined as:

$$\tau_{ij} = \rho(\nu + \nu_t)\left(\frac{\partial u_i}{\partial x_j} + \frac{\partial u_j}{\partial x_i}\right) - \frac{2}{3}\delta_{ij}k, \tag{2.3}$$

where ν = kinematic viscosity; ν_t = eddy viscosity; δ_{ij} = Kronecker delta; and k = turbulent kinetic energy.

In the current investigation, the standard k-ε turbulence model by Rodi (1993) was adopted. In this model, the eddy viscosity is:

$$\nu_t = c_\mu \frac{k^2}{\varepsilon}, \tag{2.4}$$

Here, the turbulent kinetic energy k and the dissipation rate ε are determined from Eqs. (2.5) and (2.6), respectively.

$$\frac{\partial k}{\partial t}+\frac{\partial\left(u_j k\right)}{\partial x_j}=\frac{\partial}{\partial x_j}\left[\left(\nu+\frac{\nu_t}{\sigma_k}\right)\frac{\partial k}{\partial x_j}\right]+G-\varepsilon \tag{2.5}$$

$$\frac{\partial \varepsilon}{\partial t}+\frac{\partial\left(u_j \varepsilon\right)}{\partial x_j}\frac{\partial}{\partial x_j}\left[\left(\nu+\frac{\nu_t}{\sigma_\varepsilon}\right)\frac{\partial \varepsilon}{\partial x_j}\right]+\left(c_{\epsilon 1}G-c_{\epsilon 2}\varepsilon\right)\frac{\varepsilon}{k} \tag{2.6}$$

where G = production of k. The standard values are used for the model coefficients: σ_k = 1.0; σ_ε = 1.3; c_μ = 0.09; $c_{\epsilon 1}$ = 1.44; and $c_{\epsilon 2}$ = 1.92.

2.1.2. Wall Function Approach

The wall function approach outlined in Wu et al. (2000) was adopted to incorporate the effects of the roughness elements (i.e., sediment particles on the bed). Here, the first grid point away from a wall surface in the mesh is placed within the logarithmic region, based on an a priori calculation with the characteristic length and velocity (White, 2002). In calculating the flow, Eq. (2.7) is enforced through an iterative method to obtain the local velocity components at the wall function grid level.

$$\frac{U}{u_\tau}=\frac{1}{\kappa}\ln E y^+, \tag{2.7}$$

where U = total magnitude of the velocity parallel to the bed surface ($U=\sqrt{u_i u_i}$); κ = von Kármán constant; y^+= viscous length; and $E = e^{[\kappa(B-\Delta B)]}$. The constant B has the value of 5.2 and ΔB was determined by Cebeci and Bradshaw (1977) as a function of the roughness height k_s. Finally, the kinetic energy k and the dissipation rate ε are specified by:

$$k=\frac{u_\tau^2}{c_\mu^{1/2}} \tag{2.8}$$

$$\varepsilon = \frac{u_\tau^3}{\kappa y} \tag{2.9}$$

The wall function approach has an added benefit of reducing the computational cost by enabling one to use a larger grid spacing compared to when other turbulence models such as two-layer model are used. This can be explained in terms of boundary layer theory. For two-layer model, the idea is to place a set of grid points within the viscous sublayer ($y^+ \approx 5$) to resolve near-wall turbulence using the one-equation model (Chen and Patel, 1988). On the other hand, the wall function requires the first grid point away from the wall to be placed farther from the wall, in the logarithmic region ($y^+ \approx 50$). To capture the difference in a more physical sense, the first grid spacing away from the wall are compared in Table 2.1 for select flow velocities. The estimated distances y^+ were determined following White (2002). The roughness was assumed to be zero (smooth surface) and the characteristic length was set equal to 1 m.

Table 2.1. Comparison of first grid spacing for two-layer model and wall function.

Flow Velocity	Reynolds Number	Two-Layer ($y^+ \approx 5$)	Wall Function ($y^+ \approx 50$)
0.1 m/sec	89,000	1.00 mm	10.00 mm
0.2 m/sec	178,000	0.55 mm	5.50 mm
1.0 m/sec	890,000	0.13 mm	1.30 mm

The wall function approach, however, is not without disadvantages. It has been argued that its accuracy is questionable when there is a strong pressure gradient (Pope,

2000). In such cases, other turbulence modeling schemes that resolve the physics more closely will be required, such as k-ω or large eddy simulation. However, for the present investigation's purpose of conducting practical simulations of sediment transport processes in the engineering scale, the wall function approach as presented was deemed feasible. In fact, the wall function approach has been utilized by other researchers in similar studies. For example, Wu et al. (2000) adopted the wall function approach to investigate the sediment transport around a 180° channel bend. When compared with the experiment conducted under the same condition, the predicted bed elevations and secondary flow velocity showed good agreement. The study by Zhang et al. (2010) on local scour around a submerged vertical circular cylinder also used the wall function approach. They noted that this approach increased the computational efficiency by avoiding use of fine mesh.

2.2. Suspended Sediment Transport Equations

As discussed in Section 1.3, the sediment suspended in water column was treated as a passive scalar in terms of concentration. The following equation, in tensor notation, is used to describe the transport of this quantity (Wu et al., 2000):

$$\frac{\partial c}{\partial t} + \frac{\partial}{\partial x_j}\left[\left(u_j - \omega_s \delta_{j3}\right)c\right] = \frac{\partial}{\partial x_j}\left[\left(\nu + \frac{\nu_t}{\sigma_c}\right)\frac{\partial c}{\partial x_j}\right] \tag{2.10}$$

where c = volumetric suspended sediment concentration; ω_s = particle settling velocity; and σ_c = Schmidt number. In this study, 1.0 was used as the value of σ_c.

This approach calls for appropriate boundary conditions for the free surface and the bottom boundary. At the free surface, where the fluid forms a boundary with the air above, there is no flux in the vertical direction (Wu et al., 2000). This relationship is expressed with Eq. (2.11).

$$\left(\nu + \frac{\nu_t}{\sigma_c}\right)\frac{\partial c}{\partial z} + \omega_s c = 0 \tag{2.11}$$

At the bottom boundary, the flow and turbulence may disturb the sediment particles on the bed and produce an upward flux (source), but the physics also dictates that the particles eventually settle to the bed (sink). Following van Rijn (1987), the equilibrium sediment concentration c_* was prescribed at the bottom boundary:

$$c_* = 0.015\frac{d_{50}T^{1.5}}{aD_*^{0.3}}, \tag{2.12}$$

where d_{50} = sediment median diameter; T = non-dimensional excess bed shear stress; a = thickness of the bed load layer; and D_* = non-dimensional particle diameter.

2.3. Morphodynamics Equations

FANS3D was also coupled with a morphologic model, with only the bed load transport mode considered (i.e., elevation change due to suspended load was not incorporated). The bed load transport model by Roulund et al. (2005) was adopted as the main framework, with the slope failure model by Khosronejad et al. (2011).

The balance of bed load flux within a control volume is modeled with the Exner equation (Fortunado and Oliviera, 2007):

$$\frac{\Delta z}{\Delta t} = \frac{1}{(1-n)} \nabla \cdot \boldsymbol{q}_b^*, \tag{2.13}$$

where Δz = bed elevation change over the time step Δt; n = porosity of the sediment particle; and $\boldsymbol{q}_b^*$ = volumetric bed load flux. The bed load flux per unit width $\boldsymbol{q}_b$ is determined following Engelund and Fredsøe (1976):

$$\boldsymbol{q}_b = \frac{1}{6} \pi d_{50}^3 \frac{P_{EF}}{d_{50}^2} \boldsymbol{U}_b, \tag{2.14}$$

where P_{EF} = percent of particles in motion in the surface of the bed; $\boldsymbol{U}_b$ = mean transport velocity of a particle moving as bed load. The following expressions are used to compute P_{EF} and other associated terms:

$$P_{EF} = \left[1 + \left(\frac{\frac{1}{6}\pi \mu_d}{\theta - \theta_c} \right)^4 \right]^{-1/4} \tag{2.15}$$

$$\theta = \frac{\boldsymbol{U}_f^2}{(s-1) g d_{50}} \tag{2.16}$$

$$\theta_c = \theta_{c0}\left(\cos\beta\sqrt{1-\frac{\sin^2\alpha\tan^2\beta}{\tan^2\phi}}-\frac{\cos\alpha\sin\beta}{\tan\phi}\right), \tag{2.17}$$

where μ_d= dynamic friction coefficient with the value of 0.51; θ = Shields parameter; $\boldsymbol{U}_f$ = friction velocity; s = specific gravity of the sediment; g = gravitational acceleration; and θ_c = critical value of θ for incipient motion. Note that the right-hand side of Eq. (2.17) describes the correctional treatment applied to the critical Shields parameter for a horizontal bed θ_{c0}, to account for the local bed geometry (e.g., sloping scour hole) and the orientation of the flow velocity. Here, β = the local bed slope; α = angle between the near-bed velocity vector and the direction of the bed slope; and ϕ = the angle of repose associated with the sediment particle. To determine the mean transport velocity of sediment particle $\boldsymbol{U}_b$, it is necessary to solve the system of Eqs. (2.18-2.21) that describe the balance of forces acting on an individual particle, depicted in Fig. 2.1.

$$F_D\cos\psi_1 + W\sin\beta\cos(\alpha-\psi) - (W\cos\beta)\mu_d = 0 \tag{2.18}$$

$$F_D\sin\psi_1 - W\sin\beta\sin(\alpha-\psi) = 0 \tag{2.19}$$

$$U_r\sin\psi_1 - \alpha U_f\sin\psi = 0 \tag{2.20}$$

$$U_r\cos\psi_1 - aU_f\cos\psi + U_b = 0, \tag{2.21}$$

where F_D = drag force; W = gravitational force; ψ = angle between the direction of the sediment particle $\boldsymbol{U}_b$ and the fluid velocity $\boldsymbol{U}$; ψ_1 = angle between $\boldsymbol{U}_b$ and $\boldsymbol{U}_r$, the flow velocity relative to the particle. The following equations are also required:

$$F_D = \frac{1}{2}\rho c\frac{\pi}{4}d_{50}^2U_r^2 \tag{2.22}$$

$$W = \frac{1}{6}\pi\rho g(s-1)d_{50}^3 \tag{2.23}$$

$$c = \frac{4\mu_s}{3\alpha^2\left(\frac{1}{2}\theta_{c0}\right)} \tag{2.24}$$

$$U_r = U - U_b = aU_f - U_b, \tag{2.25}$$

where c = force coefficient; $\mu_s = \tan\phi$; and α = constant of value 10. Eqs. (2.18-2.21) are solved iteratively using a multi-dimensional Newton-Raphson scheme with Jacobian matrix. In the current research, particular attention was given to selection of the appropriate initial guesses of the parameters to facilitate convergence (Chapra, 2008); after the first time step, the converged solutions from the previous time step were used as the initial guesses for the new iteration.

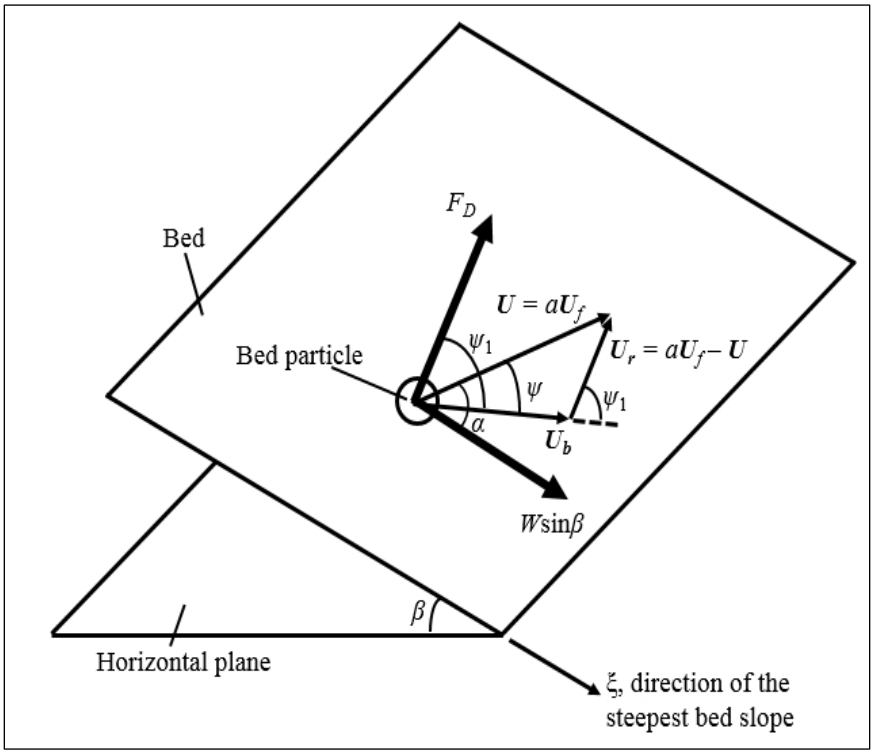

Fig. 2.1. Schematic of forces and velocities experienced by sediment particle (Roulund et al., 2005).

It is also necessary to ensure that the angle of repose inherent to the sediment type is not exceeded anywhere in the domain. Thus, the sand slide correction scheme by Khosronejad et al. (2011) was adopted. The algorithm first computes the slope between the central cell p and its neighbors. If any of these slopes exceeds the angle of repose, small volumes of sediments are exchanged among the same neighboring cells while maintaining the conservation of mass. This process is repeated until the following conditions are met:

$$\frac{\left(z_{bp} + \Delta z_{bp}\right) - \left(z_{bi} + \Delta z_{bi}\right)}{\Delta l_{pi}} = \tan\phi \tag{2.26}$$

$$A_{hp}\Delta z_{bp} - \sum_{i=1}^{4} A_{hi}\Delta z_{bi} = 0 \tag{2.27}$$

where z_{bp} = bed elevation at the center of the cell p; z_{bi} = bed elevation at the neighboring cells' center points; Δz_{bp} and Δz_{bi} = the correction height applied to the aforementioned points, respectively; Δl_{pi} = horizontal distance between p and its neighbor i; and A_{hp} and A_{hi} = the areas of the cells p and i, respectively. In this investigation, the angle of repose was set to 32° following Messer et al. (1916).

3. NUMERICAL MODELING

3.1. Finite Analytic Method

FANS3D is a general CFD program developed based on the finite analytic method of Chen et al. (1990), with the hybrid SIMPLER/PISO velocity-pressure coupling by Chen and Korpus (1993) and Pontaza et al. (2005). The current investigation used the k-ε turbulence model but the solver also has the capability to calculate flow with large eddy simulation (Huang et al., 2011) and detached eddy simulation (Chen and Chen, 2016). It has been largely employed in offshore engineering applications, such as vortex-induced vibration of pipelines (Huang et al., 2011), hull slamming (Chen and Chen, 2015), and violent free surface (Chen and Chen, 2016). Other applications more relevant to this dissertation include cohesive soil scour around an array of piers (Chen, 2002), cohesive soil scour around an abutment (Chen, 2008), and suspended sediment transport (Kim and Chen, 2014) in channel bend.

The essence of the finite analytic method is that the analytic solutions of the locally linearized governing equations are incorporated in obtaining the numerical solutions. This leads to advantages in accuracy and convergence rate over other discretization schemes. In applying the method, the computational domain is first discretized into numerical elements, as depicted in Fig. 3.1. Then, in each of these subdomains, the analytic solutions of the governing equations are obtained at the interior node P with the separation of variables technique using the dependent variables at the exterior points. In turn, algebraic equations relating the analytic solutions at P to the values at the subdomain's boundaries

are established. In the current work, the 19-point scheme by Chen et al. (1995) was used. For more detailed description of the method, the reader is also referred to Chen and Chen (1984) and Chen et al. (1990).

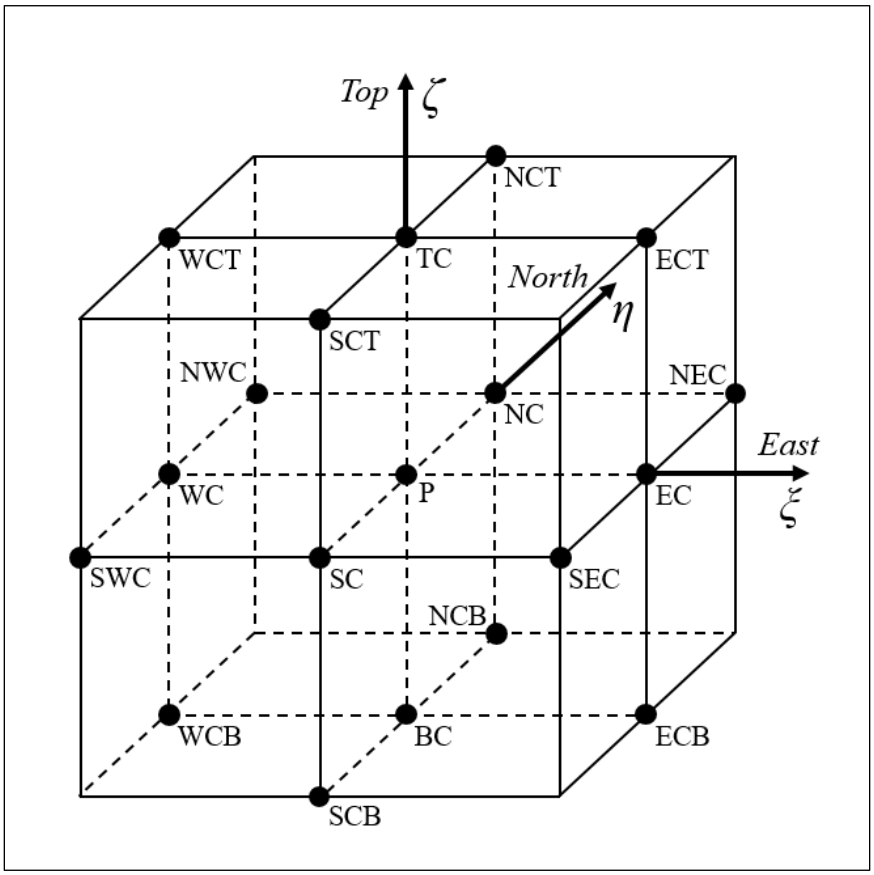

Fig. 3.1. Numerical element for the 19-point finite analytic method (Chen et al., 1995).

3.2. Overset Grid Technique

With overset grid technique, the physical domain is decomposed into geometrically simple blocks, which form the CFD mesh as a whole. The flow solutions obtained within each of the blocks are then transferred to others through interpolation.

A major advantage of this technique is that it allows one to employ local block geometries that best suit different parts of the physical domain being analyzed. For instance, assume that scour is simulated around a cylindrical pier placed inside a rectangular flume. In such case, the appropriate approach would be to model the pier with a cylindrical block and the flume with a prismatic block, with the former embedded in the latter. This will facilitate specification of boundary conditions: the inner radial surface of the pier block will have the no-slip condition, while the outer surface will be used for interpolation with the surrounding block. The key is to understand the characteristics of the flow field to be analyzed and recognize which boundary conditions are needed.

With overset grid technique, it is critical to achieve high-accuracy interpolation between blocks. In the present investigation, PEGASUS, a pre-processor developed originally in the 1980s for aerodynamics simulation, was used to set up the interpolation scheme (Benek et al., 1985). PEGASUS is particularly useful in automated hole-cutting and linking of multiple blocks according to the user input (Suhs, 2002). By specifying the block dimensions and the indices of the surfaces through which information is transferred, PEGASUS generates the interpolating protocol. This, in turn, directs the communications among the different grid points that are linked to one another. The complete sequence for generating a mesh with the overset grid technique is briefly described below.

i. Define geometry.

First, one needs to define the geometry of each of the blocks that together represent the physical flow domain. For example, to generate a mesh for simulation of flow around a pier in a channel, the geometry and number of grid points need to be specified for the pier and channel blocks separately. In the present investigation, case-specific Fortran codes were used for this Step.

ii. Improve spacing.

To obtain numerically stable solutions and to satisfy certain boundary conditions near the surfaces (e.g., wall function), the grid spacing for each block is modified as necessary. This task can be incorporated into the previous step.

iii. Assign block identifications.

For PEGASUS to recognize different components of the mesh, each block must be identified with a unique name. The file containing the names and geometries of the blocks are read by PEGASUS as one of the inputs.

iv. Establish linking with PEGASUS.

Lastly, PEGASUS is run to generate the interpolation protocol. In this investigation, version 4.0 of the software was adopted (Suhs and Tramel, 1991). The outputs from this final process are a modified mesh file made compatible with FANS3D and another containing the interpolation information. Together, they constitute the computational domain for FANS3D. It should be noted that PEGASUS may also be run mid-simulation to update linking for moving domains.

3.3. Solution Algorithm

3.3.1. Overall Algorithm

The essence of the dissertation effort is the coupling of sediment transport modules with the flow solver. FANS3D exists as a collection of subroutines, each carrying out specific functions. Likewise, the sediment transport modules have been implemented in the form of subroutines. This facilitates maintenance and modifications. The overall solution algorithm is as follows:

i. Read in grid information and user inputs.

ii. Initialize flow properties (i.e., velocities, pressure, and turbulence quantities).

iii. Compute eddy viscosity for turbulence modeling.

iv. Compute finite analytic coefficients for solving the Navier-Stokes equations.

v. Compute pseudo-velocities and turbulence terms.

vi. Perform velocity-pressure coupling and velocity correction.

vii. Apply relaxation to the solutions for convergence.

viii. Run bed load transport module and determine bed elevation changes. Update the interpolation scheme using PEGASUS as necessary (depending on the application).

ix. Go back to Step **iii** above until the specified number of time step is reached.

x. Generate output files and terminate the program.

It should be noted that the transport of suspended sediment is determined at Step **v** along with the turbulence terms for efficiency. The reason is that the transport equations are very similar to one another and thus the source terms can be shared. On the other hand,

the bed load transport and the resulting bed elevation changes are determined after the converged velocities have been obtained.

3.3.2. Bed Load Transport Algorithm

The algorithm for determining the bed load transport and the resulting bed elevation changes (Step **viii** of the overall FANS3D algorithm) is given below. It should be noted that most, if not all, terms are in dimensional forms.

i. Calculate the shear stress (τ) using the shear velocity obtained from the wall function approach (Eq. 2.7) and the fluid density:

$$\tau = \rho u_\tau^2 \tag{3.1}$$

ii. Using Eqs. (2.14-2.25), determine the bed load flux per unit width $\boldsymbol{q}_b$.

iii. Calculate the volumetric flux $\boldsymbol{q}_b^*$ using finite volume approach and the mesh geometry.

iv. Calculate the elevation change of the bed (Eq. 2.13).

v. Check whether any region in the bottom surface has local slope exceeding the angle of repose of the sediment. In such case, apply sand slide correction (Eqs. 2.26-2.27) to enforce slope failure and update the bed elevations.

3.4. Computing Environment

The simulations were run on the EOS (retired in 2016), ADA, and TERRA systems of Texas A&M University's High Performance Research Computing Facilities. The version of FANS3D with which this dissertation was undertaken does not support parallel computing, and thus only a single core was employed. The computing time is dependent on the application, and it varies widely with numerous factors including the number of grid points, number of simulation time steps, and internal iteration settings. Thus, in submitting the batch job file, the maximum wall clock time and memory usage limit per node were determined based on experience. Because the CFD solver is written in Fortran, a compiler must be loaded prior to compiling the code and starting the simulation. In the present research, the most recent versions of Intel Fortran compiler at the time of simulation were used. All codes were compiled with the double-precision option.

4. MODEL VALIDATION*

4.1. Suspended Sediment Transport

4.1.1. Net Entrainment

The first validation case was the laboratory investigation by van Rijn (1981), which is characterized by net entrainment of sediment from the bed. In a flume, initially clear, fully-developed flow was introduced over the sediment bed and the sediment concentration was measured after the equilibrium condition was reached. The flume dimensions were 30 m × 0.5 m × 0.7 m (length × width × height). The mean velocity of the inflow was 0.67 m/sec with the water depth being 0.25 m. The median diameter d_{50} of the bed material (sand) was 0.23 mm and its settling velocity was 2.2 cm/sec. Syphon method was employed to sample the water-sediment mixture at five different depths at each of the four stations downstream of the inlet. The schematic of the experimental setup is provided in Fig. 4.1.

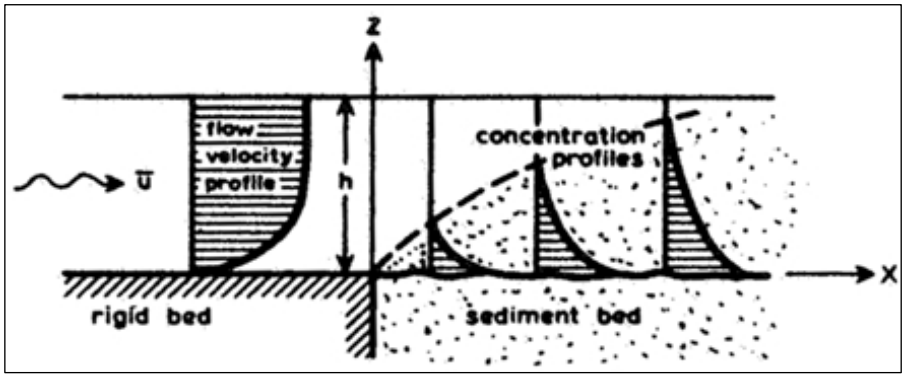

Fig. 4.1. Schematic of the net entrainment experiment by van Rijn (1981).

The mesh for this case consisted of a single prismatic block with the dimensions 201 × 3 × 21 (length × width × height) grid points. The effects of the sidewalls were assumed to be negligible and the flow was treated as two-dimensional. The wall function approach was employed for the bottom boundary, with the equivalent roughness height k_s set to 0.01 m. At the inlet, the velocity profile of the fully-developed flow was specified as the boundary condition, with zero sediment concentration. At the sidewalls zero-gradient boundary condition was used for all quantities.

The comparison between the simulation and the measurements is given in Fig. 4.2. The Figure shows the results at two different locations, $x/h = 4$ and $x/h = 40$ (x and h denote the distance from the inlet and the water depth, respectively). The computed and measured sediment concentrations were normalized by a reference value of 3,000 mg/L. The vertical axis was normalized by h. One can observe that the entrainment from the bed led to the increased concentration of suspended sediment between the two stations. For the normalized depth above around 0.5, insignificant concentration was predicted. Overall, the computed concentrations agree very well with the measurements.

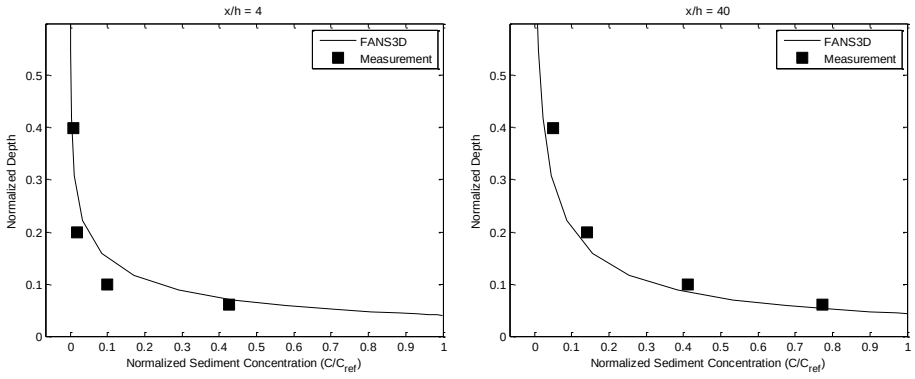

Fig. 4.2. Sediment concentration profiles for the net entrainment case.

4.1.2. Net Deposition

Another experimental study, conducted by Wang and Ribberink (1986) and involving zero entrainment from the bed, was used as the second validation case for the suspended sediment module.

The experiment was carried out in a straight flume with the dimensions 30 m × 0.5 m × 0.5 m (length × width × height). The mean longitudinal velocity was 0.56 m/sec. A constant flux of sand was supplied at the inlet of the flume, thus mimicking a steady, sediment-laden open channel flow. The characteristic diameter of the sediment d_{50} was 0.095 mm and settling velocity was 0.65 cm/sec. Samples were taken using syphon at different distances downstream of the flume. To ensure that there was no re-entrainment of sediment from the bed, the channel bed was perforated and a compartment was placed below to capture and contain the sand particles, as shown in Fig. 4.3.

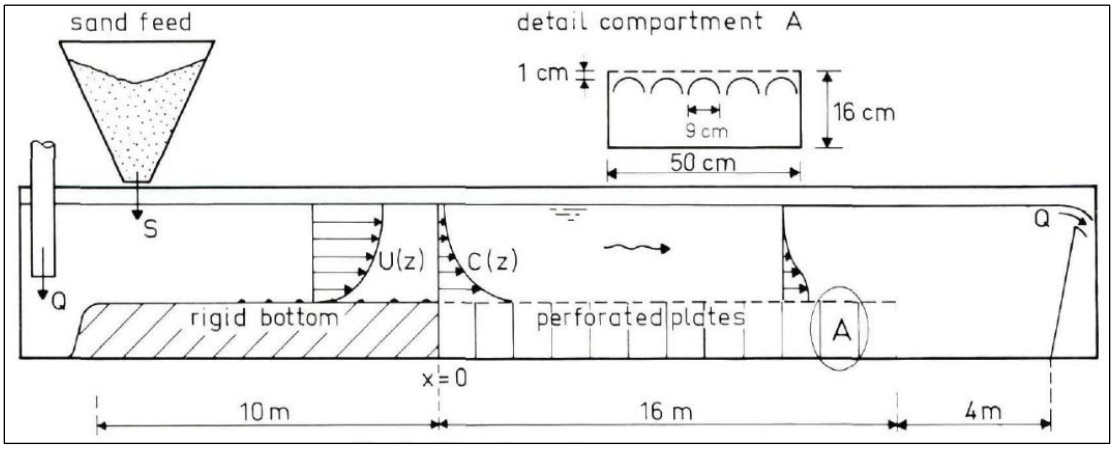

Fig. 4.3. Experimental setup for net deposition study by Wang and Ribberink (1986).

With the physical specifications provided above, the experiment was simulated with a domain of the dimensions 201 × 3 × 51 (length × width × height) grid points. With the same assumptions as the net deposition case, the flow was treated as two-dimensional. The measured distribution of suspended sediment at x = 0.1 m downstream from the inlet was taken as the inlet boundary condition for simulation. At the bed, zero-gradient condition was used for the sediment concentration, since there was no upward flux.

The results are presented in Fig. 4.4, for x/h =5 and x/h = 72. It can be seen that the simulation predicted the actual concentrations very well in general. The concentration near the bed was over-predicted by the model. It is possible that an improved bed boundary condition is required to model the process with higher accuracy.

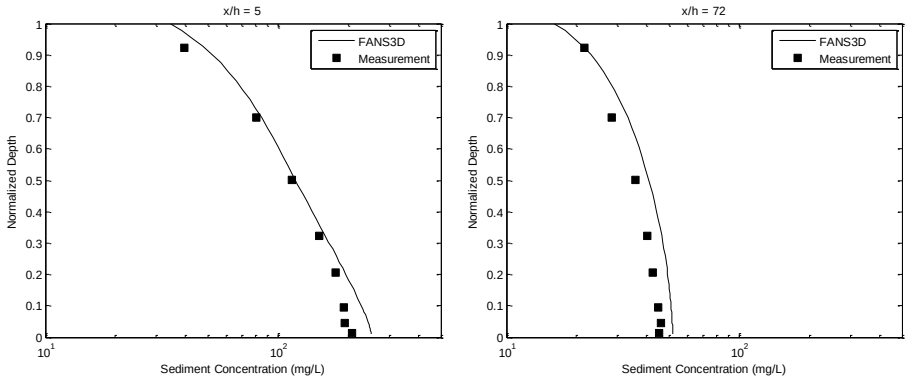

Fig. 4.4. Sediment concentration profiles for the net deposition case.

4.2. Bed Load Transport

The experiment conducted by Khosronejad et al. (2012) involving local scour around a cylindrical pier was used to validate the bed load transport module. In this particular case, a cylindrical pier of 16.51 cm in diameter was placed in a rectangular flume measuring 10 m × 1.21 m × 0.45 m (length × width × height). The bed material was uniform sand with d_{50} = 0.85 mm. The depth and approach velocity of the inflow were 18.6 cm and 0.41 m/sec, respectively. The flow and scour under this setup was simulated with FANS3D. The predicted time development of the scour depth ($\mathbf{z}$) is plotted in Fig. 4.5 against the experimental measurements, as well as the simulation result by Khosronejad et al. (2012) obtained with their numerical model FSI-CURVIB.

The comparison shows that FANS3D performed with a reasonably good agreement with the measured data. The predicted equilibrium scour depth ($\mathbf{z}_{eq}$) is 7.9 cm, which corresponds to an error of 5.4% from the measured value of 7.5 cm. On the other hand, the FSI-CURVIB method by Khosronejad et al. (2012) produced a 15.9% error with the predicted $\mathbf{z}_{eq}$ of 6.5 cm. It should be noted, however, that the time development of the scour depth predicted by FANS3D deviates from the measurements starting at time $t \approx 10$ min. as the rate of scour is reduced. Having observed a similar trend in their simulation, Khosronejad et al. (2012) explained that the discrepancy occurs because the two-equation isotropic eddy viscosity turbulence models (e.g., k-ε adopted in the current study) overpredict the magnitude of eddy viscosity at places of sharp pressure gradients, thereby underpredicting the effect of turbulent horseshoe vorticity system (THSV).

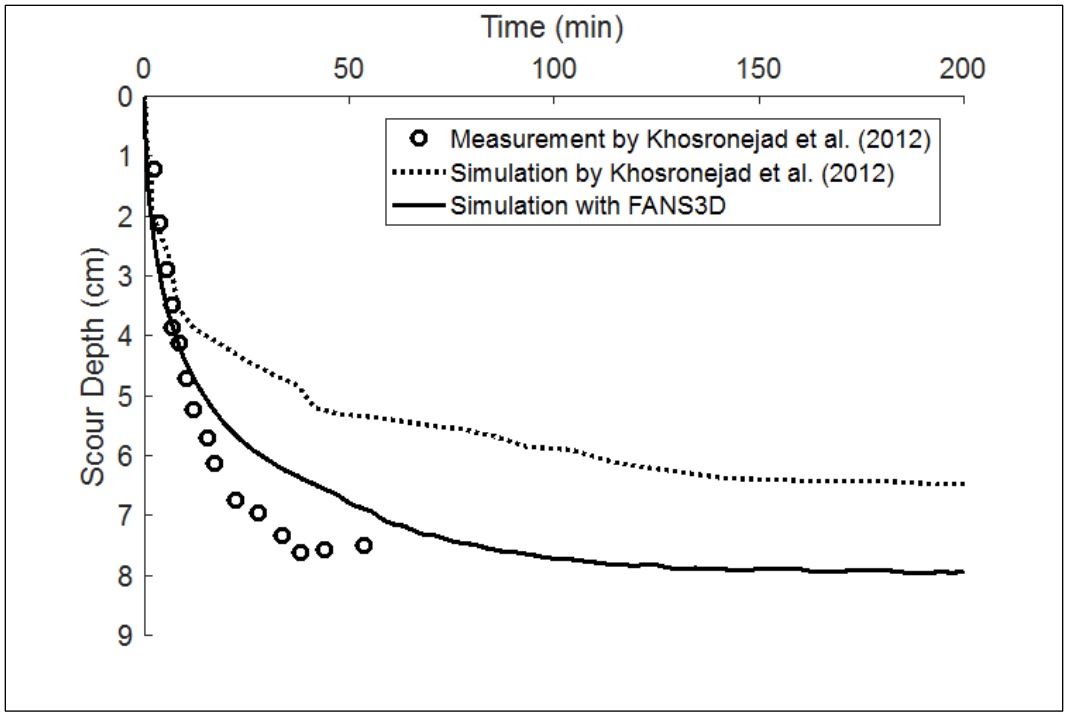

Fig. 4.5. Time series of the maximum scour depth around cylindrical pier under the experimental setup by Khosronejad et al. (2012).

Nevertheless, FANS3D predicted the equilibrium scour depth more accurately, which can be attributed to the morphologic model employed. In Khosronejad et al. (2012), the bed load flux was computed with the near-bed velocity vector and sediment concentration, which are obtained with interpolation and an empirical relation, respectively.

On the other hand, the approach by Roulund et al. (2005) adopted herein determines the particle motion from the force balance, taking into account the gravitational, drag, lift, and frictional forces acting on the particle.

Fig. 4.6 shows both the predicted and measured bed morphologies around the pier at equilibrium. The scour depth predicted by the simulation is found near the upstream side of the pier inside the area defined by $30° < \Phi < 90°$, where Φ is the angle measured from the upstream nose of the pier. The fact that this area does not encompass the upstream nose, as it did in the experiment, evidences the discussion presented above regarding the role of THSV. Overall, the prediction and the measurements show good agreement.

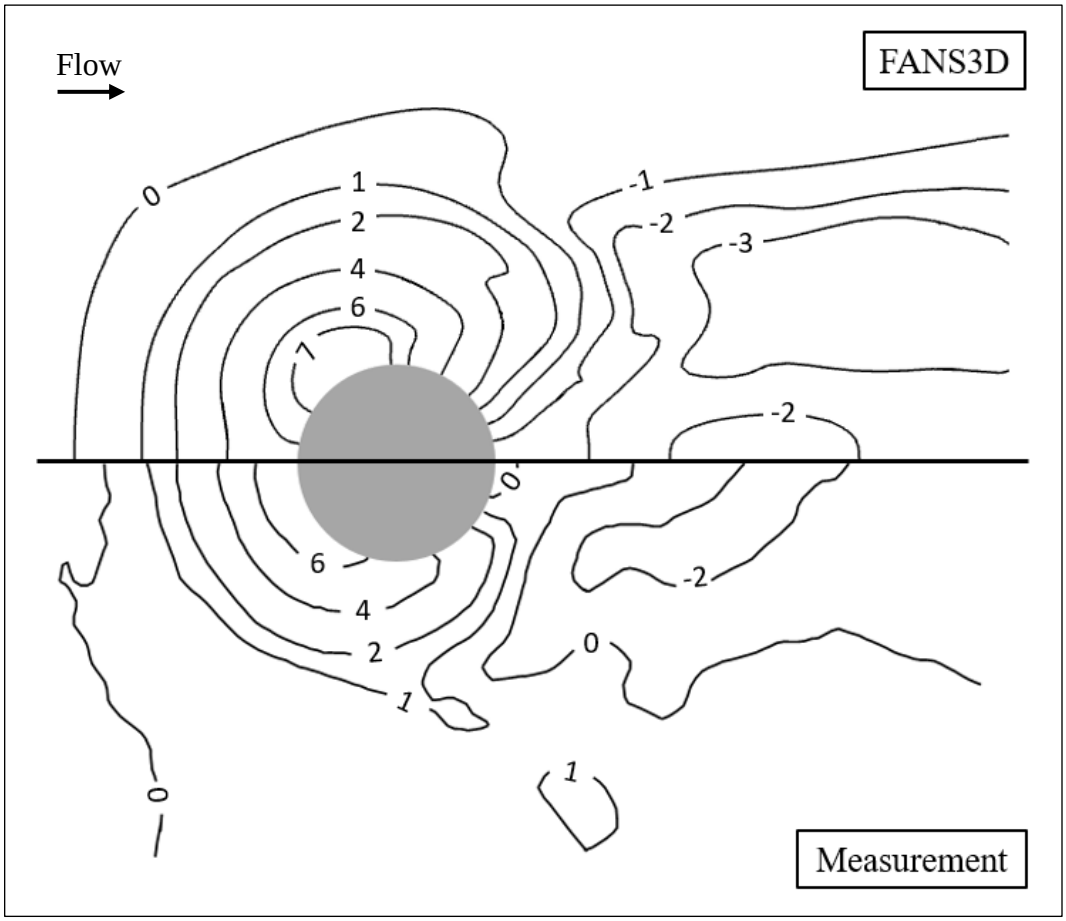

Fig. 4.6. Bed morphology around the pier at equilibrium (depth in cm; negative indicates above initial bed level). Compared are the prediction by FANS3D (top) and the measurements reported by Khosronejad et al. (2012) (bottom).

5. APPLICATIONS

5.1. Suspended Sediment Transport in Channel Bend

5.1.1. Introduction

The flow and transport of suspended sediment particles, in the form of plume, were simulated using FANS3D. The physical domain considered is an open channel with a 90° bend and wingwall abutments, which induces complex, three-dimensional flow characteristics. The effect of the sediment particle size was also analyzed using two different median diameters: 0.10 mm and 0.20 mm.

The motivation was ultimately to contribute to environmental engineering research by providing a means to simulate and visualize the transport of waterborne particles or plumes. One such implication is the transport of contaminated soils, especially those originating from concentrated animal feeding operations. It is reported that during floods, high amounts of manure and hormone-absorbed soil enter natural streams with the runoff, causing disruptive effect in the environment (Sun et al., 2010; Qi and Zhang, 2016; Adeel et al., 2017). Being able to characterize how such contaminants behave in complex flow environment and where the maximum concentrations occur in a stretch of rivers or streams will contribute to the mitigation efforts.

Another closely related implication is sedimentation in reservoirs and open channel systems. Sedimentation in reservoirs causes operational issues and the turbid currents often need to be vented through outlets (Lee et al., 2014; Chamoun et al., 2016). High turbidity in natural systems also endangers aquatic species, because thick plumes

prevent exposure to the light, and because of heavy metal contamination (Albert et al., 2015; Kulshreshtha and Shanmugam, 2015; Restrepo et al., 2016). If the transport of suspended sediment can be accurately simulated, the results can aid in predicting the light attenuation, which is the intensity reduction of light through depths of water column (Davies-Colley and Smith, 2001).

Not surprisingly, there have been past studies aimed at predicting the suspended sediment concentration in flow. Hjelmfelt and Lenau (1970) presented an analytic solution for the concentration profile in a uniform flow, with the sediment entrained from the bed. The assumptions were that the diffusion coefficient profile over the water depth is parabolic and that the depth-average velocity is constant.

Early numerical investigations include those by van Rijn (1981), which implemented a mathematical model validated with the aforementioned work of Hjelmfelt and Lenau (1970), and by Wang and Ribberink (1986), which validated a depth-integrated transport model with experiments. In their laboratory setting, a specially fabricated flume with perforated bed was used, which allowed no re-suspension from the bed once the sediment particles pass through the holes.

More recently, CFD simulation was utilized for three-dimensional study in various environments. Haun et al. (2013) used a three-dimensional model to predict the sediment concentration in various location in a reservoir. Basser et al. (2015) conducted an experimental and numerical study of scour around a rectangular abutment including suspended sediment, but the focus was given to scour depth at various locations in the channel and the plume transport was not discussed in detail.

The present investigation is an improvement upon a previous work by the author (Kim and Chen, 2014) by incorporating two different sediment particle sizes and their physical characteristics. The flow domain, originally presented by Chen (2008) was modified to eliminate those components with little relevance to plume transport.

5.1.2. Flow Environment

In the setup for the present investigation, a sediment plume with the volumetric concentration of 1,000 parts per million (ppm) is introduced at the inlet of the channel. That is, the concentration profile does not vary along the flow depth. With the intention to visualize the movement of particles in the water column, it was assumed that there is no deposition or erosion taking place at the bed. Rather, the particles that fall onto the bed will simply "pass through" the bed surface. This setup reduces the number of sediment sources to only one: the inlet. This approach is identical to the approach used by Wang and Ribberink (1986) in their flume study involving a perforated flume.

The overall flow environment resembles that used in the study by Chen (2008), which analyzed the shear stress and the subsequent cohesive sediment scour around abutments with overtopping flow. The original channel consisted of a 90° bend, with wingwall abutments on either side of the cross section at the middle of the bend. The abutments supported a rectangular bridge, for which the overtopping was simulated. Also, the channel featured a depression along its centerline.

For the current study, however, several modifications were made to the original domain. First, since the goal was to simulate the plume transport in the channel bend and not the flow overtopping a bridge, the blocks associated with the overtopping were

removed. It was also deemed that the presence of the wingwall abutments provided a sufficiently complex flow environment worthy of investigation. Secondly, the bed was made flat by removing the depression that extended in the longitudinal direction. This change has a physical ground; the depression's slope in the transverse direction (45°) exceeded the angle of repose of non-cohesive sediment, which results in slope failure. The original and modified meshes are depicted in Fig. 5.1.

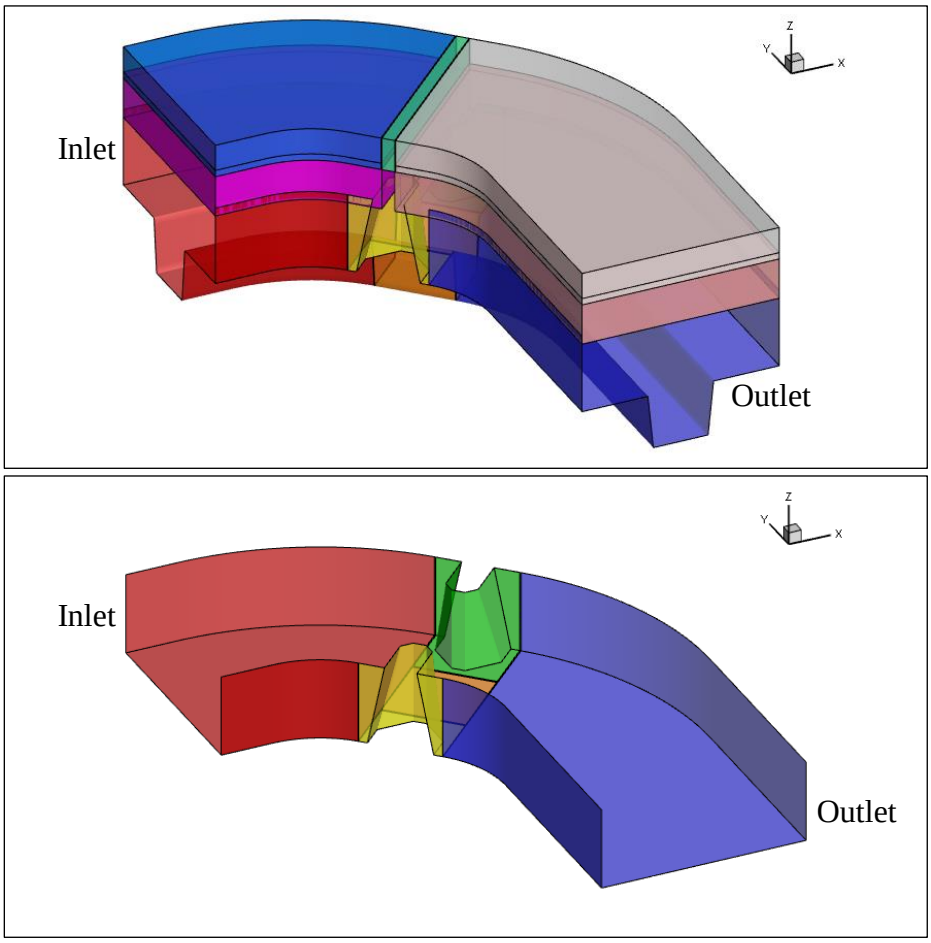

Fig. 5.1. Channel configurations for Chen (2008) (top) and the current simulation (bottom). The vertical scale was magnified by a factor of 10.

The same flow properties as in Chen (2008) were used for the current simulation. The approach velocity was 0.43 m/sec, and the flow depth was 0.29 m. The resulting Reynolds Number is 112,000.

The two median sediment diameters considered were d_{50} = 0.10 mm and d_{50} = 0.20 mm, with settling velocities of 0.7 cm/sec and 2.4 cm/sec, respectively (Zanke, 1977). The density was assumed to be equal at 2650 kg/m^3, and the porosity was assumed to be 0.40.

5.1.3. Mesh

As with the physical configuration, the grid structure of the original mesh was also modified. Fig. 5.2 depicts the change made to Block 1, which spans from the channel inlet to immediately upstream of the abutments. As shown in the Figure, fewer grid points were adopted in the transverse direction. The abrupt changes in the grid spacing were avoided with the elimination of the depression in the channel bed. Also, the near-wall spacing increased from 0.0016 mm to 9.7 mm. This change was made because unlike the original simulation, which used the two-layer model to resolve turbulence, this investigation used the wall function approach. Similarly, the spacing in the vertical direction was similarly altered (not shown). However, the blocks associated with the abutments maintained their original structure and the two-layer model was used.

The number of grid points for both the original (two-layer) and the new (wall function) meshes are presented in Table 5.1. As can be seen, the adoption of the wall function approach led to an added benefit of reduction of computing resources. It should be noted that this Table excludes the blocks associated with the overtopping flow in the

original mesh. The longitudinal, transverse, and vertical coordinate directions are denoted with ξ, η, and ζ, respectively.

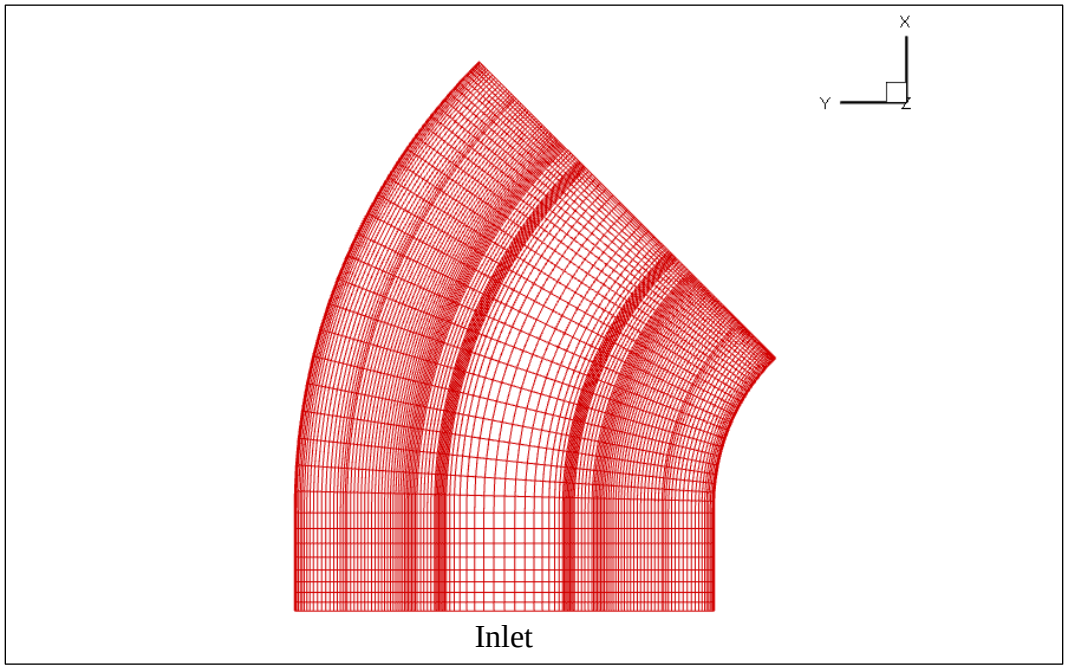

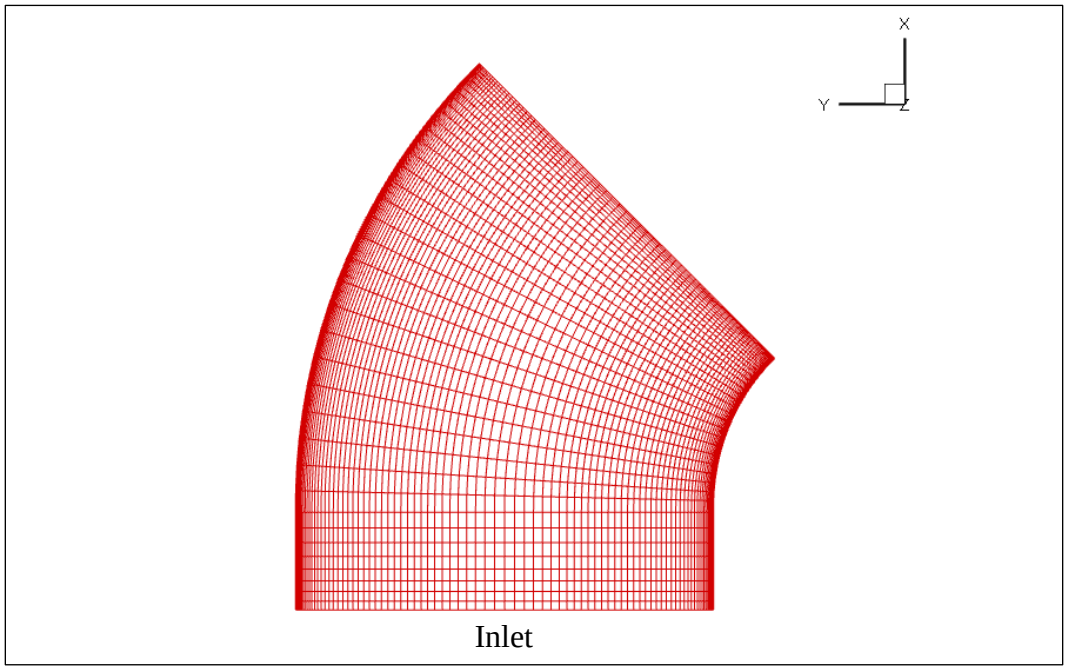

Fig. 5.2. Mesh structures for two-layer model (top) and wall function (bottom).

Table 5.1. Number of grid points used for the plume transport study.

Block	Description	Original (two-layer model)			New (wall function)		
		ξ	η	ζ	ξ	η	ζ
1	Inlet	40	147	25	40	87	25
2	Middle	109	43	25	89	43	25
3	Abutment at inner bank	211	44	25	211	44	25
4	Abutment at outer bank	211	44	25	211	44	25
5	Outlet	80	147	25	80	87	25
	Total	1,022,375			820,875		

5.1.4. Simulation Setup

In flow simulations with FANS3D, all quantities are in the non-dimensionalized forms. For the current study, the characteristic length and velocity scales were set equal to the initial flow depth and the approach velocity, respectively. The non-dimensional time step size used, 0.15, translates to the physical step size of 0.102 seconds.

The boundary conditions were chosen to recreate the physical processes. At the channel inlet, the longitudinal velocity profile was prescribed using logarithmic profile of Wu et al. (2000). The transverse and vertical velocities, as well as the turbulence quantities, were set to zero. A uniform profile of 1,000 ppm of sediment concentration was prescribed and the turbulence quantities were set to zero. At the outlet, all quantities followed the zero-gradient condition, where the values at the node upstream were adopted as the boundary condition. At the free surface, the rigid-lid condition was assumed. The longitudinal and transverse velocities followed zero-gradient conditions, whereas the vertical velocity was set to zero. The turbulence quantities were solved using Eqs. (2.8-2.9) and the suspended sediment concentration was set using Eq. (2.11). At the sidewalls

and the bed, the flow and turbulence quantities were resolved using the wall function as discussed in Section 2.1.2. However, the roughness height along the sidewalls were set to zero, whereas the bed roughness height was assumed to be three times the sediment diameter following van Rijn (1984). The sediment plume was assumed to simply "pass through" the boundaries using the zero-gradient condition, instead of using Eq. (2.12).

5.1.5. Results and Discussion

Before presenting the results for suspended sediment, it is first necessary to discuss the hydrodynamics in the channel bend. Fig. 5.3 shows the local total velocity magnitude, computed at each grid point, of the pseudo-equilibrium flow in three different channel depths. It should be noted that values represented by the color contours are relative to the characteristic velocity scale. For instance, the value of 3 indicates that the magnitude is three times as high as the approach velocity.

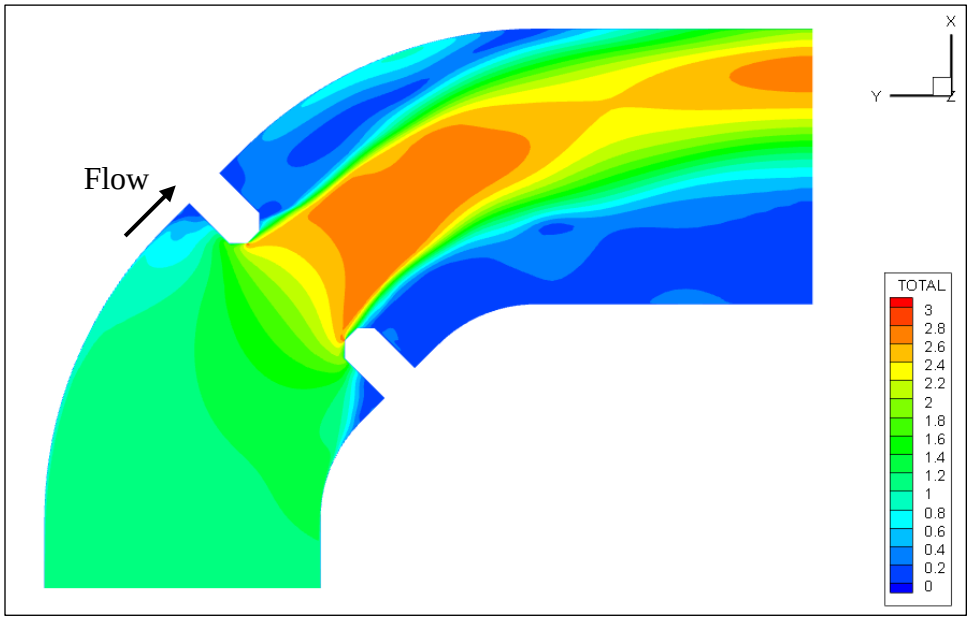

Fig. 5.3. Toal velocity magnitude in channel bend: top surface.

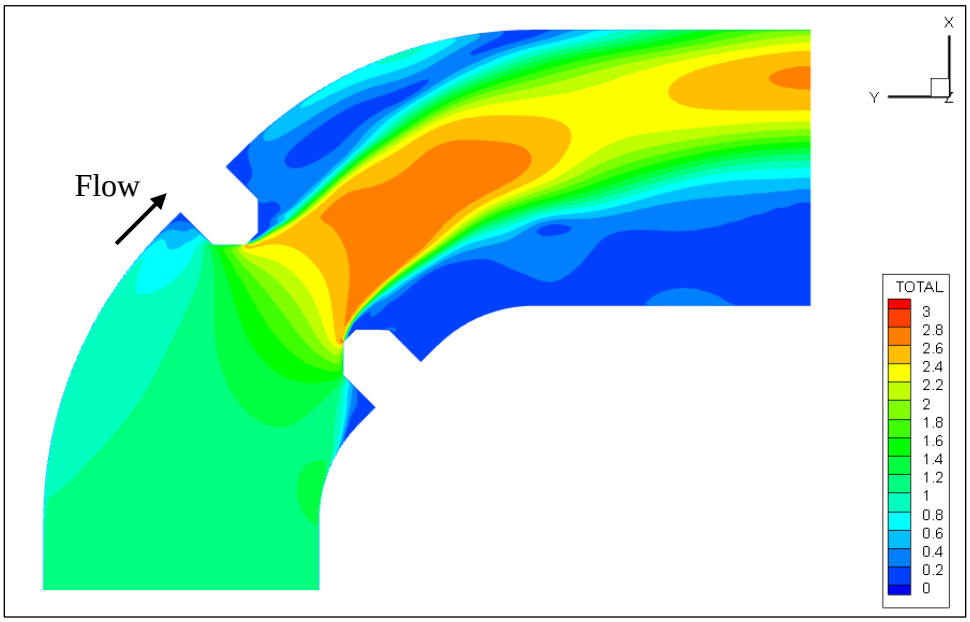

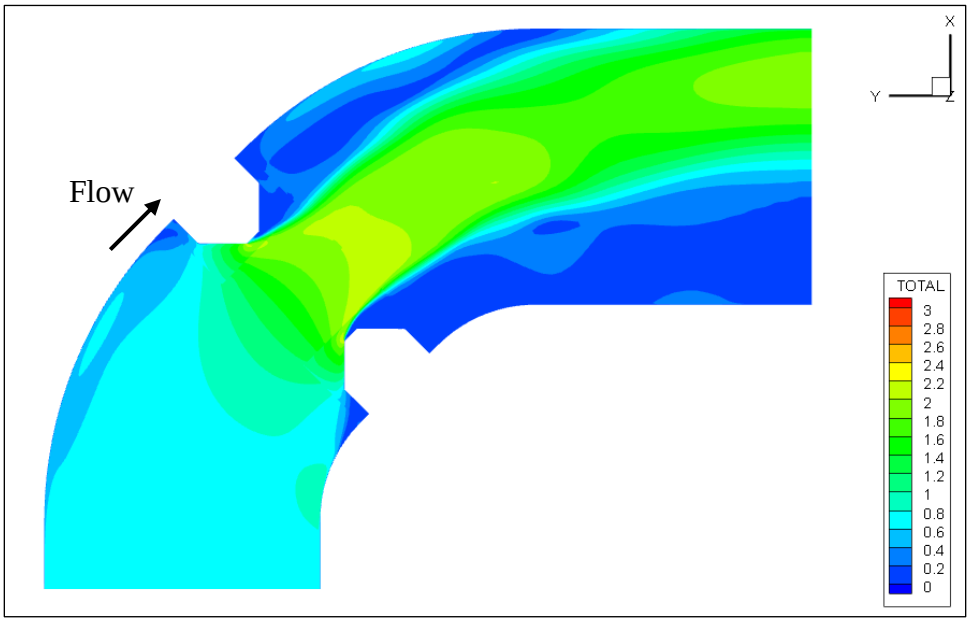

Fig. 5.3. (continued) Toal velocity magnitude in channel bend: mid-depth (top of this page), at 9.7 mm from the channel bed (bottom).

It can be seen that the contraction caused by the two abutments led to flow acceleration. At the top surface, for instance, the flow magnitudes immediately upstream and downstream of the passage along the centerline differ by a factor of 1.5. In each of the corners formed by the abutments and the channel sidewalls, sharp reduction in the velocity magnitude is observed due to pressure gradient and flow recirculation. Vortices formed around and downstream of the abutments, shown in Fig. 5.4, agreeing well Koken and Constantinescu (2014). The positive and negative values indicate the counter-clockwise and clockwise directions, respectively.

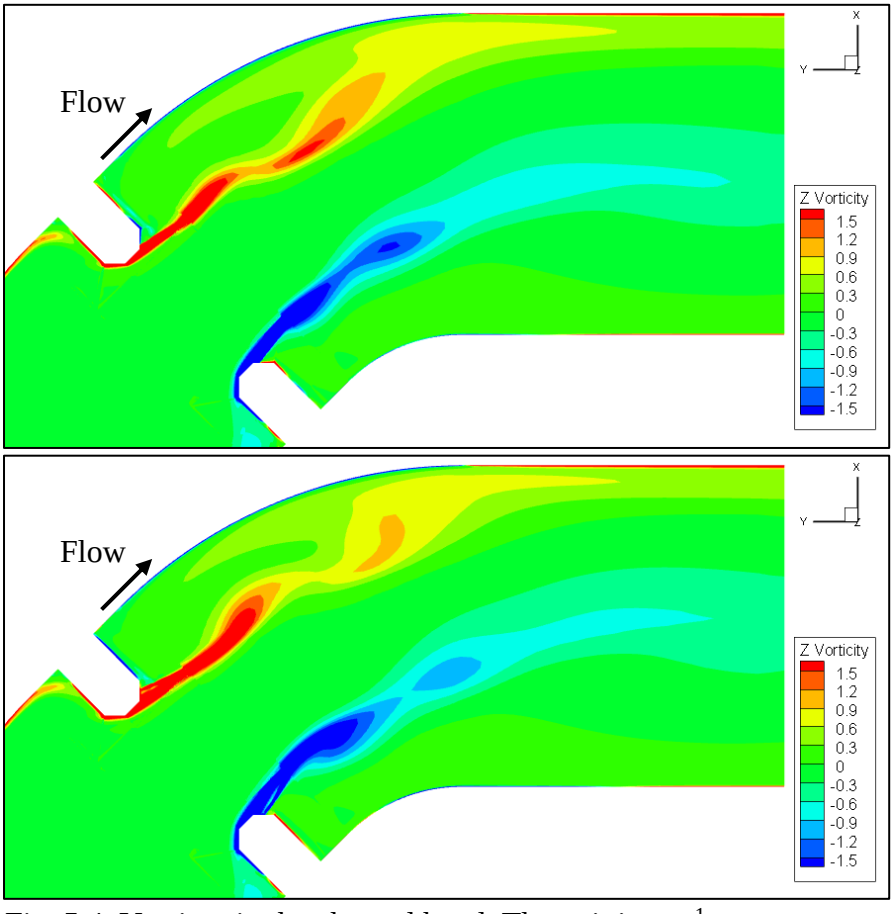

Fig. 5.4. Vortices in the channel bend. The unit is sec^{-1}.

The flow behind the abutments are studied in greater detail with the local velocity vectors and the total velocity magnitude (Fig. 5.5). Here, the vectors are shown only on the top surface of Block 5. As observed in the Figure, there are vortices rotating in opposite directions behind each abutment. These, combined with the curvature of the channel, generate a unique and complex three-dimensional flow pattern.

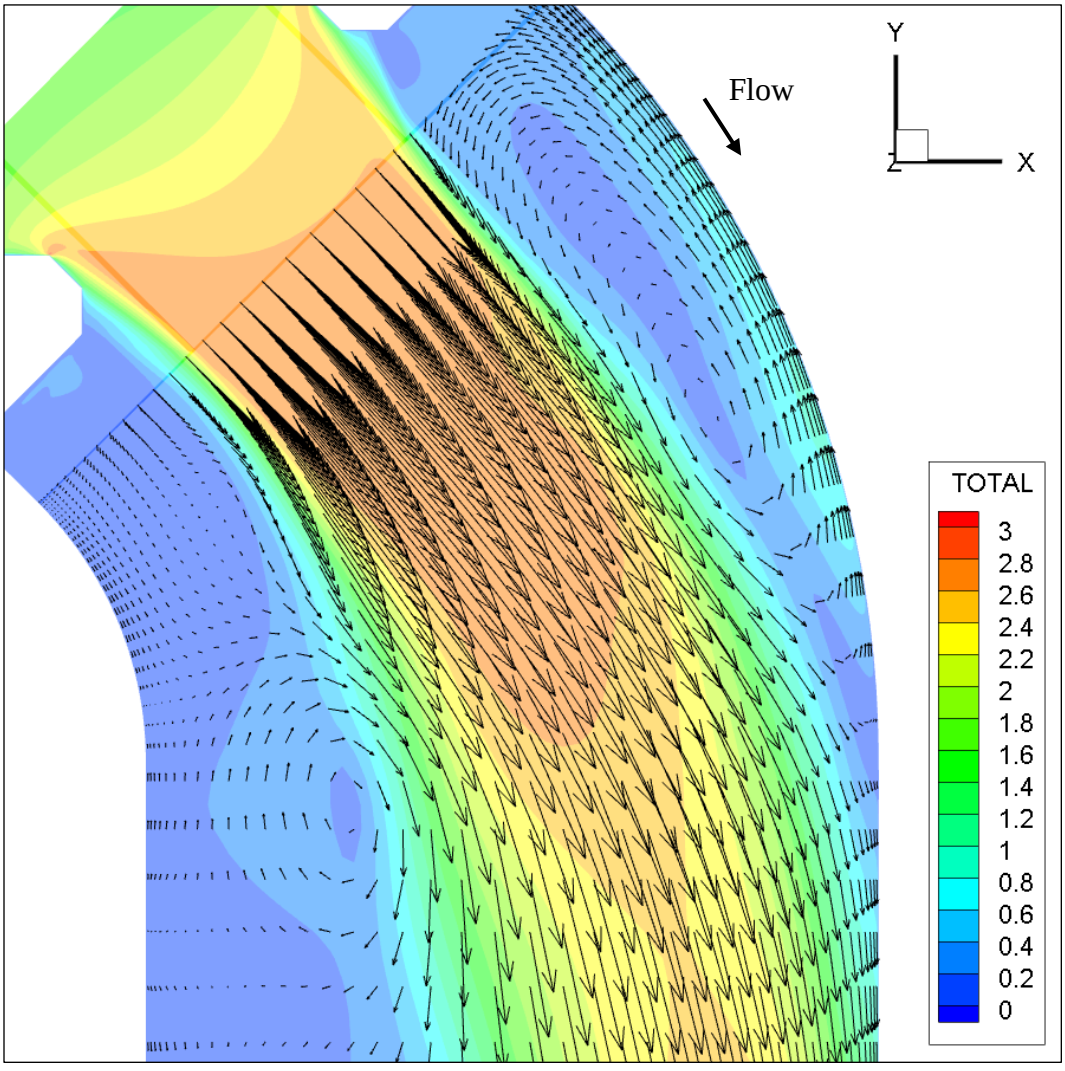

Fig. 5.5. Flow characteristics downstream of the wingwall abutments.

When the suspended sediment transport was initiated in the flow field thus described, significant difference was produced between the two diameters. The time series of the concentration distribution in the channel are compared in Figs. 5.6 (top surface) and 5.7 (near-bed plane). Fig. 5.6 is discussed first. It can be clearly seen that the plume concentration at the top surface drops sharply immediately after release for d_{50} = 0.20 mm. On the other hand, the concentration associated with d_{50} = 0.10 mm is at least an order of magnitude higher at the same locations because of its lower settling velocity. Immediately upstream of the contraction, however, locally higher concentration is observed. This is due to the intense mixing driven by the vortices formed (Kwan and Melville, 1994; Barbhuiya and Dey, 2004). Downstream of the contraction, the sediment concentration is significantly higher along the centerline due to the flow acceleration occurring between the abutments. In the frames for t = 40 min. and t = 60 min., plume travelling upstream is observed due to the swirl.

In Fig. 5.7, which shows the near-bed concentration, the effect of settling velocity is seen more clearly. The contour distribution is very similar between the two sediment diameters. However, after t = 40 min., one can see that the particles with d_{50} = 0.10 mm travel significantly farther downstream before settling to the bed. Both Figs. 5.6 and 5.7 indicate the concentration was higher in the area near the inner bank.

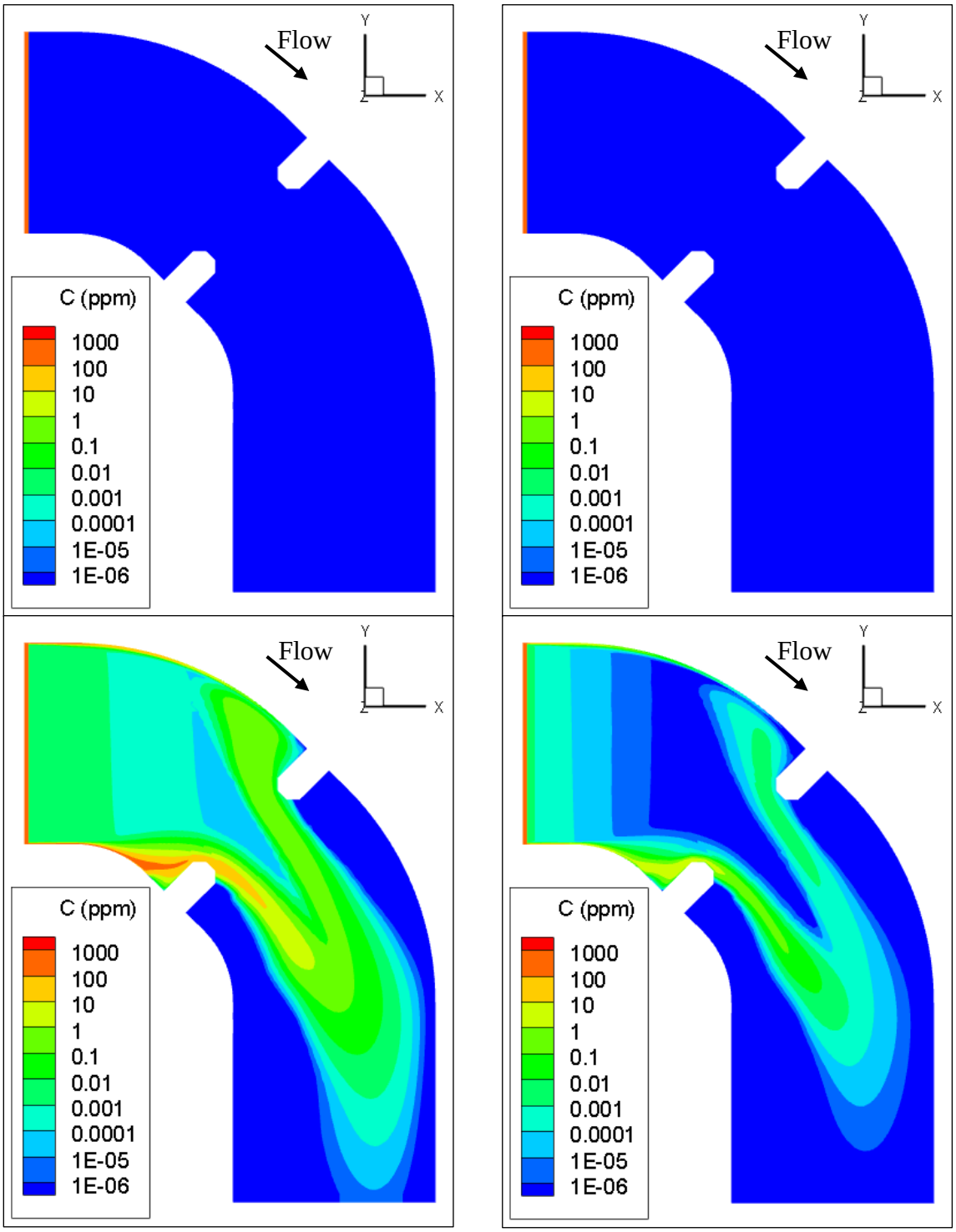

Fig. 5.6. Suspended sediment distribution at top surface for d_{50} = 0.10 mm (left) and d_{50} = 0.20 mm (right), at t = 0 (top) and t = 20 min. (bottom).

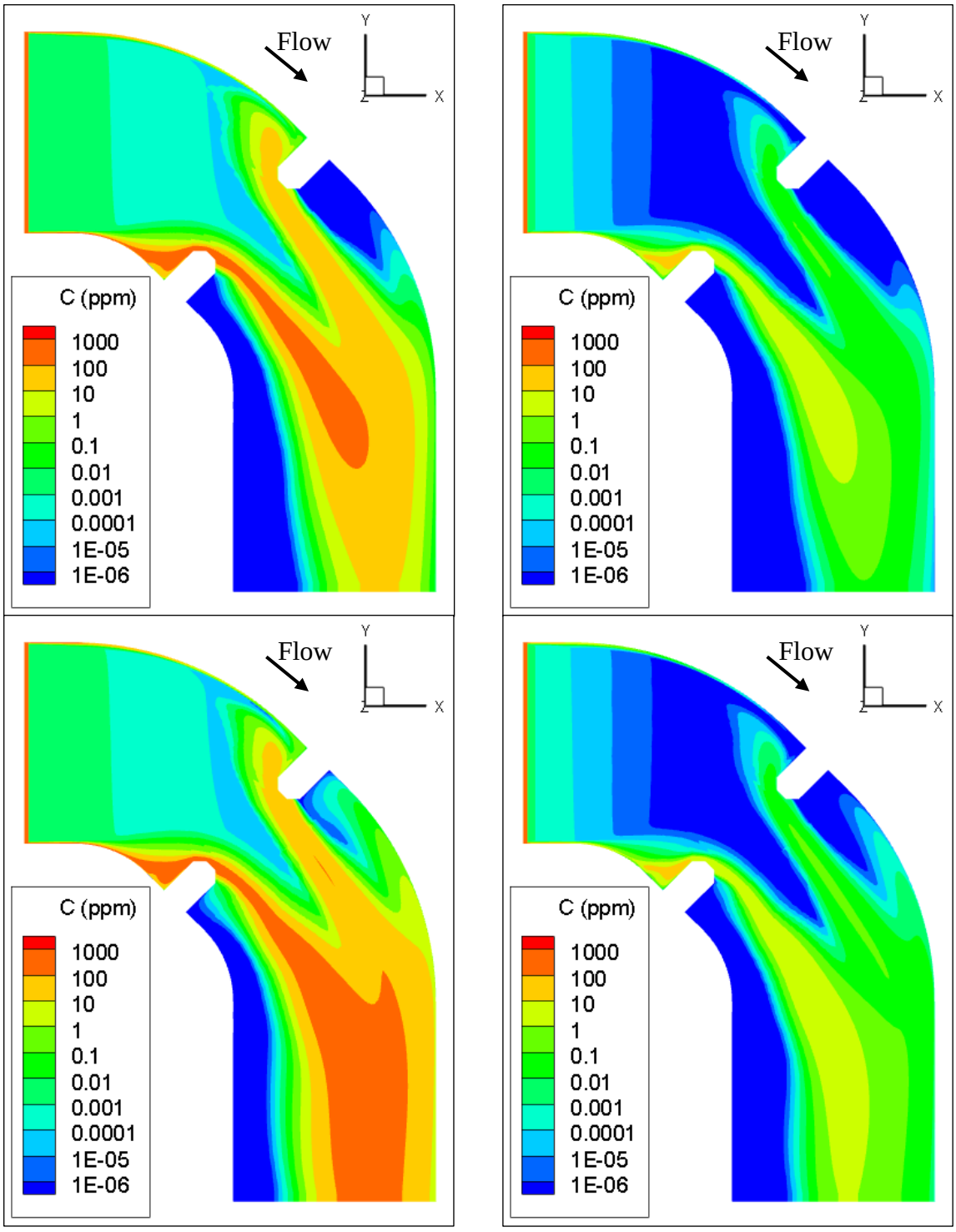

Fig. 5.6. (continued) Suspended sediment distribution at top surface for d_{50} = 0.10 mm (left) and d_{50} = 0.20 mm (right), at t = 40 min. (top) and t = 60 min. (bottom).

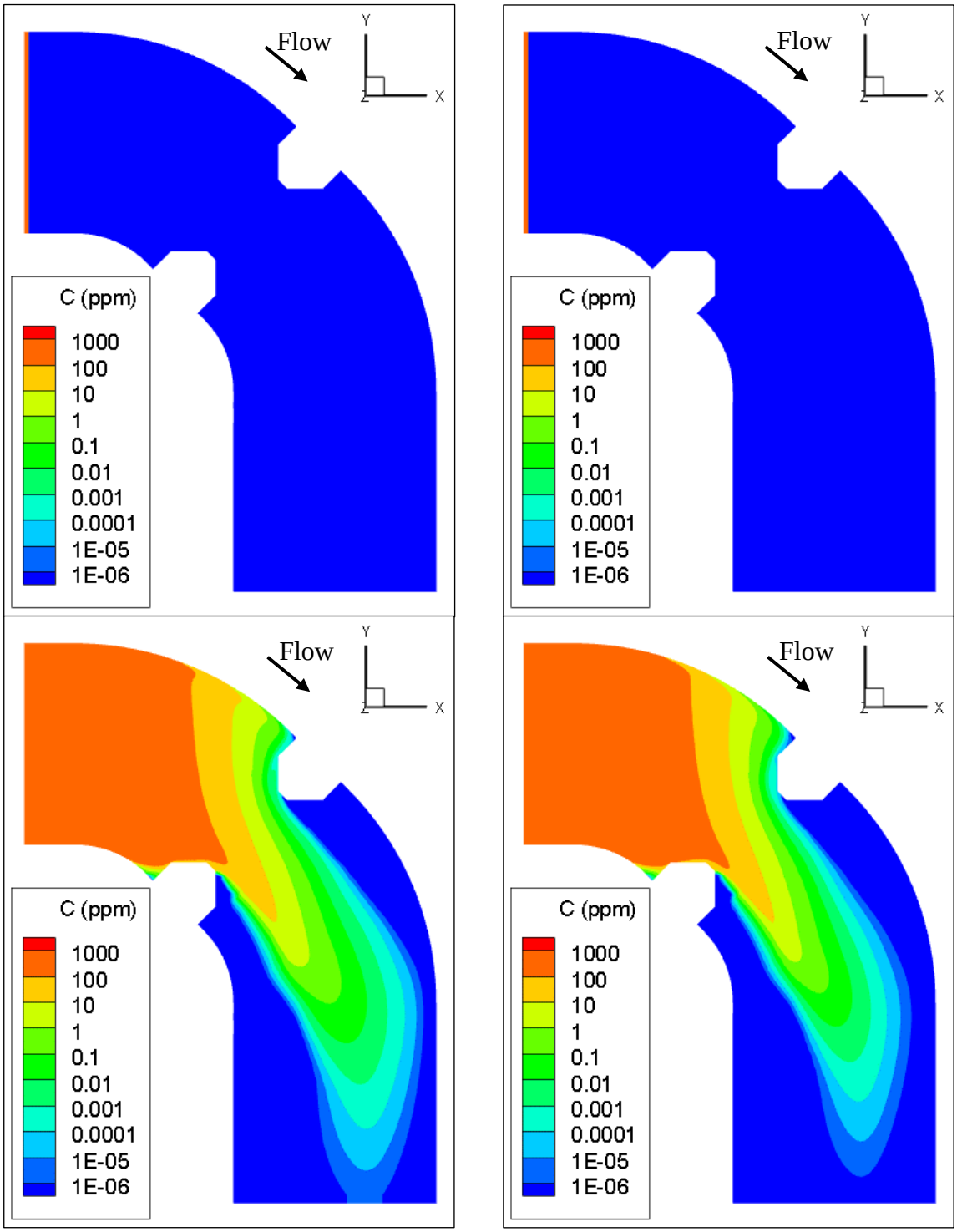

Fig. 5.7. Suspended sediment distribution near bed for d_{50} = 0.10 mm (left) and d_{50} = 0.20 mm (right), at t = 0 (top) and t = 20 min. (bottom).

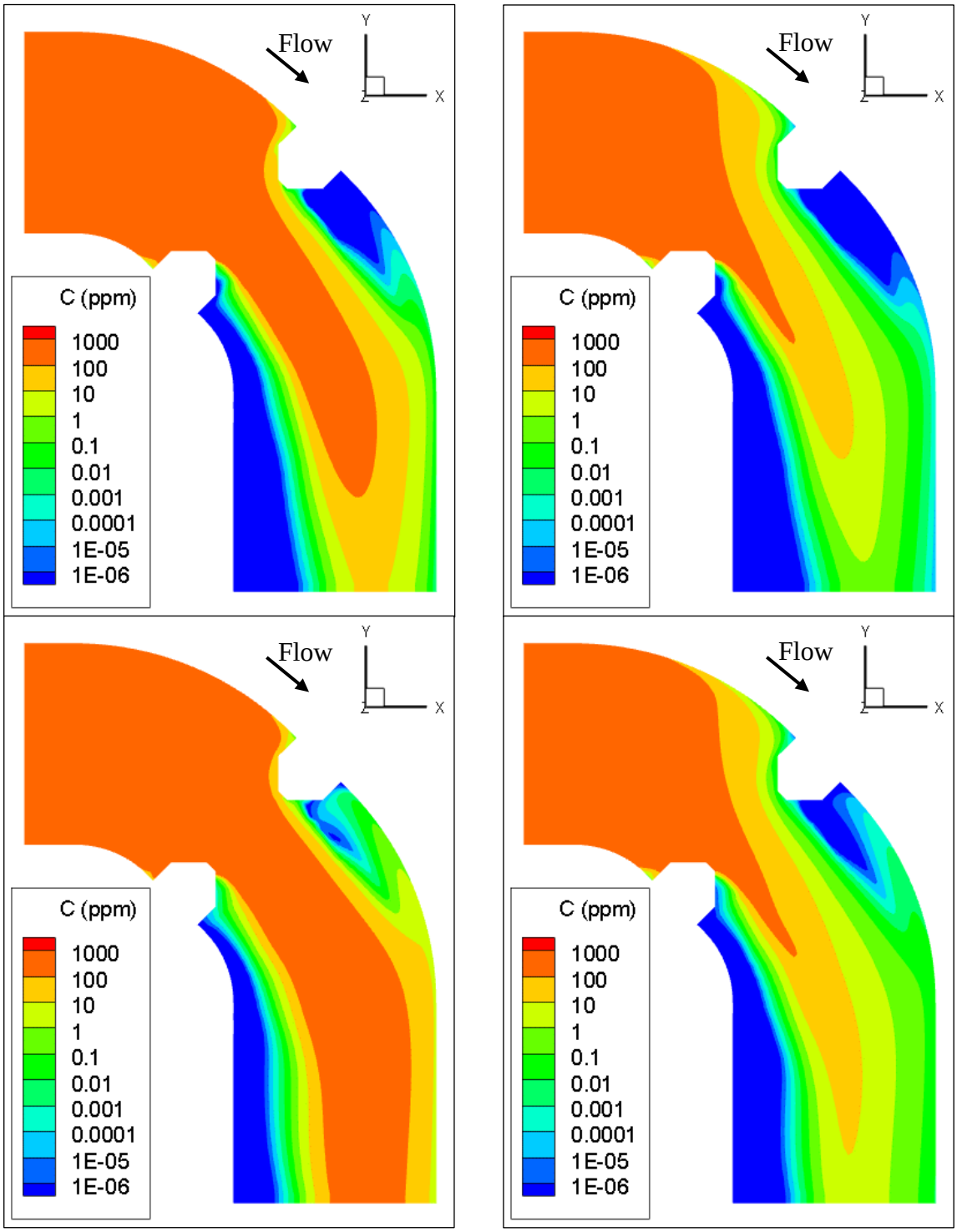

Fig. 5.7. (continued) Suspended sediment distribution near bed for d_{50} = 0.10 mm (left) and d_{50} = 0.20 mm (right), at t = 40 min. (top) and t = 60 min. (bottom).

The time series of the sediment concentration distributions in the longitudinal mid-plane are presented in Figs. 5.8 and 5.9 for both median diameters. These Figures show the concentration profiles along the depth of the channel, as well as the mixing induced by the flow acceleration. In the first frame of Fig. 5.8, corresponding to t = 20 min. for d_{50} = 0.10 mm, it can be seen from the contours past the abutments that the local maximum concentration occurs not near the bed, as Wang and Falconer (1995) proved, but instead mid-depth. This is due to the flow acceleration between the abutments and the subsequent vortices, which cause mixing. By the same mechanism, the top surface's concentration is lower between the abutments than in the downstream regions.

For the case with d_{50} = 0.20 mm, however, the settling velocity dominated the transport mechanism, and the maximum concentration occurs near the bed. The mixing due to the flow acceleration and vortices had some influence, though, as evidenced by the rise of contours near the outlet of the channel. Comparing Figs 5.8 and 5.9, it is clearly seen that the smaller particles, with their lower settling velocity, travel farther before settling.

The effect of sediment diameter on the plume transport is further investigated by observing the concentration distribution in the cross sections upstream and downstream of the abutments, as well as in between them. Fig. 5.10 captures the profile views of the contours for both sediment diameters at t = 60 min. The Figure reinforces the findings already noted that smaller particles result in higher concentration in the water column, since the particles settle slower.

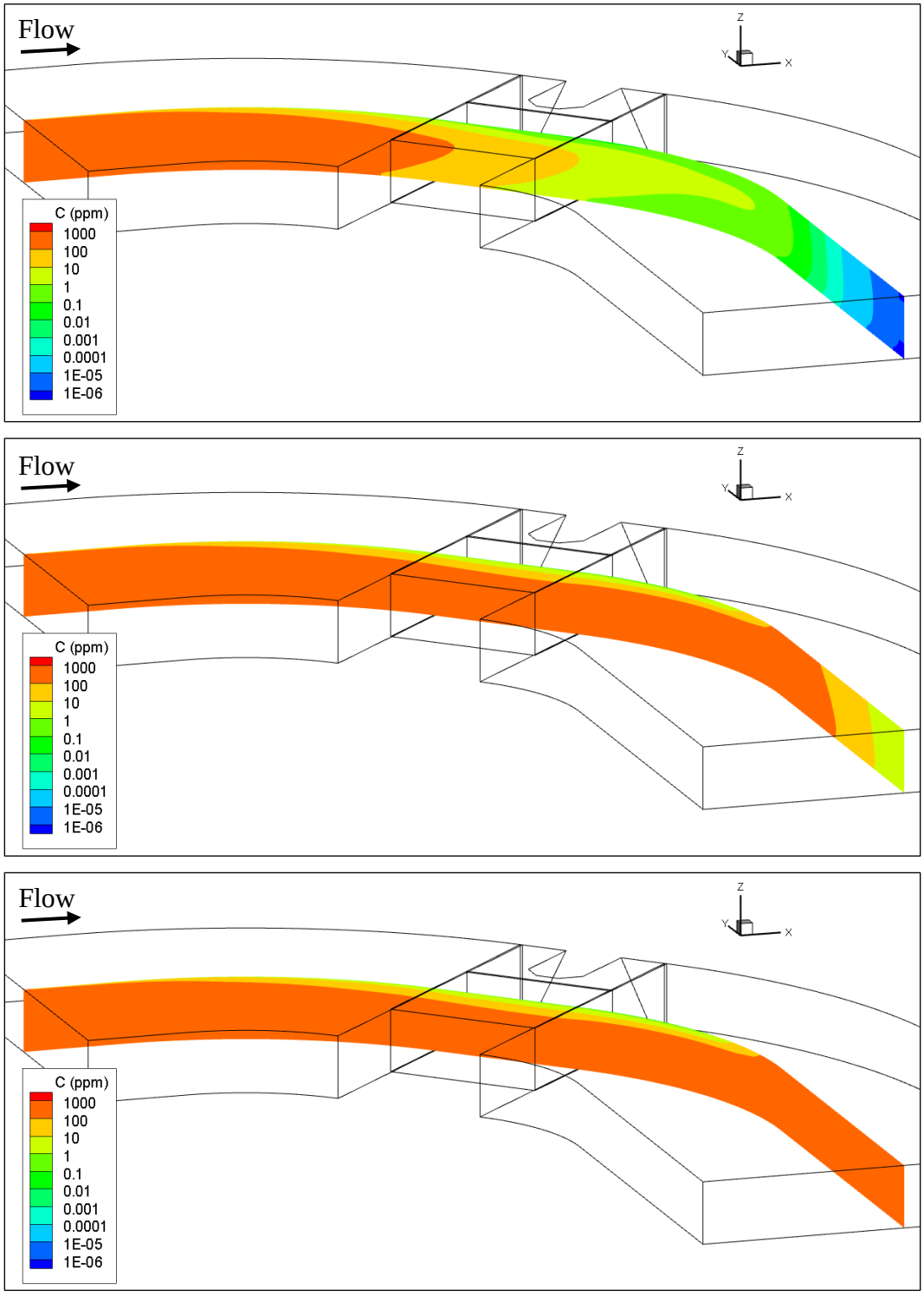

Fig. 5.8. Sediment concentration in the longitudinal mid-plane for d_{50} = 0.10 mm at t = 20 min. (top), t = 40 min. (middle), and t = 60 min. (bottom).

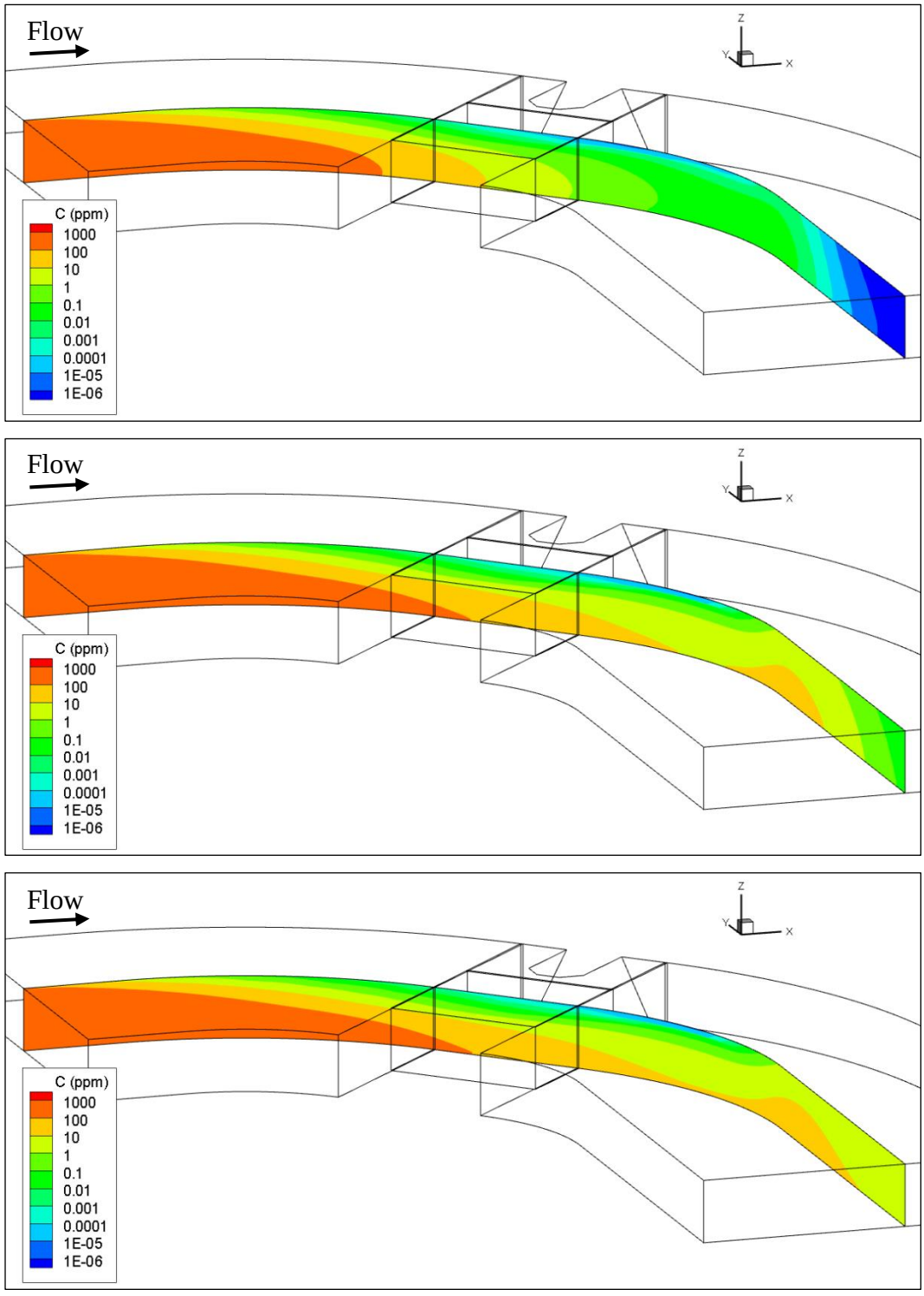

Fig. 5.9. Sediment concentration in the longitudinal mid-plane for d_{50} = 0.20 mm at t = 20 min. (top), t = 40 min. (middle), and t = 60 min. (bottom).

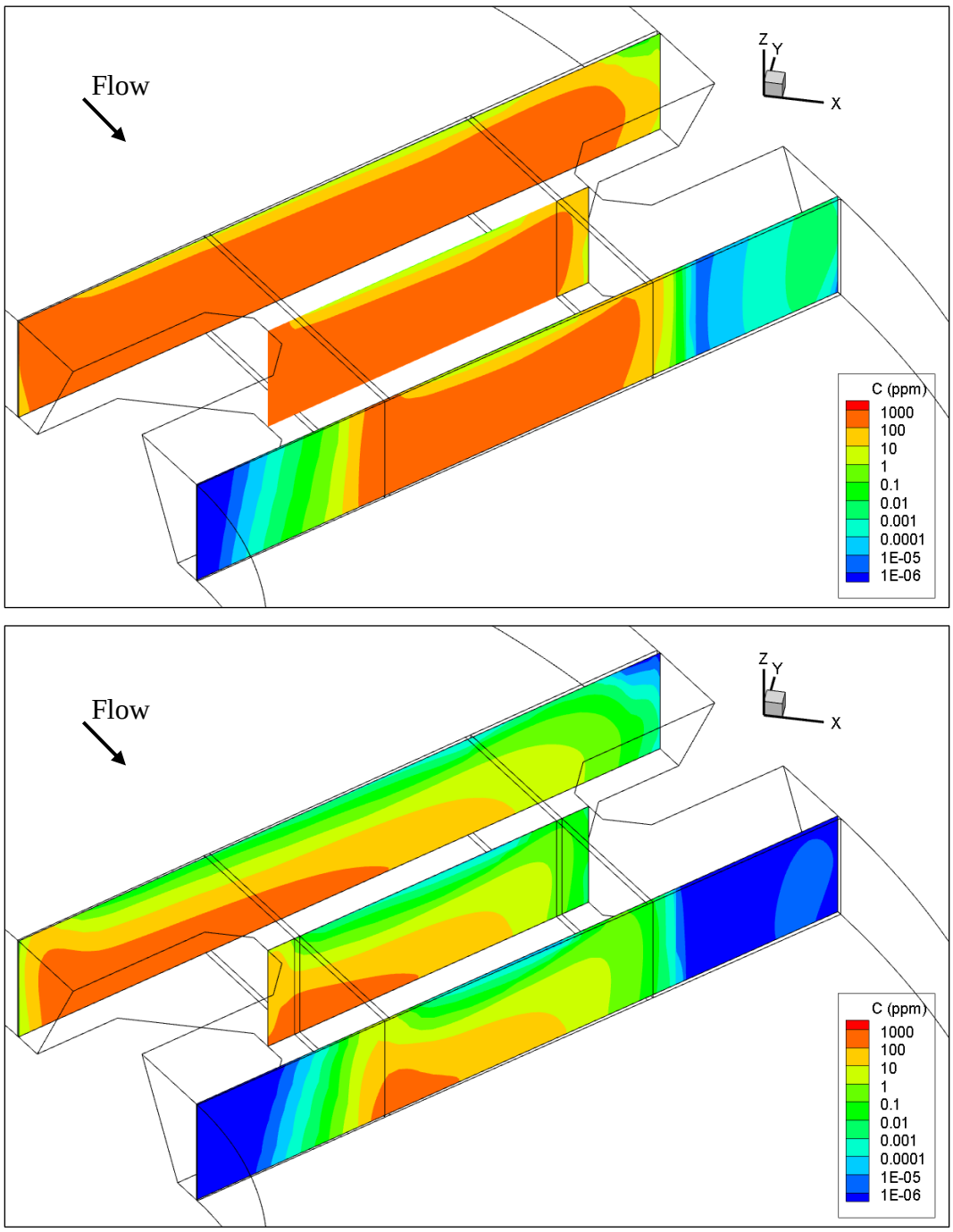

Fig. 5.10. Sediment concentrations near the abutments at t = 60 min. for d_{50} = 0.10 mm (top) and d_{50} = 0.20 mm (bottom).

5.1.6. Conclusions and Future Works

To improve the understanding of how suspended sediment is transported in a three-dimensional flow, simulation was conducted with two different median diameters, 0.10 mm and 0.20 mm, inside a channel bend with wingwall abutments. The domain is similar to the one used by Chen (2008) with several modifications, including removal of the overtopping elements and the depression in the channel centerline. The wall function approach was adopted in combination with the two-layer model for different components of the mesh. This study has presented the following contributions to the research community:

i. Wall function approach and the two-layer model, which utilize near-wall spacings that differ by orders of magnitude, were used together. The interpolation among blocks was successfully established by PEGASUS.

ii. The flow around wingwall abutments was simulated, including vortex shedding.

iii. The time series of concentration distribution of suspended sediment are provided in three dimensions. Locations of relatively high and low concentrations were identified.

Nevertheless, there is room for improvement for more comprehensive understanding of suspended sediment transport. Primarily, the implementation of bed boundary conditions that model the actual physical processes (entrainment and deposition) at the bed will bring new insight. Also, use of different channel configurations will help build additional practical knowledge.

5.2. Scour around Abutments

5.2.1. Introduction

The effects of sediment particle size on the scour depth around an obstruction were studied. Two different structures were considered: a wingwall abutment and a prismatic structure with a semi-cylindrical edge, as depicted in Fig. 5.11. Unlike the former, whose cross section tapers in the vertical direction, the latter has a constant cross section. Although such geometry is not employed in typical abutment designs (Tonias and Zhao, 2007), it contributes to the understanding of sediment transport processes. Thus, it will be termed and considered as a "round abutment" in the present discussion.

The effect of the diameter of a sediment particle on its mobility was studied extensively by Shields (1936). The Shields diagram, relating the critical shear stress required for the incipient motion of a particle to its diameter and the Reynolds Number, has paved the way for decades of sediment transport studies that followed. More recently, Briaud et al. (2001) and Briaud (2006) presented a set of curves that relate the critical flow velocity and shear velocity based on the erosion function apparatus experiments.

The relationship between particle diameter and the scour depths has been presented in experimental works including Melville and Chiew (1999), Florida Department of Transportation (FDOT) (2005), Sheppard et al. (2007), Lee and Sturm (2009), and Lança et al. (2011). In these experiments, the physical or dimensionless sediment particle sizes were varied and the scour depths around a cylindrical pier were measured. Scour around wingwall abutment was recently studied by Mazumder and Barbhuiya (2014), with four different sediment diameters.

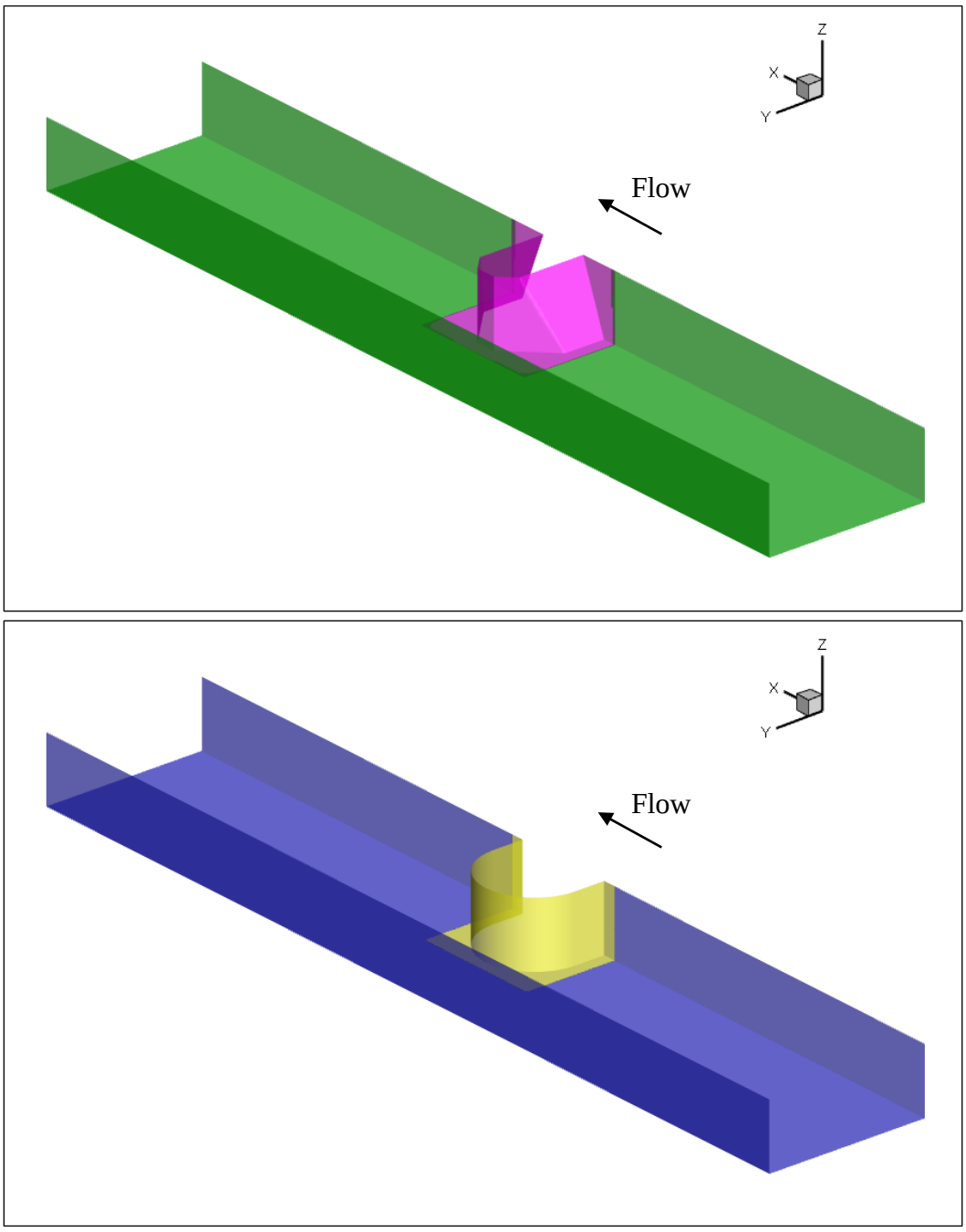

Fig. 5.11. Channel configuration: Wingwall abutment (top) and round abutment (bottom). Scale is magnified by factor of 5 in the vertical direction.

5.2.2. Flow Environment

The flow environment was identical to the experimental setup for the Experiment Case 9 discussed in Chen (2008) and Oh (2008), where a constant flow was maintained at the inlet of a 6 ft-long channel to observe cohesive scour around a wingwall abutment. In the current simulation, to generate a fully-developed flow profile, sufficiently long distance was provided between the inlet and the abutment. The initial flow depth and the approach velocity were 0.29 m and 0.43 m/sec, respectively. The geometry of the wingwall abutment was identical to the one presented in Section 5.1.

As can be seen in Fig. 5.11, the channel was rectangular and straight, bound with smooth sidewalls. The bed was covered with sediment particles as was in the experiment. It should be mentioned, however, that because the sediment type was different (cohesive vs. non-cohesive), the roughness effect was different from the experimental setup. In addition, the bed surface was initially flat for the current simulation.

The round abutment has a size comparable to that of the wingwall counterpart. For variability in sediment particle size, four different median diameters were adopted: 0.20 mm, 0.40 mm, 0.60 mm, and 0.80 mm. Their physical properties that have implications in the transport are summarized in Table 5.2.

Table 5.2. Physical characteristics of sediment with different median diameters.

d_{50} (mm)	Settling Velocity (cm/sec)	Critical Shields Parameter
0.20	2.38	0.056
0.40	5.72	0.038
0.60	8.16	0.034
0.80	10.07	0.031

5.2.3. Mesh

The simulation for this investigation was performed in a mesh consisting of the block associated with the abutment embedded within the rectangular channel block as shown in Fig. 5.12. A hole was generated within the channel block with PEGASUS, for which the solution is not obtained during simulation. In Fig. 5.12, the hole points have been "turned off" and thus are not visible. To improve interpolation between the two blocks, similar grid spacing was adopted in the vicinity of the interface.

It should be noted that while the original grid structure of the wingwall abutment mesh (compatible with the two-layer turbulence model) was maintained, the round abutment mesh was generated to be used with the wall function approach. Thus, a relatively large grid spacing was applied near the wall, $y^+ \approx 100$. The near-bed spacing, however, was set to $y^+ \approx 100$ for both meshes. The number of grid points for the two meshes are presented in Table 5.3. Here, the number of grid points include those in the hole region. The longitudinal, transverse, and vertical coordinate directions are denoted with ξ, η, and ζ, respectively.

Table 5.3. Number of grid points employed for the abutment scour simulations.

Block	Description	Wingwall			Round		
		ξ	η	ζ	ξ	η	ζ
1	Abutment	211	43	25	19	131	25
2	Channel	117	71	25	117	71	25
	Total	434,500			269,900		

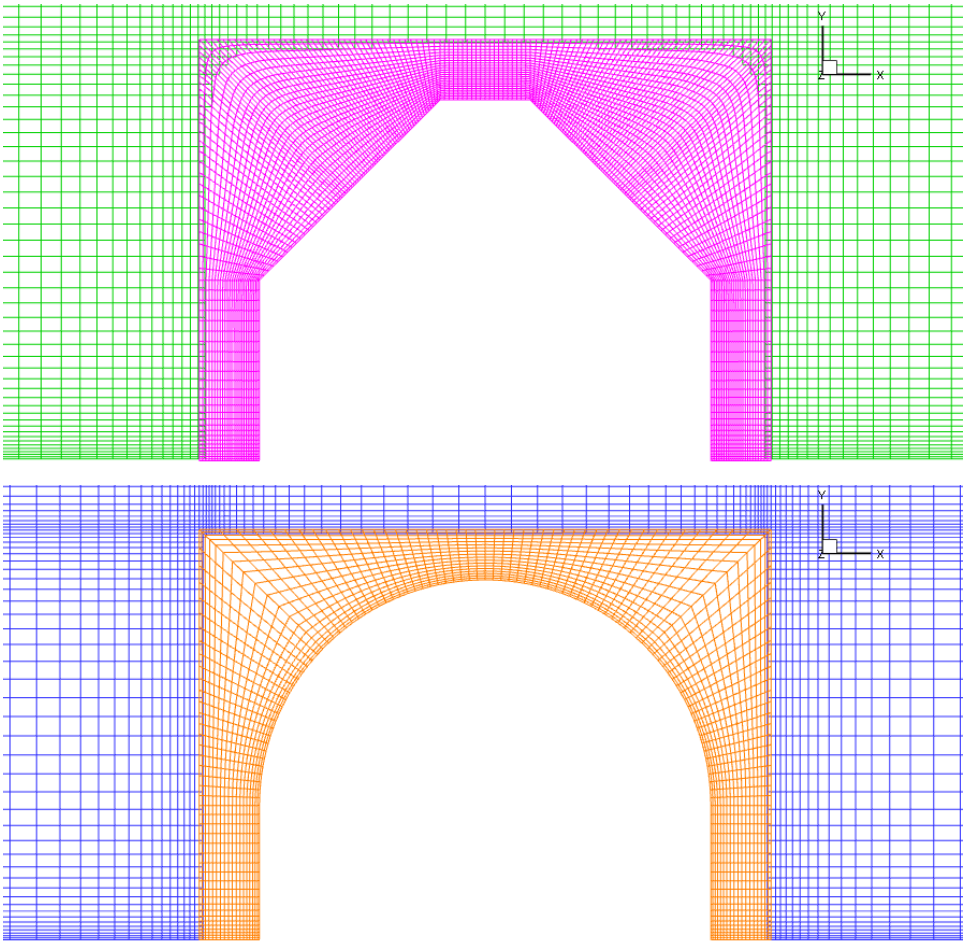

Fig. 5.12. Grid structure for the abutments: Wingwall (top) and round (bottom)

5.2.4. Simulation Setup

The characteristic length and velocity scales were set equal to the initial flow depth and approach velocity, respectively. The non-dimensional time step size, 0.2, led to the physical step size of 0.14 seconds.

The boundary conditions of the rectangular channel were set to mimic the physical flow conditions. At the inlet, logarithmic velocity was prescribed in the direction of the

approach flow, while the transverse and vertical velocity components were set to zero. At the outlet, the zero-gradient condition was used. The wall function approach was adopted for the sidewalls and the bed. The sidewall surfaces were assumed to be smooth. On the other hand, the two abutment types used different turbulence resolving schemes for the sidewall surfaces: the wingwall abutment used two-layer model, while the wall function approach was used for the round abutment. This is, again, due to the fact that the wingwall abutment mesh was originally generated to be used with two-layer model.

5.2.5. Results and Discussion

The hydrodynamics around the abutments are depicted in Fig. 5.13. The velocity vectors are placed at 25% and 50% of the initial depth above the bed. For both abutment types, strong downward flow is observed in the upstream half of the structure, which helps generate the horseshoe vortex. Around the midpoint along the radius of the structure, however, the turbulence caused the flow to accelerate upward. In the downstream face of the structure, downward flow is again observed.

While the overall hydrodynamics can be generalized as above, there are subtle differences resulting from the geometric characteristics of the abutment types. While the steep sidewall slope of the round abutment (i.e., the abutment surface is perpendicular to the bed) caused the velocity vectors to be pointing normal to the bed surface in the upstream and downstream faces, the relatively low angle of the wingwall abutment resulted in less abrupt changes in the vector directions. In addition, the transition from the downward to upward flows occurred sooner for the wingwall abutment.

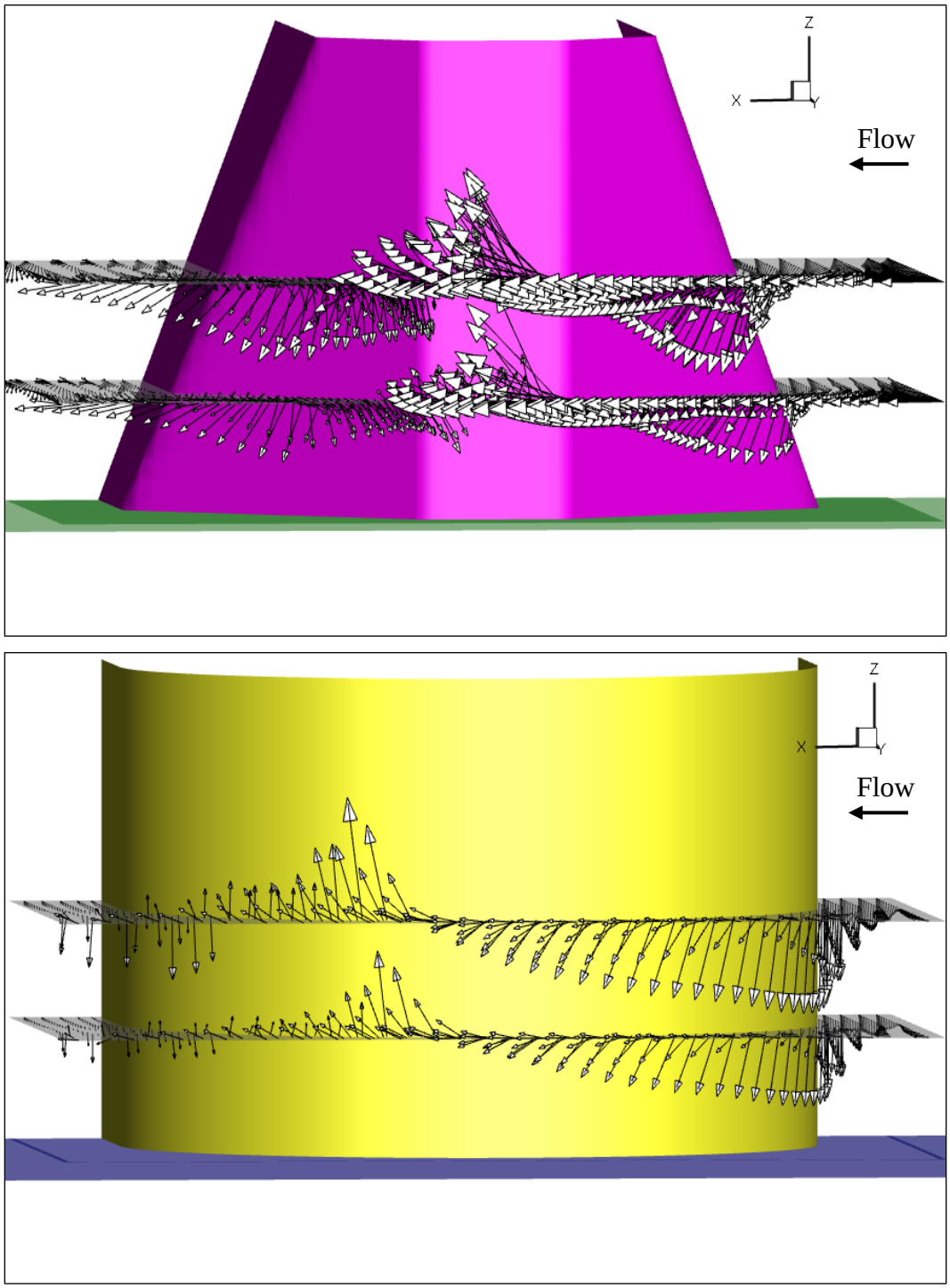

Fig. 5.13. Velocity vectors around the wingwall (top) and round (bottom) abutments.

The shear velocities associated with the different sediment particle diameters are compared in Figs. 5.14 and 5.15 for the wingwall and round abutments, respectively. The numeric values associated with the color contours represent the non-dimensional shear velocity; one can obtain the dimensional values by multiplying them by the characteristic velocity scale.

It was found that larger particle diameter generates higher shear velocity at a given location. This is due to the roughness effect of the particle. In the present study, the roughness height was set equal to three times the particle diameter (van Rijn, 1987), and according to Eq. (2.7), rougher surface generates higher shear velocity.

Another finding was that the overall distribution of shear velocity is consistent for a given abutment structure. For instance, for the wingwall abutment, the maximum shear velocity occurred around the upstream corner, marked "A" in Fig. 5.14, regardless of the sediment diameter. Extending from the Point A and trailing downstream, a long and thin streak of relatively high shear velocity is observed. Such phenomenon is caused by the turbulence induced by the sidewall (Koken and Constantinescu , 2014).

Similarly, for the round abutment, the maximum shear velocity occurred at the position marked "B" in Fig. 5.15. However, unlike with the wingwall abutment, downstream of the Point B, no streak of intensified turbulence is observed. The reason for the absence is that the "roundedness" of the structure prevents abrupt pressure gradient and formation of vortices. As a result, for any particular sediment diameter, the regions of high shear velocity are found to be more localized.

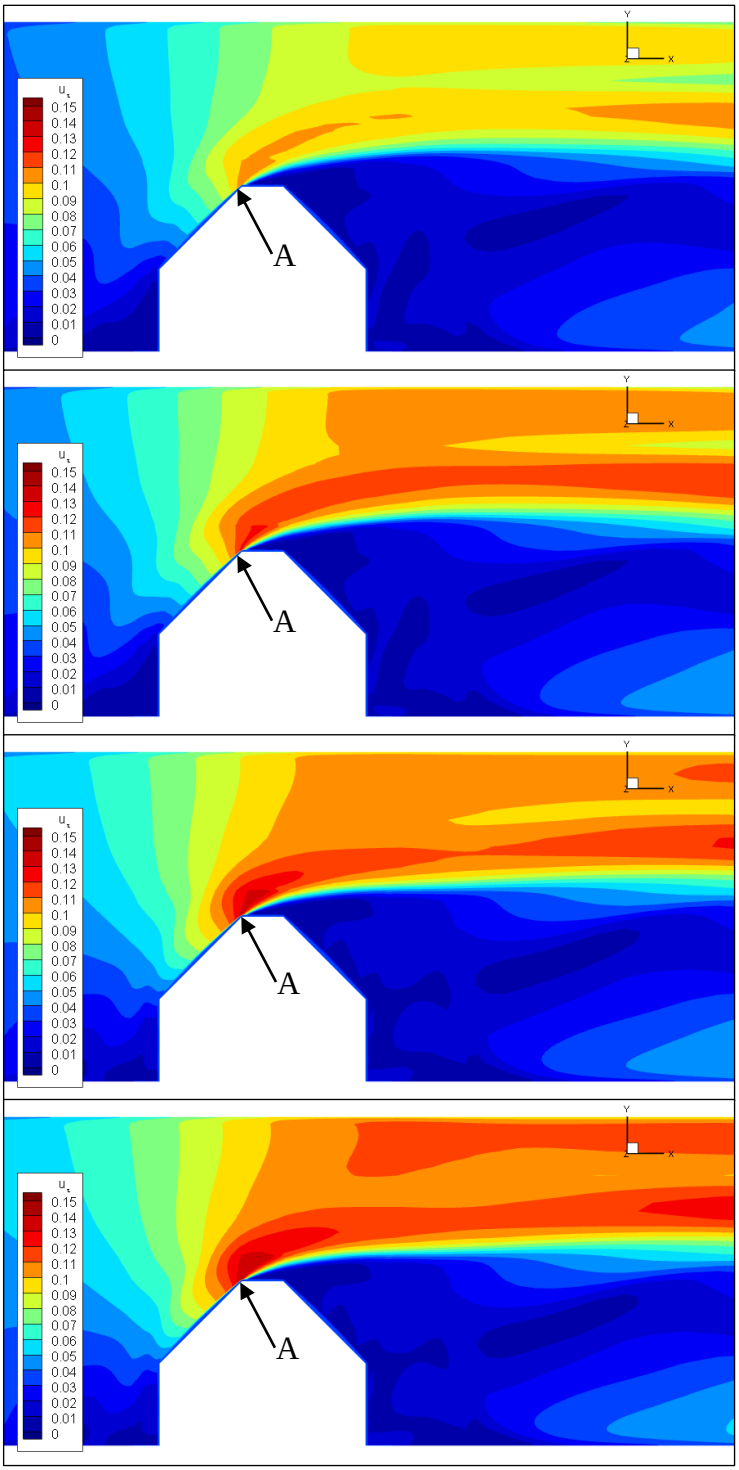

Fig. 5.14. Effect of median diameter on shear velocity around the wingwall abutment: (from top to bottom) 0.20 mm, 0.40 mm, 0.60 mm, and 0.80 mm. Flow direction is from left to right.

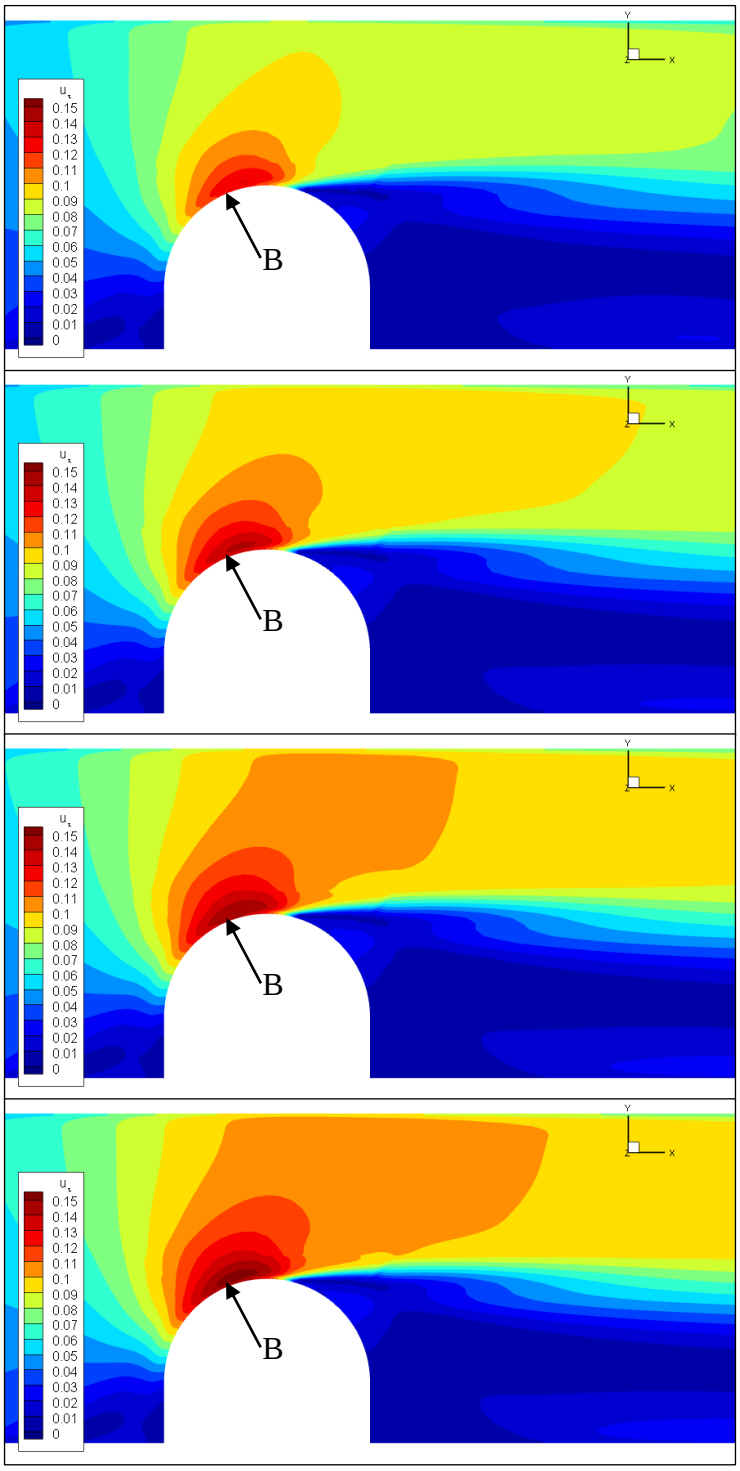

Fig. 5.15. Effect of median diameter on shear velocity around the round abutment: (from top to bottom) 0.20 mm, 0.40 mm, 0.60 mm, and 0.80 mm. Flow direction is from left to right.

Simulation of bed load transport in the given flow field showed that increase in sediment diameter leads to a deeper scour hole. As can be seen in Figs. 5.16 and 5.17 for the wingwall and the round abutments, respectively, d_{50} = 0.80 mm resulted in the deepest scour hole and d_{50} = 0.20 mm the shallowest. This relationship can be explained in terms of roughness, as was the case for the shear velocity: when the diameter is larger, the rougher surface creates more turbulence, which contributes to higher shear stress (Bates et al., 2005). FDOT (2005) also reported similar finding, where the normalized scour depth increased with larger normalized sediment diameter within a certain range. An everyday example of such phenomenon is the drag a person experiences when their arm is stretched out of the window of a moving vehicle.

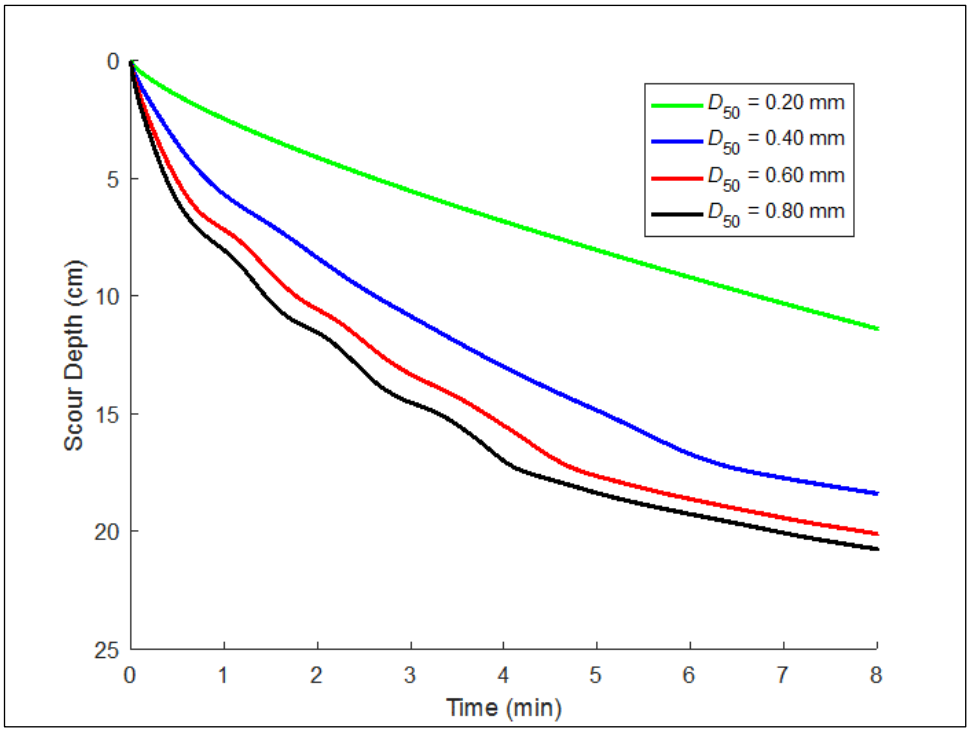

Fig. 5.16. Scour hole depth over time around the wingwall abutment.

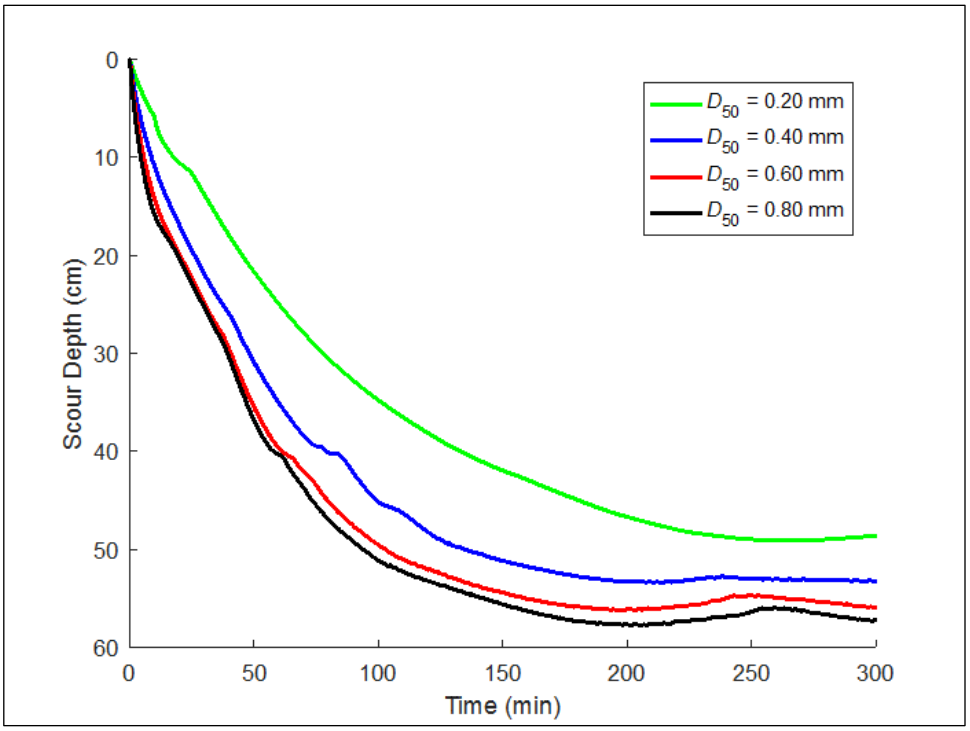

Fig. 5.17. Scour hole depth over time around the round abutment.

The initial rate of scour around the two abutment types is compared in Fig. 5.18. It can be seen that the wingwall generates deeper scour hole for all sediment diameters. Another key observation is the nonlinearity in the relationship between the sediment diameter and the consequent scour depth, which resembles the diminishing returns in economics. That is, at any given time, increasing the sediment diameter results in decrease in the marginal scour depth. This indicates that there is a threshold value above which the associated scour depth will start to decrease. In fact, this is represented as the peak of the curve in Fig. 5.19 (FDOT, 2005). Here, D_{50} = median diameter, D* = the effective diameter of the structure, and y_s = equilibrium scour depth.

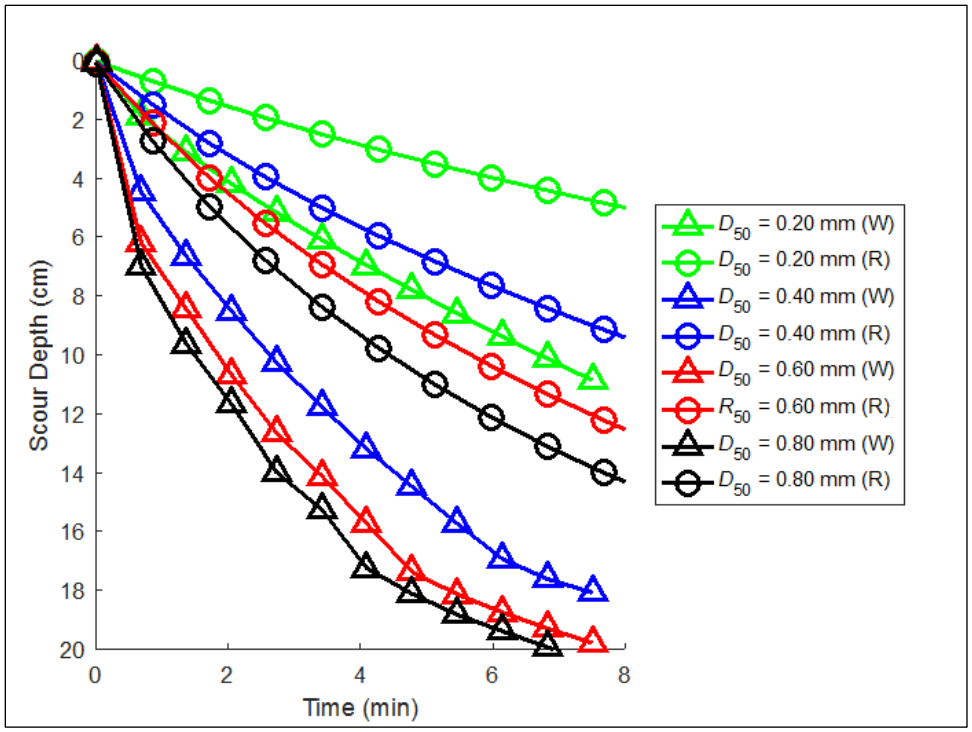

Fig. 5.18. Comparison of scour rates between the wingwall (W) and round (R) abutments.

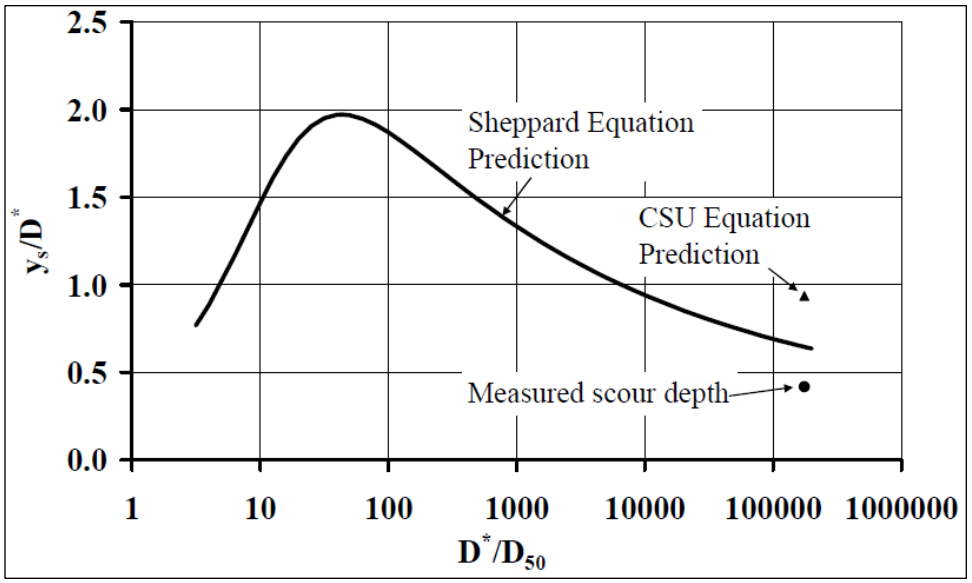

Fig. 5.19. Relationship between normalized median diameter and scour depth (FDOT, 2005).

With regards to Figs. 5.16 and 5.18, it should be noted that the results corresponding to only the first 8 minutes are presented. The reason is that for the wingwall abutment, extensive morphologic changes following a prolonged simulation resulted in certain numerical behaviors that do not represent the actual physical phenomena. However, the round abutment, with its simpler geometry (e.g., the shape of the cross section is uniform), did not cause any numerical instability during the simulation.

The plan views of the bed morphology around the wingwall and round abutments are presented in Figs. 5.20 and 5.21, respectively. It is shown that the general location of the maximum depth coincides with that for the shear velocity. Also, increase in diameter generates not only a deeper scour hole, but also a larger one. The scour hole area was visually determined as the region confined by the boundary with the zero-bed elevation.

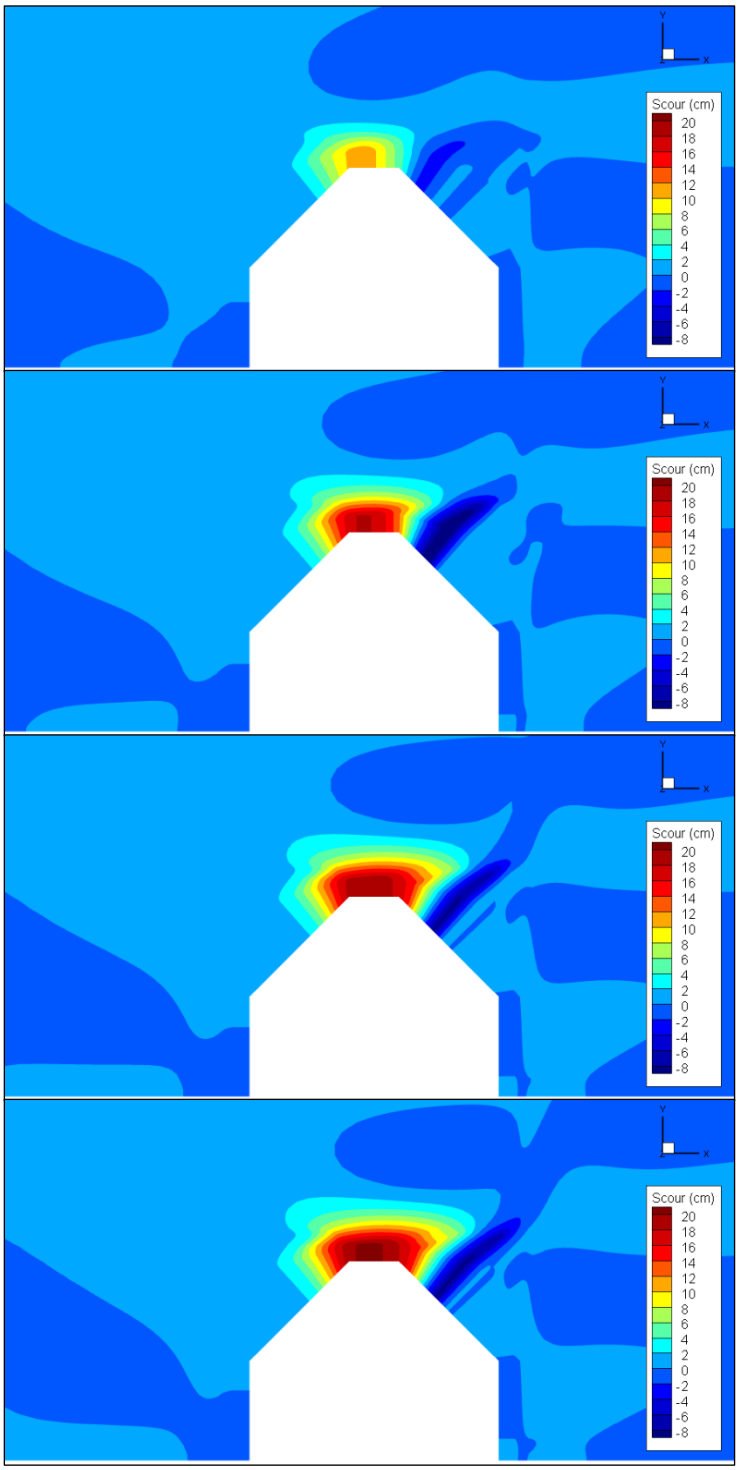

Fig. 5.20. Scour hole depth around the wingwall abutment at t = 8 min. The represented median diameters are (from top to bottom) 0.20 mm, 0.40 mm, 0.60 mm, and 0.80 mm. Flow direction is from left to right.

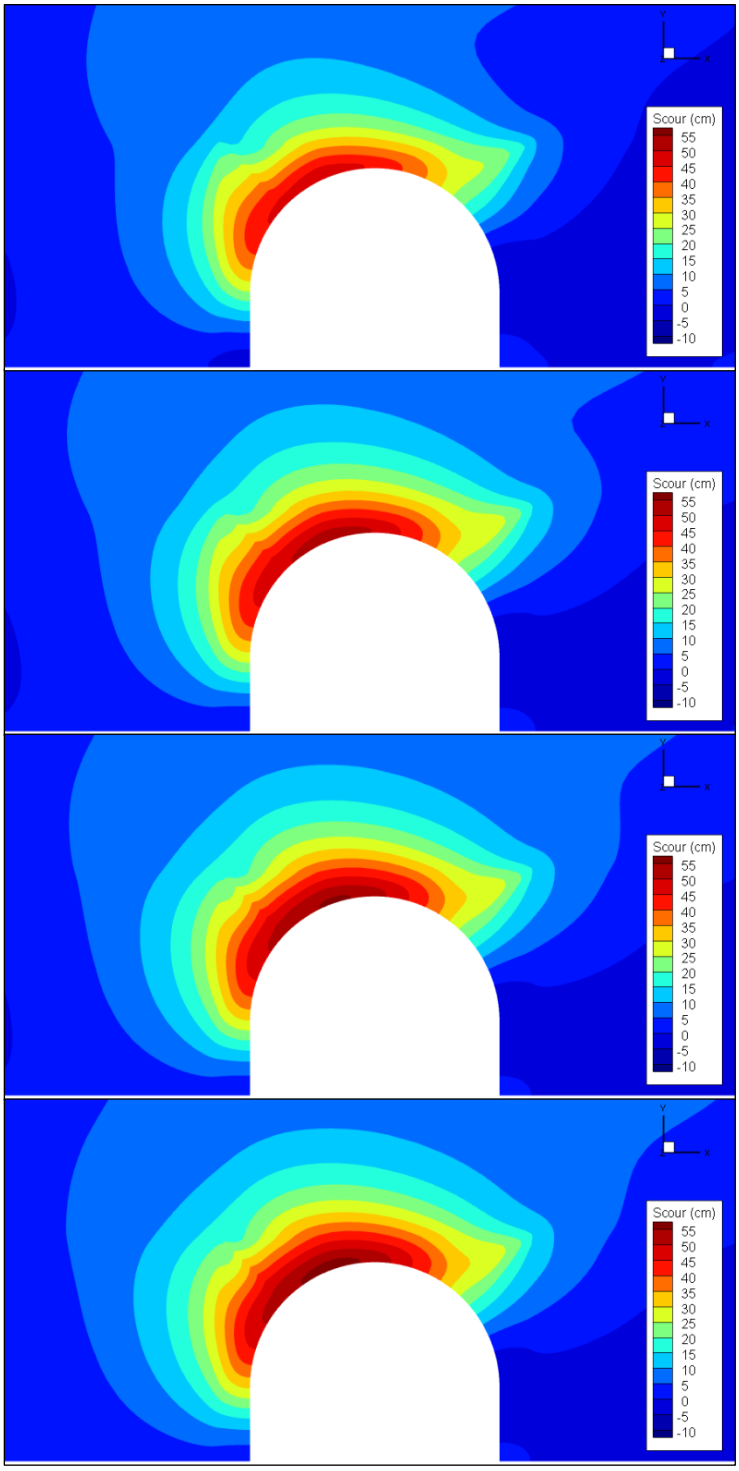

Fig. 5.21. Scour hole depth around the round abutment at t = 300 min. The represented median diameters are (from top to bottom) 0.20 mm, 0.40 mm, 0.60 mm, and 0.80 mm. Flow direction is from left to right.

5.2.6. Conclusions and Future Works

The purpose of the present study was twofold: first, to simulate scour around a wingwall abutment and a semi-cylindrical obstruction (treated as a round abutment), and to study the effect of sediment particle size on the scour processes. Four median diameters were considered: 0.20 mm, 0.40 mm, 0.60 mm, and 0.80 mm. Because the wingwall abutment mesh caused numerical instability during the scour simulation, the equilibrium scour depths were obtained only with the round abutment. The following are the main contributions this study is bringing:

i. It was shown that, among those considered, sediments with larger diameter generate higher shear stress and deeper scour holes. This is in agreement with FDOT (2005).

ii. The different geometries of the abutments, particularly with regards to the sidewall slope, generated different flow fields around them.

iii. The relatively sharp edge of the wingwall abutment generated a thin streak of high shear velocity in its wake due to turbulence.

One major weakness of this study is the fact that the scour around the wingwall abutment was terminated before the equilibrium depth was reached due to numerical instability. A new mesh with different structure may improve the stability.

5.3. Scour Hole Backfilling in Unidirectional Flow

5.3.1. Introduction

One out of nine bridges in the United States is structurally deficient (ASCE, 2013). With such a high number of bridges posing potential hazard to the millions of people who use them every day, scour is of a great interest in the field of civil engineering; according to a National Cooperative Highway Research Program report (Hunt, 2009), more than 20,900 U.S. highway bridges are scour-critical. However, the reported data may have been distorted by backfilling, the process in which an existing scour hole is filled as the approach velocity reduces and/or changes direction, and thus the reality may be worse. Because backfilling occurs in the final stage of flood, observations made during the normal flow condition may not represent the maximum scour depth (Foti and Sabia, 2014). The author believes that numerical simulation with CFD is the most viable approach in obtaining the maximum scour depth, as opposed to the final depth, in terms of cost and efforts involved.

There have been a number of numerical studies in the past that simulated sediment transport around vertical pier in steady current. Olsen and Melaaen (1993) used a finite volume method to simulate the flow around a cylinder in 3D and the resulting scour. At every iteration, a new grid was generated to account for the change in bed elevation, which was in turn used to update the flow field. Olsen and Kjellesvig (1998) computed the local scour depth using a 3D simulation and compared with several empirical formulas, which showed reasonable agreement. Jia et al. (2002) predicted the scour depth around a cylindrical pier using the CCHE3D model with k-ε turbulence closure. An empirical

relation was incorporated in the calculation of shear stress to capture the influence of the vertical wash around the structure. Roulund et al. (2005) investigated the flow and scour around a circular pile with both experiment and numerical simulation. ElipSys3D flow solver was used to calculate the flow field with k-ω turbulence model. For their morphologic model, the bed load equation by Engelund and Fredsøe (1976) was adopted. The flow characteristics around the pile on both rigid and mobile bed, as well as the scour development, showed good agreement with experiment. Zhao et al. (2010) also conducted study on scour around a cylinder both experimentally and numerically. The flow was solved with RANS equations with k-ω turbulence model. They noted horseshoe vortex and vortex shedding as the main factors governing scour process. Khosronejad et al. (2012) investigated the scour around piers of different shapes: cylinder, square, and diamond. FSI-CURVIB method with a k-ω turbulence model was used to simulate the flow. They included the aforementioned correction of shear stress by Jia et al. (2002). Pang et al. (2016), on the other hand, combined ANSYS-FLUENT with a Torczon optimization algorithm to numerically determine the equilibrium scour depth. Here, the Shields parameter around the pile is compared with the critical value to find the optimal value leading to the amount of bed deformation, rather than determining the fluid-particle interaction. Although this approach brings the benefit of reduced computation time, the model can only be applied to a cylindrical pile.

The numerical investigation of backfilling around a vertical pier was conducted only recently by Sumer et al. (2014). In their study, a scour hole developed around a pile under a steady current was backfilled when the flow switched to a wave condition. They

found that the flow with a particular Keulegan-Carpenter (KC) number results in a characteristic equilibrium depth, regardless of the initial bed morphology. The simulation utilized the fully-coupled CFD toolbox OpenFOAM using k-ω turbulence model, and the morphologic model included both suspended and bed loads. Ahmad et al. (2015) also observed wave-induced backfilling in their simulation of scour around multiple piles. However, their study focused on the effect of the pile placement on the scour depth, and thus the nature of backfilling was not discussed in detail. They used the REEF3D model, which employs the finite volume method to solve RANS equation with k-ε closure.

To the best of the author's knowledge, there are no numerical studies in the literature on backfilling of scour around a vertical pier under a current-only environment. It is thus the main purpose of this study to increase the understanding of its process through CFD for the first time. A novel approach to simulate backfilling is adopted, where a scour hole is first generated under a high flow velocity, then the velocity is reduced but still maintained above the critical value for sediment motion (live-bed condition). In turn, the sediment flux from the upstream fills the existing hole until a new equilibrium depth is reached.

5.3.2. Flow Environment

Flows with two different depth-averaged approach velocities and the subsequent sediment transport processes were simulated: $\boldsymbol{U_{flood}}$ = 2 m/sec (flood), $\boldsymbol{U_{normal}}$ = 1 m/sec (normal). The two approach velocities were selected with the intention to maintain live-bed scour; they both exceed 0.33 m/sec, the critical value for incipient motion for the particle size considered in the study (d_{50} = 0.85 mm) (Briaud, 2013). For backfilling, a

time-varying hydrograph is adopted in which the flow switches from the flood to the normal condition. The transition of the approach velocity is made after the equilibrium scour depth has been reached under the flood condition ($z_{eq,flood}$). As such, sediment particles would continue to roll into the scour hole generated under the flood until a new equilibrium depth ($z_{eq,backfill}$) is reached. The backfilled depth is the difference between $z_{eq,flood}$ and $z_{eq,backfill}$. The theoretical relationship between the flow conditions and the respective equilibrium scour depths is depicted in Fig. 5.22. The depth of the approach flow was 50 cm. The pier diameter (D) was also 50 cm, creating a one-to-one ratio with the flow depth. The Reynolds numbers for the flood and normal flow were 900,000 and 450,000, respectively.

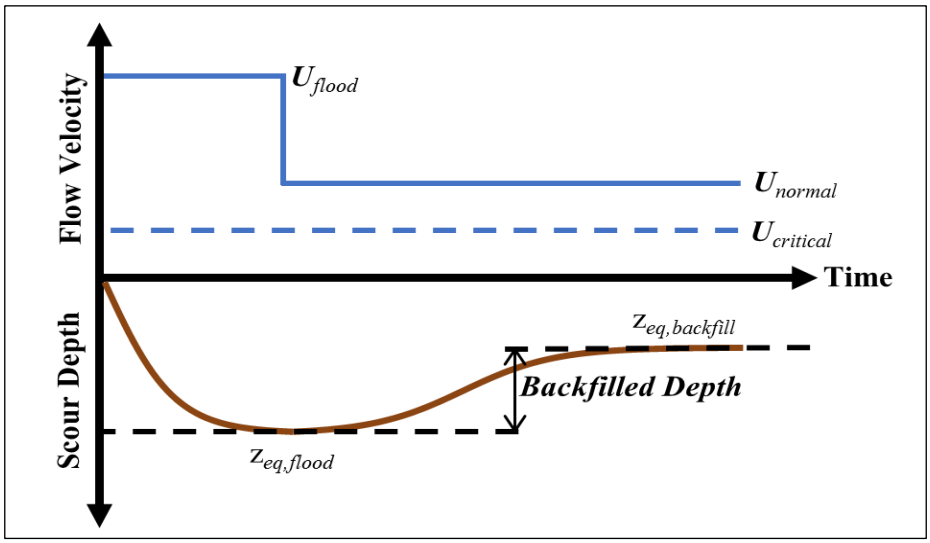

Fig. 5.22. Relationship between approach flow velocity and the associated equilibrium scour depth under unidirectional flow.

The sediment considered in the study is non-cohesive sand with d_{50} of 0.85 mm. The settling velocity is 10.5 cm/sec following Zanke (1977). The porosity is 0.4 with the density of 2,650 kg/m^3. The critical velocity for incipient motion is 0.33 m/sec as mentioned above (Briaud, 2013).

5.3.3. Mesh

The flow regime measured 21*D* in length and 6*D* in width. The domain boundaries were located at considerable distances away from the pier in order to minimize boundary condition effect on scour; the inlet, outlet, and right-side boundary were located 12*D*, 9*D*, and 6*D*, respectively, from the center of the pier.

Verification of the numerical solution was conducted by analyzing its sensitivity to different domain densities (497,385 and 330,183 grid points for high- and low- density grids, respectively) and dimensionless time step sizes (with a difference by a factor of 2). In total, six different simulations were conducted, with their computational environment summarized in Table 5.4.

Table 5.4. Computational environment for each of the pier scour simulation cases.

Case	Flow Condition	Grid Density	Time Step
A1	Normal	High	0.20
A2	Normal	Low	0.20
A3	Normal	Low	0.40
B1	Flood	High	0.15
B2	Flood	Low	0.15
B3	Flood	Low	0.30

5.3.4. Simulation Setup

At the inlet, a fully-developed velocity and turbulence profiles, obtained beforehand by a CFD simulation in absence of the pier, were used as the inlet condition. Both the transverse and vertical components of the velocity were set to zero. At the outlet, the zero-gradient condition was imposed for all velocity components and turbulence quantities. The same condition was used for the sidewalls, except for the transverse velocity component, which was set to zero. At the surface of the bed and the pier, the aforementioned wall function approach was used to specify the boundary values. Lastly, the top surface was treated as a rigid lid, with zero-gradient condition imposed for all velocity and turbulence quantities, except for the vertical velocity component, which was zero.

5.3.5. Results and Discussion

Hydrodynamics

For each flow condition, the fully-developed hydrodynamics solutions obtained from the respective three simulations (Cases A1-A3 for normal and B1-B3 for flood) agreed extremely well with one another. The shear stress τ distributions around the pier for Cases A1 and B1 at the onset of scour (i.e., the bed is rigid and no sediment transport has occurred) are compared in Fig. 5.23. For both cases, the maximum shear stress τ_{max} is found at the position corresponding to $\boldsymbol{\Phi} \approx 70°$. This is attributed to the combination of the contraction of streamlines and the presence of horseshoe vortex (Breusers et al., 1977; Roulund et al., 2005). The τ_{max} for Case A1 is four times as high as that for Case B1, since shear stress is proportional to the square of the shear velocity (Eq. 3.1).

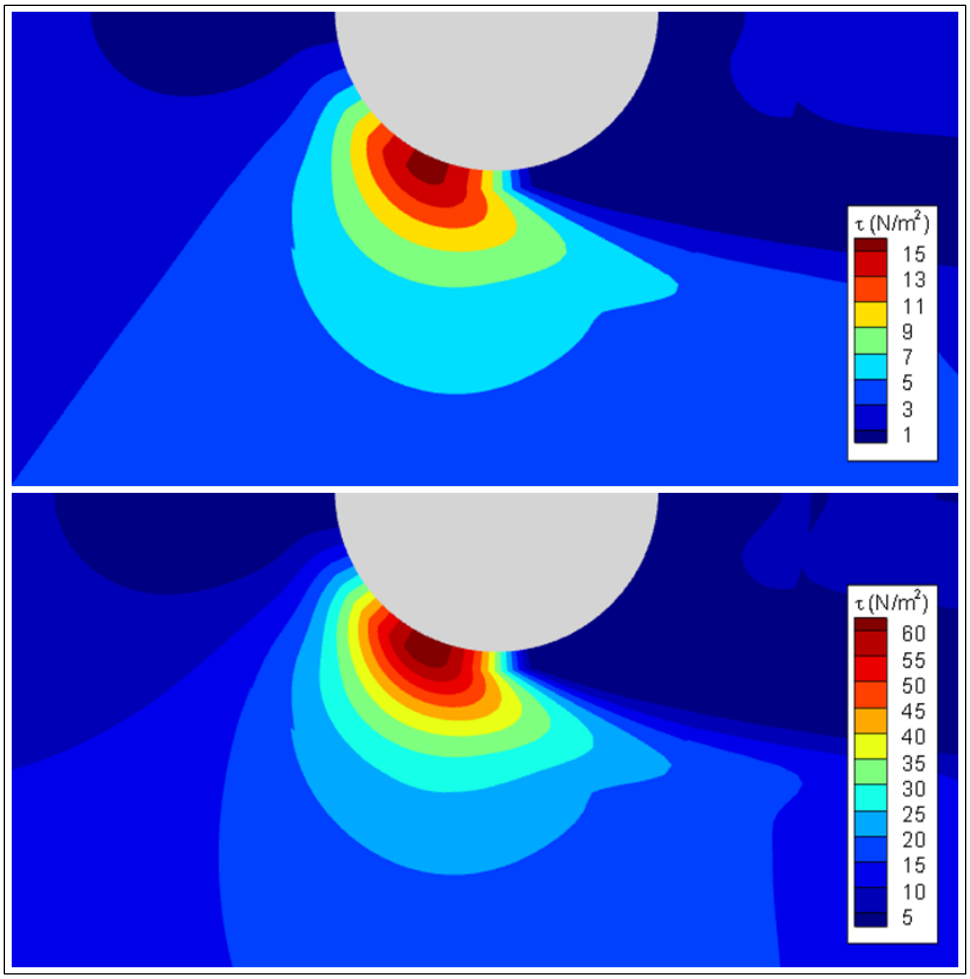

Fig. 5.23. Shear stress distribution around the pier at the onset of scour (Top: Case A1; bottom: Case B1). Flow direction is from left to right.

The fluid-structure interaction is further studied with Case B1 in Figs. 5.24 and 5.25. As shown in Fig. 5.24, the horseshoe vortex at the upstream edge of the pier is resolved well. The velocity vectors indicate the strong downwash along the surface of the pier and the direction of the flow towards the saddle point. The separation distance is 0.75*D* measured from the center of the pier. Fig. 5.25 shows the wake vortex system, generated when the unstable shear layers are detached from the surface of the pier

(Breusers et al., 1977). The nature of the vortex systems presented herein agrees well with previous reports (Breusers et al., 1977; Baker, 1980; Eckerle and Langston, 1987; Roulund et al., 2005; Zhao et al., 2010).

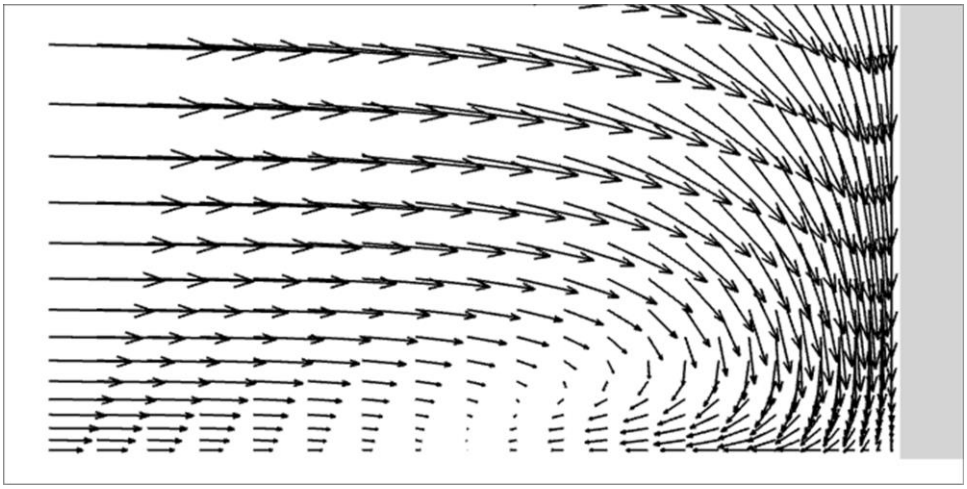

Fig. 5.24. Horseshoe vortex near the upstream base of the pier. Flow direction is from left to right.

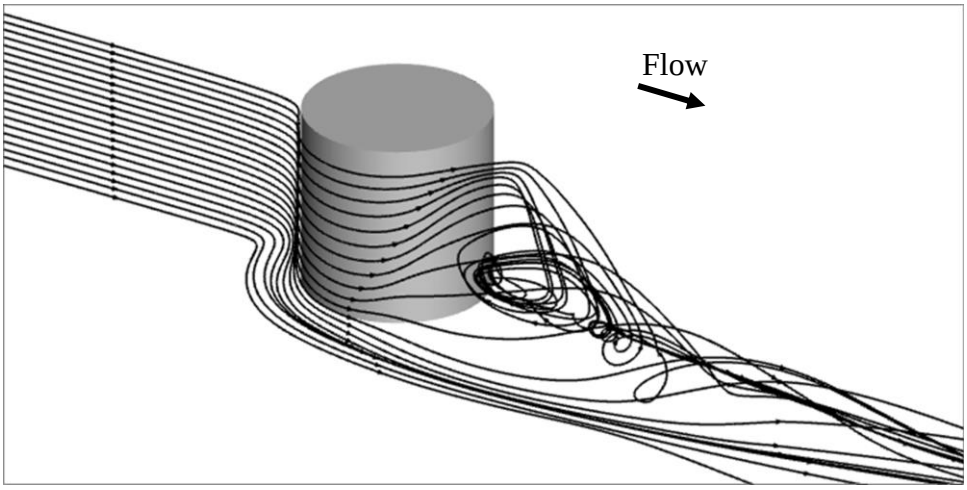

Fig. 5.25. wake vortex in the downstream of the pier. A full pier, as opposed to the half-domain used in the actual computation, is placed for visualization purpose.

Pier Scour

The time series of scour depths under the two flow conditions are presented in Fig. 5.26. It was deemed that equilibrium has been reached if the change in the scour depth during any 15-min. period of time does not exceed 1% of *D*. For both flow conditions, the variability in the grid density nor time step size does not have significant effect on the simulation results; the equilibrium depths are within 4% of *D* from one another. However, higher degree of sensitivity is observed with the change in grid density. This is evidenced by the virtually identical equilibrium depths associated with the same grid density but different time step size (A2-A3 and B2-B3 pairs). On the other hand, reducing only the grid density while keeping the time step size constant resulted in a shift in the equilibrium depths (A1-A2 and B1-B2 pairs). From this sensitivity analysis, Cases A3 and B3 are chosen to represent the respective flow conditions for comparison. Accordingly, the equilibrium scour depths $\mathbf{z}_{eq,normal}$ and $\mathbf{z}_{eq,flood}$ are 56.1 cm and 70.4 cm, respectively. The difference is 28.6% of *D*. Scour under the flood condition reached the equilibrium much quicker at $t \approx 30$ min., compared with $t \approx 50$ min. under the normal flow.

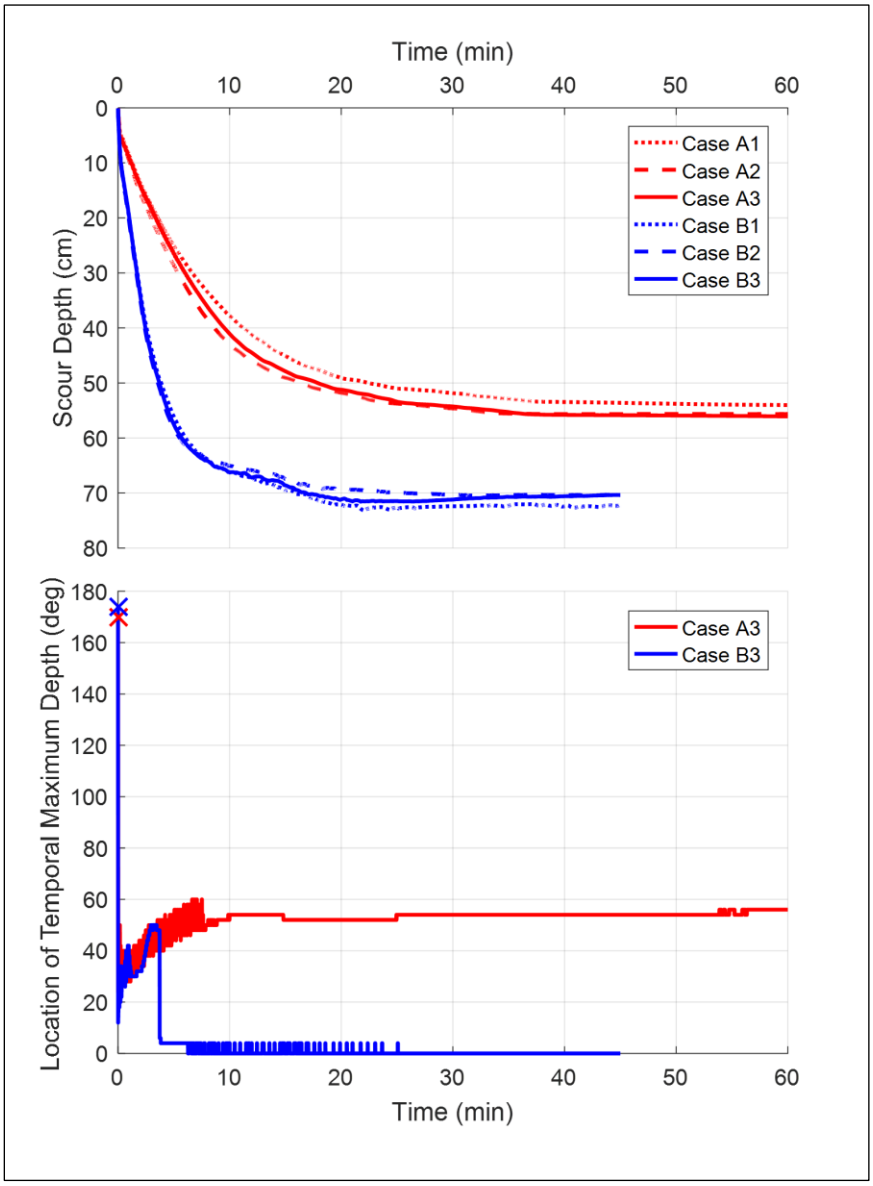

Fig. 5.26. Top: Time series of the maximum scour depth for normal (Cases A1, A2, and A3) and flood (Cases B1, B2, and B3) flow conditions. Bottom: Location of the maximum scour depth corresponding to each flow condition.

Also shown in Fig. 5.26 is the time series of $\boldsymbol{\Phi_z}$, the location of the maximum scour depth at a given time (not to be confused with the maximum scour depth of a given flow condition). At the start of the scour, $\mathbf{z}$ for both flow conditions is found at $\boldsymbol{\Phi} \approx 170°$, radially $1.0D$ away from the pier's center. Dargahi (1990) similarly observed the initial scour around a cylinder to occur in its wake, which was attributed to the primary wake vortices. Immediately afterward and until $t \approx 1.5$ min., the value of $\boldsymbol{\Phi_z}$ oscillates within the range between $20° \leq \boldsymbol{\Phi} \leq 40°$. What follows is an interesting phenomenon and a striking difference in the scour patterns between the two flows. For Case B3, $\boldsymbol{\Phi_z}$ sharply increases to 50° then immediately drops to 6°. Within 20 min., Case B3's $\boldsymbol{\Phi_z}$ converges to 0°, which corresponds to the upstream nose of the pier. On the other hand, for Case A3, $\boldsymbol{\Phi_z}$ undergoes gradual increase while oscillating within a 10° interval, until reaching an equilibrium of 56° ($\boldsymbol{\Phi_{z,eq}}$). With respect to the radial direction, the temporal maximum depths after the initial scour occur at the interface between the pier and the bed.

It is noted that $\boldsymbol{\Phi_z}$ does not reach ≈ 70°, where the maximum shear stress is found at the onset of scour, nor does it converge to ≈ 45° in the early stages, as reported in the literature (Dargahi, 1990; Escauriaza and Sotiropoulos, 2011). This is due to the fact that even in the far-field, the flow environment creates a live-bed condition. As such, $\boldsymbol{\Phi_z}$ occurs where the oncoming sediment flux is insufficient to replenish the locally eroded volume, rather than coinciding with the location of the highest shear stress. The oscillation in $\boldsymbol{\Phi_z}$ is caused by ripples associated with the live-bed condition.

The bed morphology around the pier is further investigated with Figs. 5.27 and 5.28 for Cases A3 and B3, respectively. Case A3 is discussed first. At $t = 5$ min., there is

an area of deposition downstream of the pier, with the maximum height of ≈15 cm (measured from the initial flat bed). The "mound" has been formed by the particles eroded from near the base. At t = 20 min., the mound has travelled further downstream and the wake scour is clearly observed. As flow continues, the part of the scour hole downstream of the pier becomes more elongated.

Fig. 5.28 also shows that the eroded material from around the pier generates a deposit in the downstream at t = 5 min. However, because of the higher velocity (2 m/sec vs. 1 m/sec), the mound is located further downstream compared to Case A3. The mound is also larger in size, but the maximum heights are similar between the two cases, at ≈15 cm. At t = 10 min., as with Case A3, the mound travels further downstream and the scour hole becomes larger. The location of the temporal maximum depth is clearly observed at the upstream nose of the pier. At t = 15 min. and 20 min., both the area and depth of scour increase. Most notably, the boundary between the flat bed and the scour hole is located significantly further upstream for Case B3. This poses implications in the backfilling process, as discussed in the next section. The widths of the scour holes (in the transverse direction), on the other hand, do not differ significantly between the two Cases.

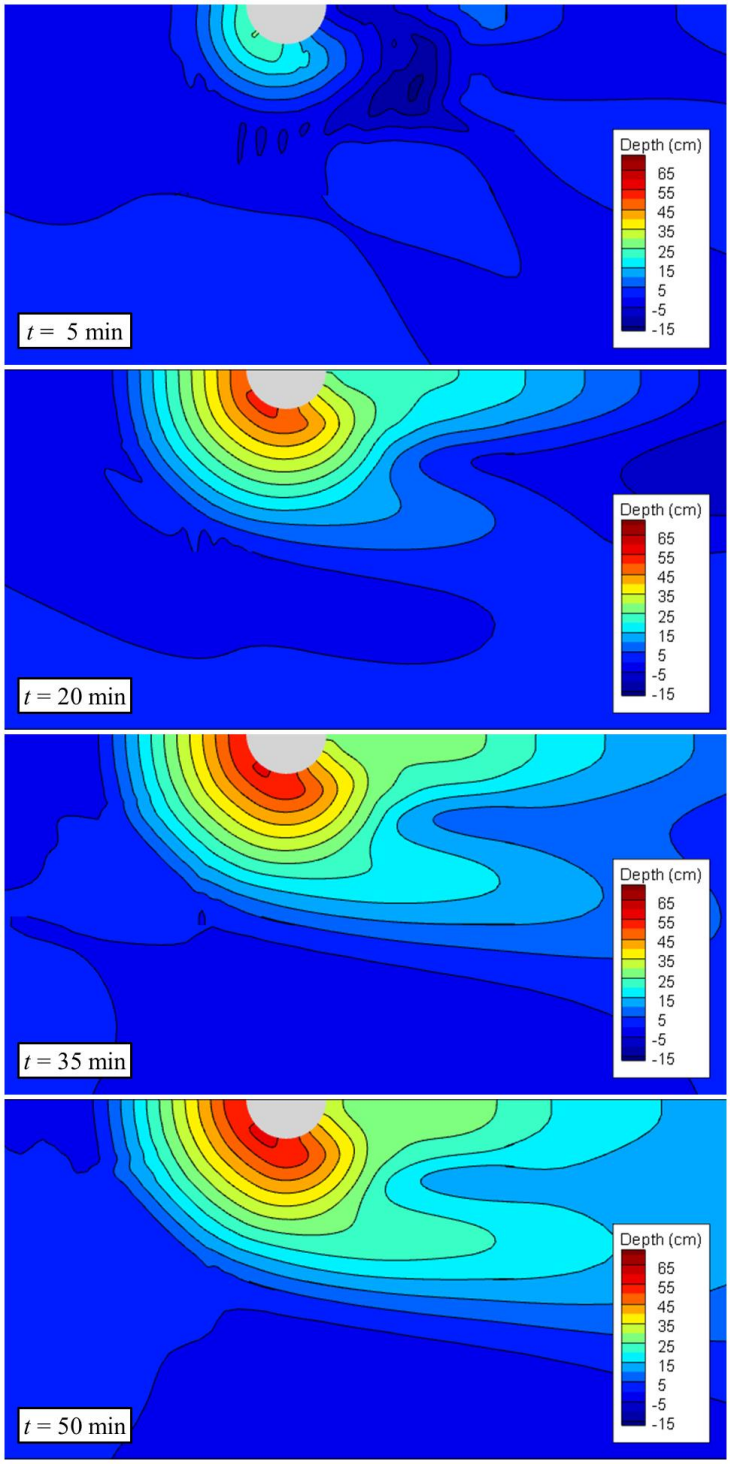

Fig. 5.27. Time series of bed morphology for normal flow condition (Case A3). Flow direction is from left to right. Negative depth indicates above initial bed level.

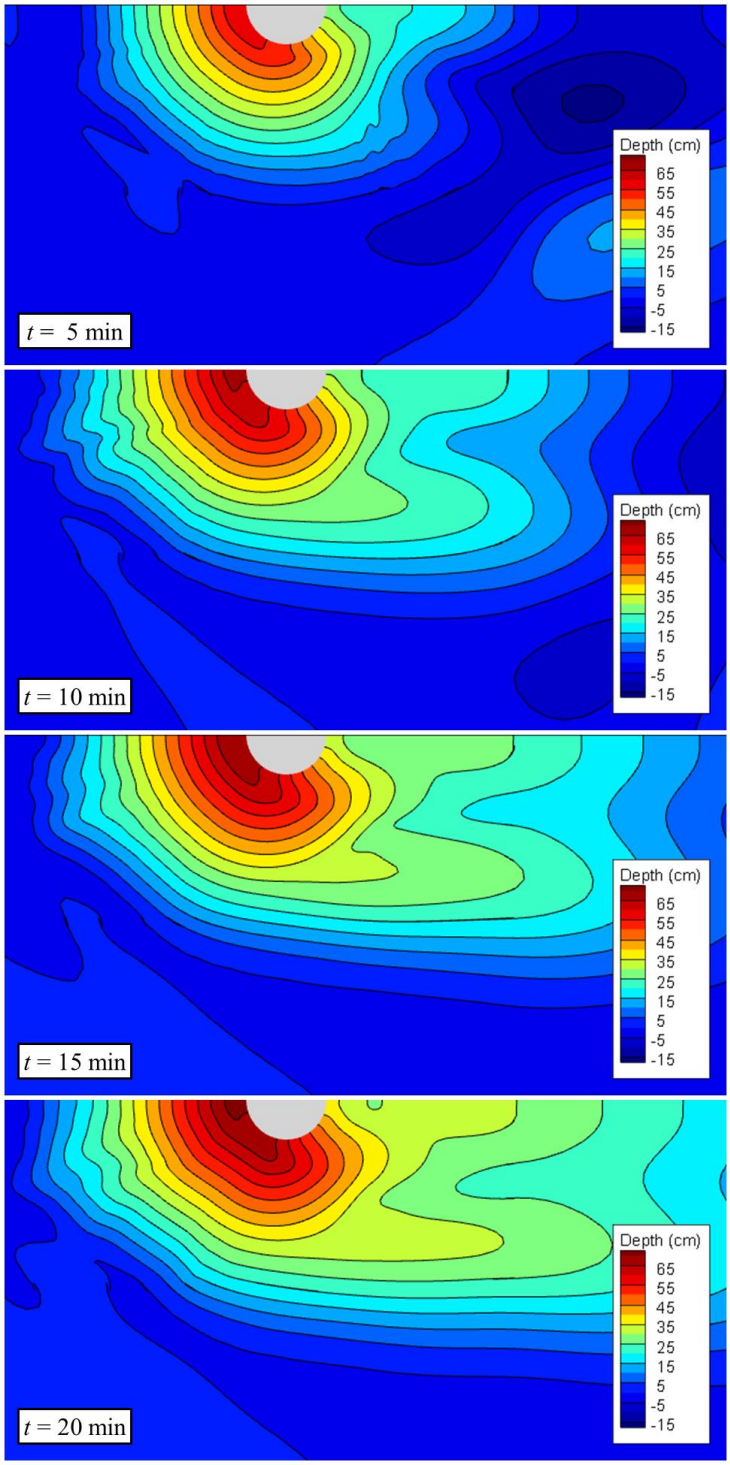

Fig. 5.28. Time series of bed morphology for flood flow condition (Case B3). Flow direction is from left to right. Negative depth indicates above initial bed level.

Backfilling

After Case B3 has reached the equilibrium, the resulting morphology was used to simulate backfilling. It began by first obtaining a fully developed flow with $\boldsymbol{U_{normal}}$ while keeping the bed rigid. Then, sediment transport was commenced. To allow for a systematic comparison with the scour under $\boldsymbol{U_{normal}}$, the same time step size as in Cases A3 was used. Fig. 5.29, the time series of $\mathbf{z}$ and $\boldsymbol{\Phi_z}$ during backfilling, sheds light on the different physical processes that take place around the pier. To facilitate discussion, the total duration is divided into three stages based on the trend in $\boldsymbol{\Phi}$ (also indicated on the Figure).

Stage I, which spans from $t = 0$ to $t \approx 30$ min., corresponds to the period in which $\boldsymbol{\Phi_z}$ remains at 0°. The scour depth decreases from 70.6 cm to 65.2 cm. However, it is relatively constant for the initial 6 min. This is attributed to the time it takes for sediment particles to collect near the upstream edge of the scour hole until the local slope reaches the angle of repose. Once the slope of the entire face reaches the angle of repose, the deepest part of the hole begins to be backfilled due to sand slide. This phenomenon occurs only because the equilibrium scour hole generated by the flood flow has a slope less than the angle of repose in the said region. Had the slope been equal to the angle of repose, the scour depth will be backfilled immediately.

Stage II begins with the sudden shift of the location of the temporal maximum depth from the upstream nose towards the wake of the pier. In the approximately 100-min. period, $\boldsymbol{\Phi_z}$ then gradually increases from 82° to 106°. The backfilled depth is 6.3 cm. The rate of backfilling is relatively constant, as can be seen by the linear relationship between scour depth and time in the Figure.

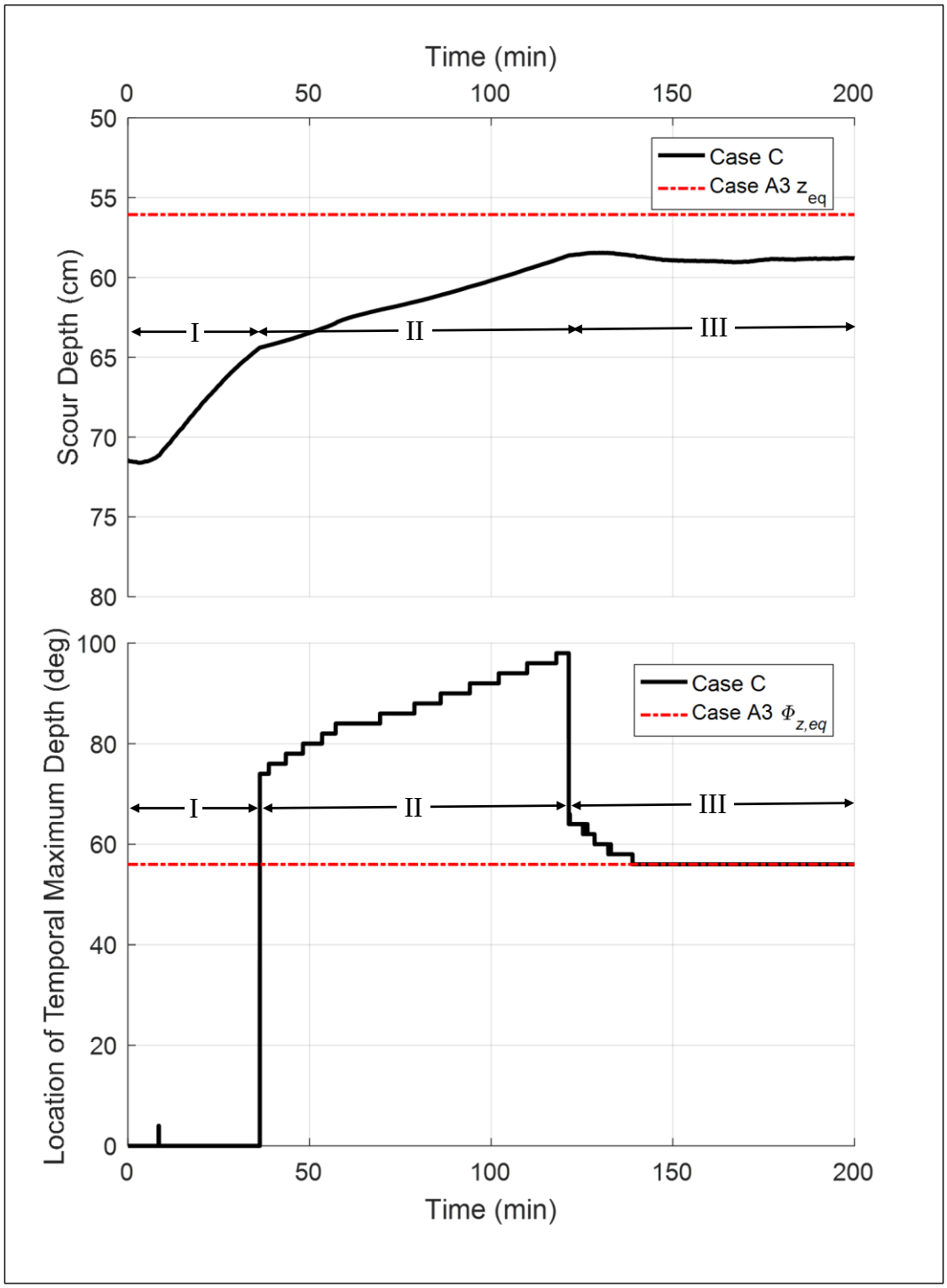

Fig. 5.29. Top: Time series of the maximum scour depth during backfilling. Bottom: Corresponding location of the maximum scour depth. Both $\mathbf{z}$ and $\boldsymbol{\Phi}_{\mathbf{z}}$ under backfilling converge to their Case A3 counterparts.

In Stage III, backfilling continues until reaching $\mathbf{z}_{eq}$ of 59.0 cm. The error between $\mathbf{z}_{eq,backfill}$ and $\mathbf{z}_{eq,normal}$ is 2.9 cm (5.8% of *D*). This is similar to observation made by Sumer et al. (2013) with oscillating flow, where the backfilled equilibrium depth for a given KC number was equal to the equilibrium scour depth with an initially flat bed with the same KC number. Meanwhile, $\boldsymbol{\Phi}_{\mathbf{z}}$ sharply drops to 64° then soon converges to an equilibrium value of 56°, with minimal fluctuation. It should be stressed that this value is equal to $\boldsymbol{\Phi}_{\mathbf{z}}$ under $\boldsymbol{U}_{normal}$. The temporal maximum depth remains at the pier-bed interface throughout. To the best of author's knowledge, this is the first report revealing both the equilibrium depth and its location for a given flow velocity to be independent of the initial bed morphology. The total backfilled depth is 11.4 cm, corresponding to 22.8% of *D*. Time scale to reach the backfilled equilibrium (≈ 200 min.) is considerably greater than those associated with scour (< 60 min.).

The overall bed morphology pre- and post- backfilling are presented in Fig. 5.30, along with the equilibrium morphology of A3 for comparison. The Figure shows that the boundary between the flat bed and the scour hole advances downstream during backfilling. As a result, the size of the scour hole upstream of the pier contracts in the longitudinal direction. The width of the hole also becomes narrower, particularly in the downstream. On the other hand, the depth in the wake region remains relatively constant, indicating that the backfilling process takes place mostly in the vicinity of the pier and upstream. The post-backfilling and Case A3 results show remarkable agreement in the general size and shape of the hole upstream of the pier. In the wake region, however, Case A3 features higher elevations. It can be deduced that if the normal flow condition is to be sustained for

an extended period of time after the equilibrium scour depth is reached, the wake vortex will cause further scour downstream of the pier.

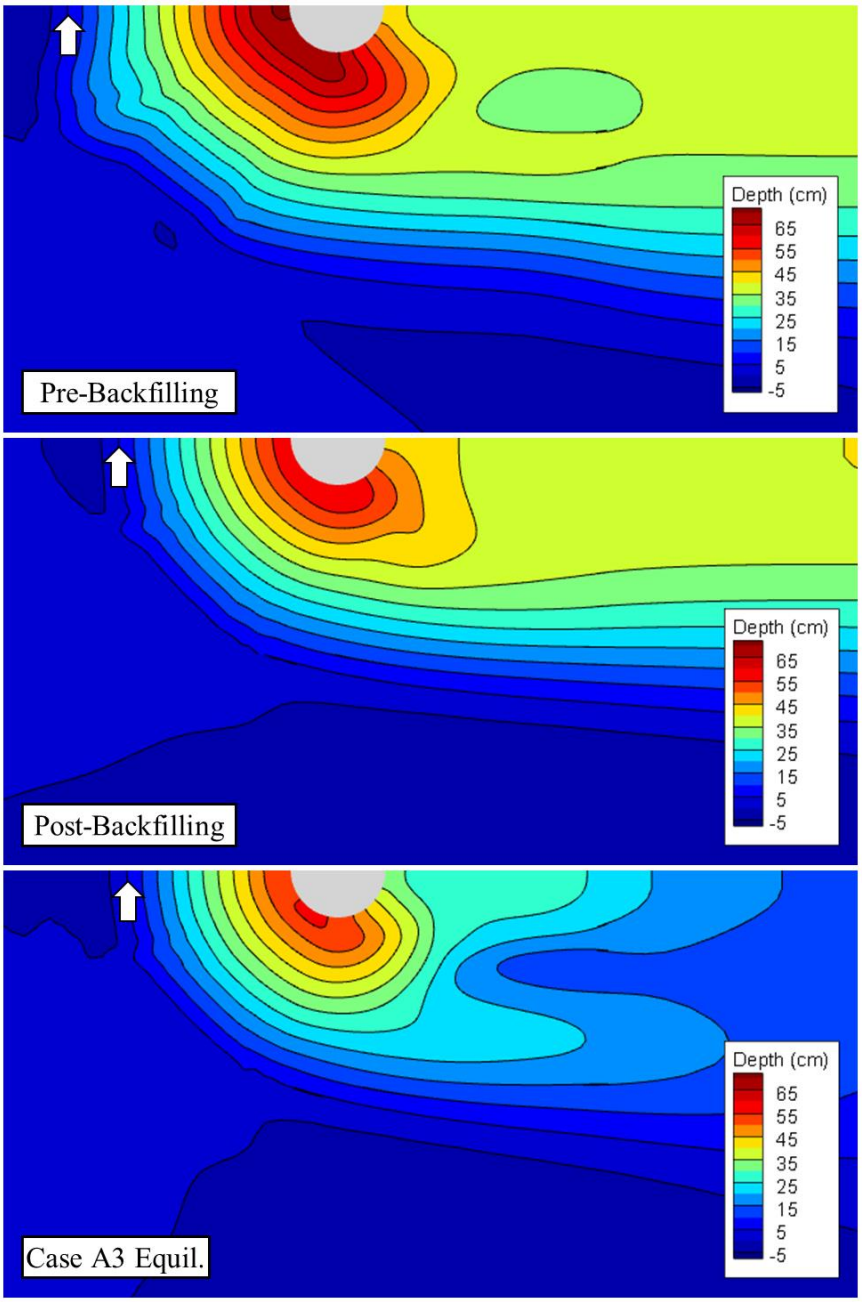

Fig. 5.30. Bed morphology before backfilling (top), after backfilling (middle), and for Case A3 at equilibrium (bottom). White arrow is placed at the scour hole boundary. Flow direction is from left to right.

5.3.6. Conclusions and Future Works

The three-dimensional CFD solver FANS3D was employed to simulate scour hole backfilling under unidirectional flow. The coupled sediment transport model determines the rate of transport from the force balance on a particle. The code was then validated with the experimental investigation. The equilibrium scour depth predicted by FANS3D show a good agreement with the measurements. The time scale of simulated scour is significantly greater than that of the experiment, however, which is attributed to the fact that the two-equation turbulence models underpredict the effect of turbulent horseshoe vorticity system (THSV).

Backfilling was induced by generating the equilibrium scour hole under $\boldsymbol{U}_{\boldsymbol{flood}}$, then transitioning the flow to $\boldsymbol{U}_{\boldsymbol{normal}}$. The equilibrium scour depths $\mathbf{z}_{\boldsymbol{eq,normal}}$ and $\mathbf{z}_{\boldsymbol{eq,flood}}$ were first obtained in a separate simulation for comparison. This step also served as a verification procedure, where the grid density and time step size were varied to determine the numerical solution's sensitivity to them. After observing the error to be insignificant, the cases associated with the low-density domain and the larger time step size were chosen as the references. It was found that the time to reach equilibrium under $\boldsymbol{U}_{\boldsymbol{flood}}$ is 60% of that for $\boldsymbol{U}_{\boldsymbol{normal}}$, while $\mathbf{z}_{\boldsymbol{eq,flood}}$ is greater than $\mathbf{z}_{\boldsymbol{eq,normal}}$ by 28.6% of D.

For both flows, in the early stages of scour, the sediment particles eroded from around the pier forms mound-like features downstream. The deposit continues to travel further downstream, until finally reaching the outlet boundary of the domain. With sustained flow, the holes grow in size mostly in the longitudinal direction, caused by extensive scour in the wake of the pier. While the equilibrium scour holes are of a similar

width, the boundary between the flat bed and the hole under the flood is located significantly further upstream.

From $\mathbf{z}_{eq,flood}$ of 70.4 cm, the scour depth is backfilled to 59.0 cm, which is within 5.8% of D from $\mathbf{z}_{eq,normal}$ of 56.1 cm. The backfilled depth equates to 22.8% of D. The duration of the backfilling, measured until the new equilibrium depth is reached, is ≈200 min. In addition, the location of the temporal maximum depth shifted from the upstream nose of the pier to $\boldsymbol{\Phi} = 56°$, which is equal to $\boldsymbol{\Phi}_{z,eq}$ under $\boldsymbol{U}_{normal}$.

This particular investigation has presented the following key contributions to the research community:

i. Backfilling around a vertical pier under a current-only flow was simulated for the first time, using the CFD tool FANS3D coupled with a sediment transport model.

ii. It was found that both the equilibrium scour depth and its location for a given unidirectional approach flow are independent of the initial bed morphology.

iii. Backfilling is observed to occur non-uniformly over the scour hole. Rather, in the present simulation, the upstream nose of the pier is backfilled first, followed by the range defined by $82° \leq \boldsymbol{\Phi} \leq 106°$. In the final stage of the process, $\boldsymbol{\Phi}_{\mathbf{z}}$ converges to the normal flow's $\boldsymbol{\Phi}_{z,eq}$.

iv. It was demonstrated that the initial rate of scour can be highest in the wake of the pier, supporting a previous experimental observation.

v. The time series of the scour around a pier under two different approach velocities are analyzed.

vi. The applicability of CFD to scour forecasting is proved. The output can be incorporated into existing scour evaluation tools, such as HEC-18 (Arneson et al., 2012) and the observation method for scour (OMS) (Briaud et al., 2009).

To improve this investigation, a realistic hydrograph can be adopted, instead of the idealized velocity changes used herein. Extending this work to other types of structures, such as abutments, would contribute to the engineering discipline as well.

5.4. Scour around Hybrid Support Structure for Offshore Wind Turbine

5.4.1. Introduction

With the growing interest in harnessing wind energy, increasing efforts are directed at developing and maintaining reliable offshore wind turbine structures (Kallehave et al., 2015; Rodrigues et al., 2015; Colmenar-Santos et al., 2016). Currently, most common types of structure used in wind energy operations are gravity-base foundations, monopiles, and tripods and jackets (Colmenar-Santos et al., 2016). Because these structures are constantly exposed to waves and currents in the sea environment, scour around them is of a great interest to the engineers.

However, most of the previous studies aimed at predicting and mitigating scour around wind turbine structures have been centered around cylindrical piles. Sumer et al. (1992) studied the time scale of scour around a vertical pile under current and waves through series of experiments. They concluded that under a wave condition, the Keulegan-Carpenter number and the Shields parameter dominate the time scale. Petersen et al. (2015) conducted laboratory and field investigations of scour around scour protections around piles in sea environment. It showed that the upstream and transverse perimeter undergo severe scour due to horseshoe vortex and flow acceleration. Baykal et al. (2017) simulated scour and backfilling around a circular pile in waves. It was found that the equilibrium depths are the same for the scour and backfilling processes for a given Keulegan-Carpenter number. A comprehensive study of the nature of scour development at offshore windfarm foundations by Whitehouse et al. (2011) was also limited to monopiles, although various scour protection methods were discussed in both cohesive

and non-cohesive beds. The focus on monopiles is likely to have been economy-driven, as exemplified by the fact that 75% of the offshore wind farms in Europe are supported by monopiles (European Wind Energy Association, 2012).

The goal of this investigation was twofold: to demonstrate the ability to perform CFD simulation for a hybrid offshore wind turbine support structure, and to study how its upper geometry, positioned away from the bed, affects the scour depth. Here, the term hybrid is used because the structure takes a form between the gravity-base and the jacket structures (Park et al., 2013), as depicted in Fig. 5.31.

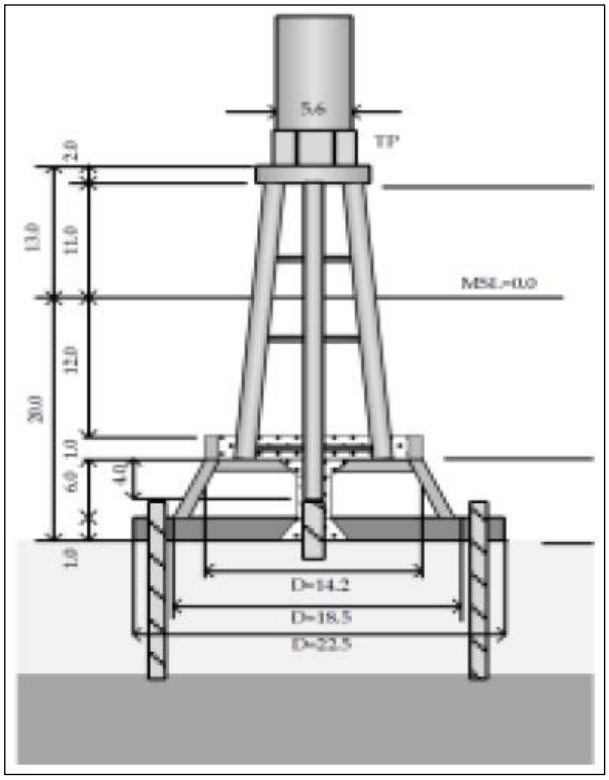

Fig. 5.31. Schematic of the hybrid structure (Lee et al., 2016).

As the Figure shows, the structure consists of three main components: (from bottom to top) a cylindrical disc, a base, and a jacket structure. The disc is held to the ground with suction piles. This design was developed and lab-tested with a 20:1 model at Korea Institute of Civil Engineering and Building Technology (KICT), with the goal to improve the structural dynamics in the coastal waters of Korea (Park et al., 2013; Lee et al., 2016).

Although the role of a cylindrical pier's diameter on the scour around it has been discussed extensively (Sumer and Fredsøe, 1992; Sumer et al., 1993; Ettema et al., 2006; Zhao et al., 2010; Arneson et al., 2012), to the best of the author's knowledge, the present investigation is the first one involving such a complex non-cylindrical structure.

5.4.2. Flow Environment

The CFD simulation was also conducted with the 20:1 model, with its geometry simplified to facilitate the investigation. Mainly, the disc was assumed to be extending far below ground, with no suction piles, and the jacket was replaced with a cylindrical shaft. For variability in the superstructure geometry, three different shaft diameters were adopted, defined as a percentage of the base's top diameter: 25% (Case A), 50% (Case B), and 75% (Case C), as depicted in Fig. 5.32.

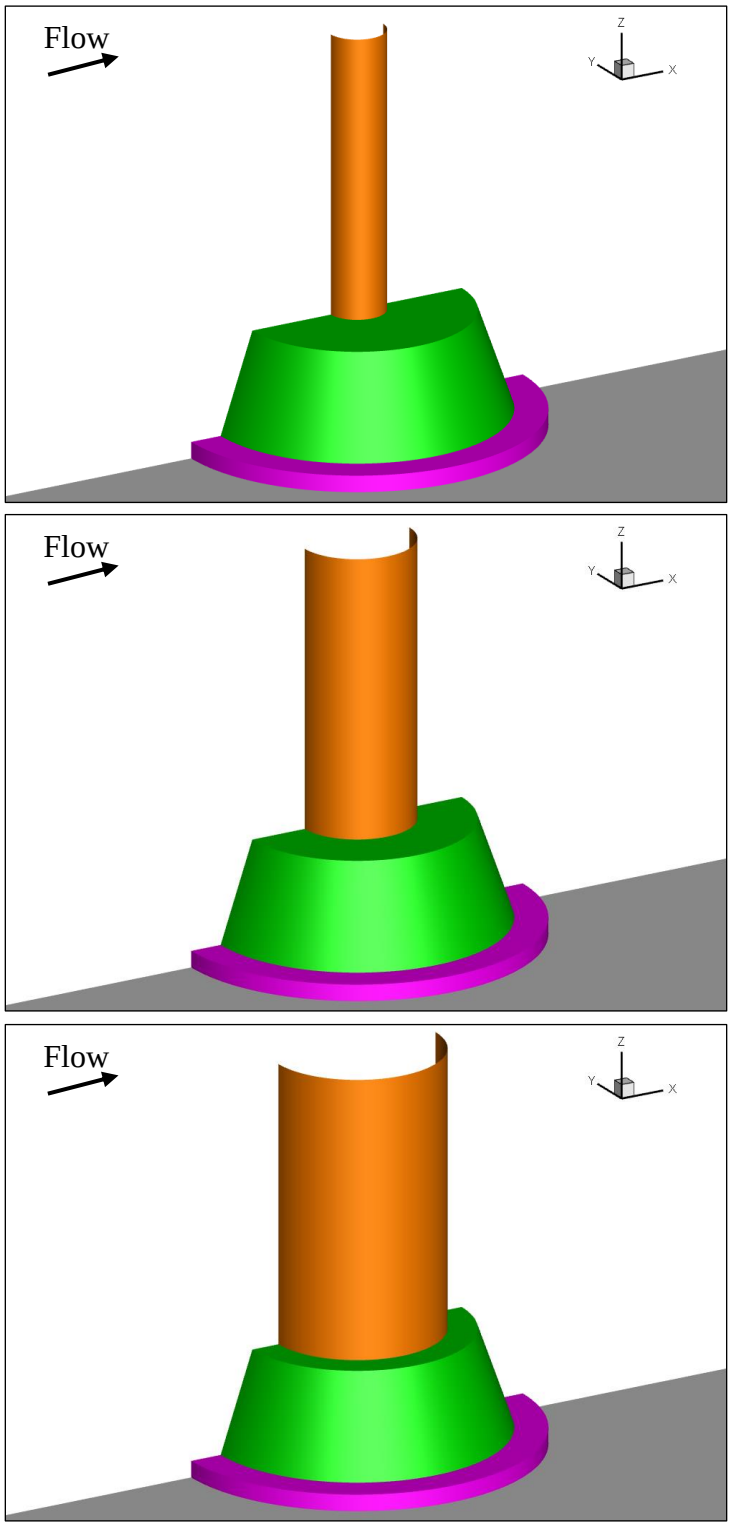

Fig. 5.32. Hybrid structure configuration for (from top to bottom) Cases A, B, and C.

The simplifications applied to the prototype may have consequences which do not exactly represent the physical processes occurring in the experiment or in the field. First, replacing the jacket with a single cylindrical superstructure will change the vortex structure around the structure and in its wake. Secondly, the assumption that the disc extends deep into the ground will prevent the flow and subsequent sediment transport which may occur below the structure as its bottom becomes exposed. However, the simplified geometry nevertheless captures the significant physical characteristics of the support structure, and it was deemed suitable for the investigation's focus. It must be remembered, however, that the decision to simplify the domain was made solely on pragmatic basis (e.g., to reduce time involved in pre- and post-processing, as well as computing), and it is actually possible to generate a mesh that represents the exact geometry of any physical structure using the overset grid technique.

The experimental flow conditions at KICT are summarized in Table 5.5 (obtained through personal communications with KICT personnel). The condition for Run 3 was chosen as the flow environment to be simulated. The selection was based on the fact that the water depth is the highest, corresponding to a high tide, and it was determined that the flow and scour simulation of this "demanding" condition would benefit the stakeholders the most.

Table 5.5. Flow conditions for the hybrid structure experiment.

Run	Flow Depth	Approach Velocity	Reynolds Number
1	0.159 m	0.4 m/sec	57,000
2	0.200 m	0.4 m/sec	71,000
3	0.241 m	0.4 m/sec	86,000

5.4.3. Mesh

The mesh employed a total of ten blocks for the simulation. The coordinate system used and the number of grid points for each block are presented in Table 5.6. The configuration of those surrounding the support structure is shown in Fig. 5.33. As can be seen, finer spacing was adopted near the wall surfaces for the wall function approach. Among those that conform to the surfaces, small blocks (Blocks 9 and 10) were placed to function as an "intermediary" between the other blocks, ensuring complete transfer of solutions.

The blocks associated with far-field flow are shown in plan-view in Fig. 5.34. The top surfaces of the disc and the base are colored magenta and green, respectively. As with the backfilling study discussed in Section 5.3., only half of the physical domain was simulated, since the time-averaged flow around a cylindrical structure is symmetrical. The Figure is used to show that the grid spacing, in general, expands gradually going from the immediate vicinity of the structure to the far-field.

Table 5.6. Mesh information for the hybrid structure simulation.

Block Number	Coordinate System	Number of Grid Points	Linked Blocks
1	Cylindrical	4,095	3,4
2	Cylindrical	20,475	9,3,10
3	Cylindrical	8,463	1,2,4,9,10
4	Cylindrical	97,643	1,3,5,6,7
5	Cartesian	19,575	4,7
6	Cartesian	19,575	4,7
7	Cartesian	30,885	4,5,6
8	Cylindrical	25,935	9
9	Cylindrical	30,576	2,3,8,10
10	Cylindrical	4,095	2,9,3

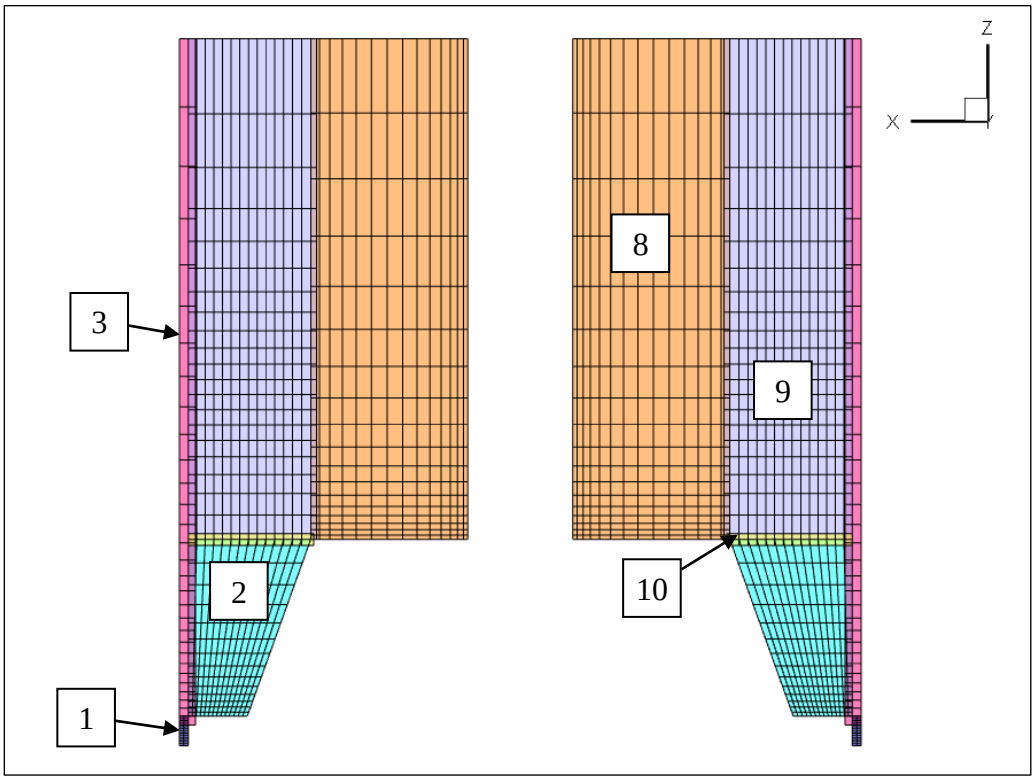

Fig. 5.33. Grid configuration of the blocks forming the turbine structure.

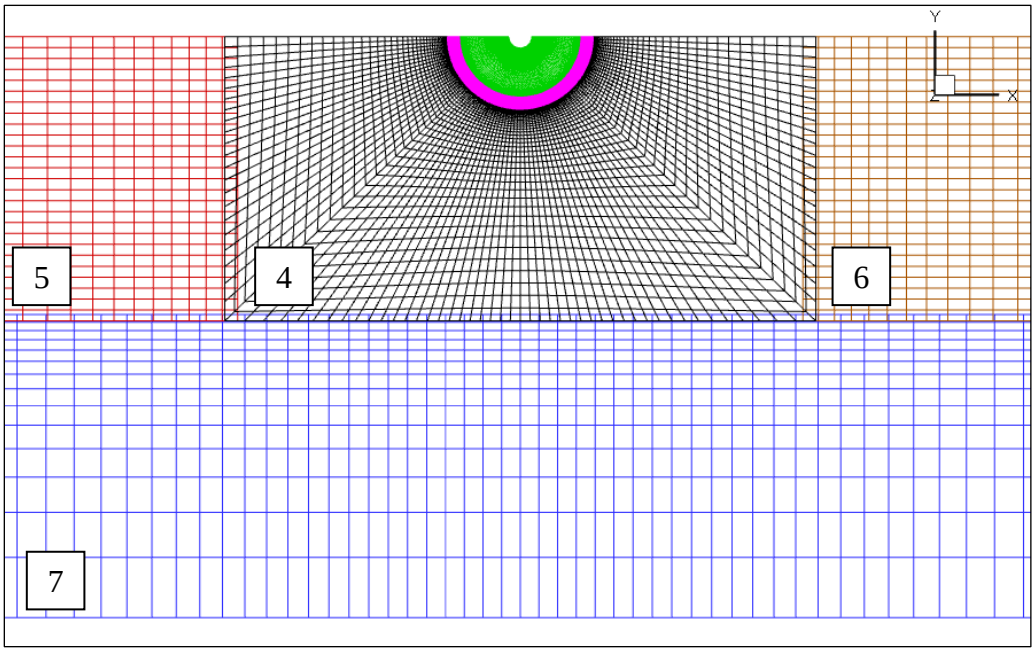

Fig. 5.34. Grid configuration of the far-field in plan view. Flow direction is from left to right.

5.4.4. Simulation Setup

The boundary conditions for the blocks associated with the far-field flow (blocks 4-7) were set such that the combined effect produced the boundary conditions appropriate for a rectangular channel (see Section 5.3). For other blocks, the wall function approach was taken to resolve turbulence and velocity near the surfaces. During bed load transport, PEGASUS was called every time step to update and maintain accurate interpolation scheme among the blocks.

5.4.5. Results and Discussion

The effect of different shaft diameter is first examined through the horseshoe vortex formations. The results are shown in Fig. 5.35 for all shaft diameters. Three different horseshoe vortices are observed, each forming at the upstream nose of the disc, base, and the shaft, separately. The most notable effect the shaft diameter had was the height of the horseshoe vortex forming at the base; as the shaft's diameter decreased, the vortex's height increased, as indicated in Fig. 5.35 with red arrows.

The general size of each of the vortices, however, varied according to the height of the obstruction providing the adverse pressure gradient; the smallest was observed in front of the disc, and the largest in front of the shaft. This trend was consistent among all three shaft diameters.

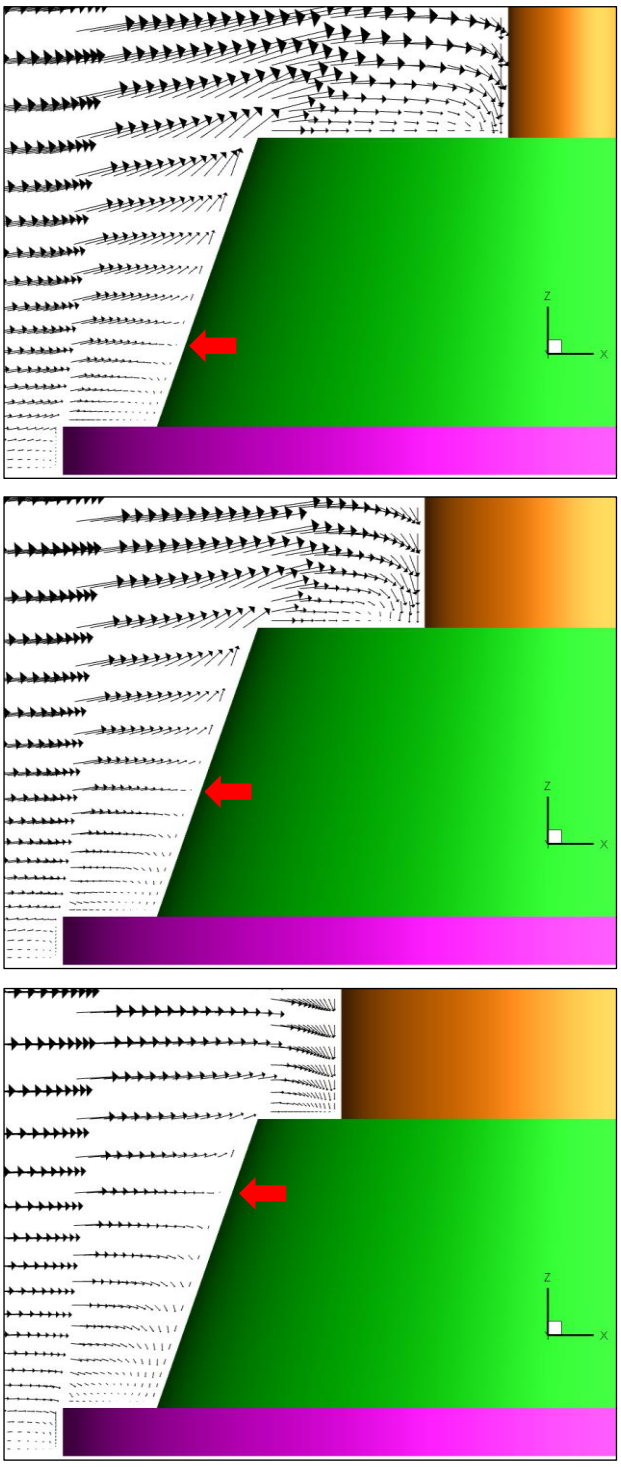

Fig. 5.35. Horseshoe vortex for each shaft diameter: (from top to bottom) Cases A, B, and C. The red arrow points to the height of the horse-shoe vortex. Flow direction is from left to right.

The shear velocity distribution, depicted in Fig. 5.36, shows that the vortices reach farther when the shaft is larger. More specifically, the regions of highest shear velocity (contours colored in orange and red) become larger. However, with increasing shaft diameter, the shear velocity is lower directly downstream and upstream of the structure. The explanations are as follows: the higher shear velocity on the side of the structure is caused by the flow being diverted against the obstruction; the lower magnitude in the upstream is due to the interaction between the approach flow and the backwash of the vortex; the downstream phenomena is due to flow separation and recirculation. The reader is reminded that because only the shaft's diameter is changing with the lower portion of the structure remaining unvaried, the physics established for flow around cylindrical piers cannot be directly applied.

The time series of the scour depth, presented in Fig. 5.37, shows that the larger shaft diameter in general produces deeper scour hole. The exception occurred during the time span between 130 min. and 290 min. when the scour depth for Case B was greater than that for Case C. However, after this brief period, the initial trend was restored and the larger diameter again generated greater scour depth. The overall tendency for a larger diameter to generate deeper scour hole is due to the increase in horseshoe vortex strength and shear velocity, and this is in agreement with previous findings with cylindrical piers (Sumer and Fredsøe, 1992; Sumer et al., 1993; Ettema et al., 2006; Zhao et al., 2010; Arneson et al., 2012).

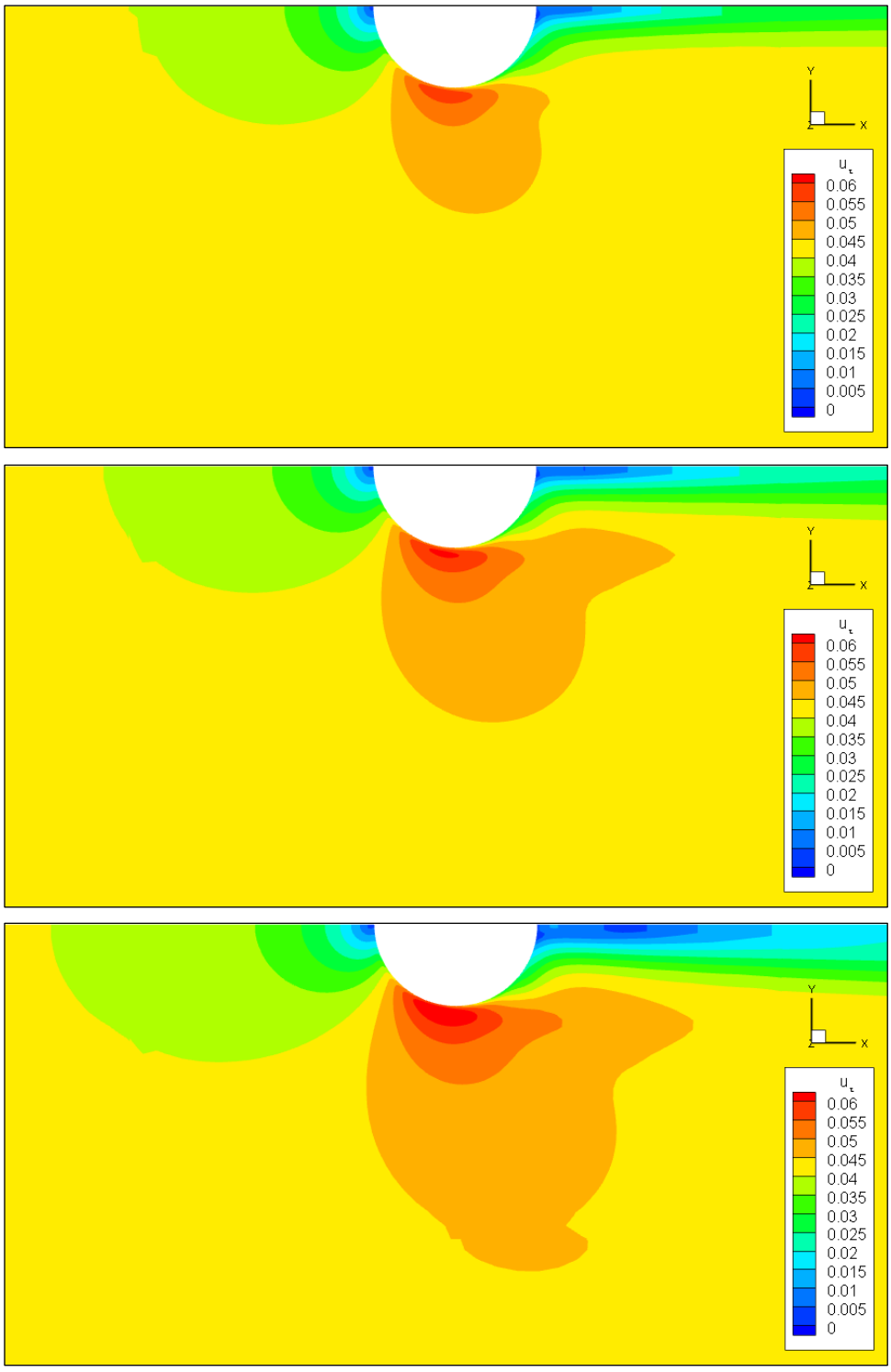

Fig. 5.36. Shear velocity contours: (from top to bottom) Cases A, B, and C. Flow direction is from left to right.

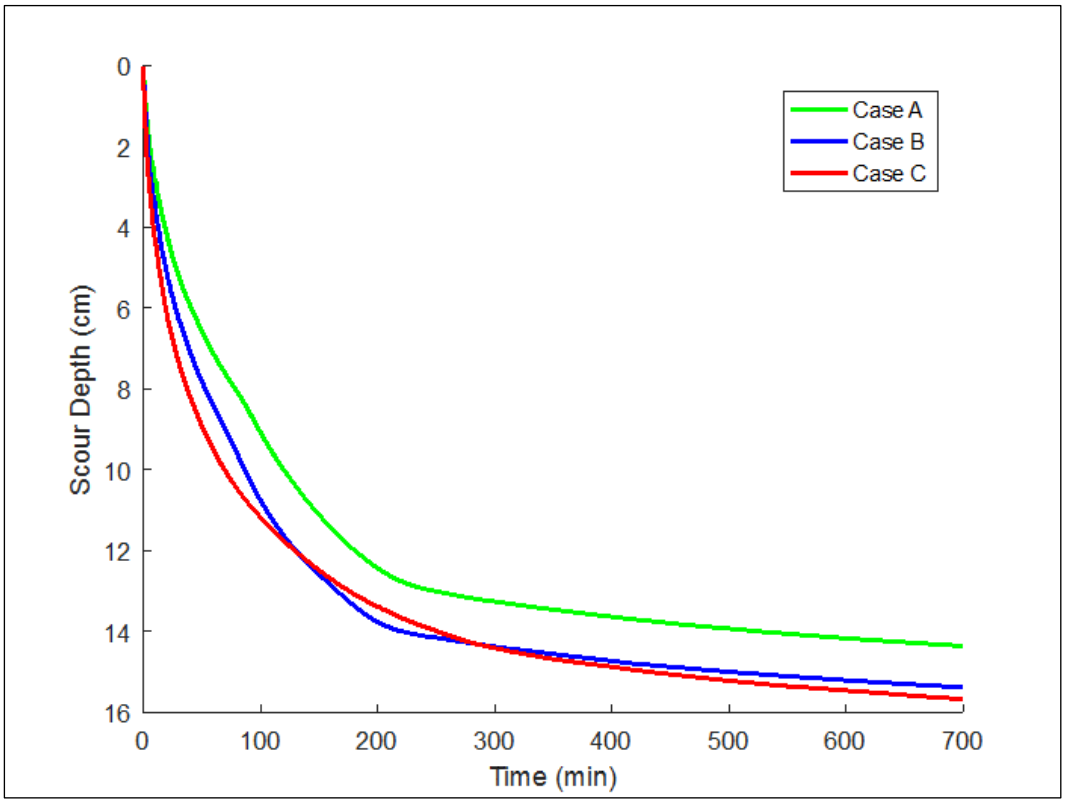

Fig. 5.37. Time series of scour depth around the hybrid structure.

The bed morphologies at t = 700 min. are presented in Fig. 5.38, showing the relationship between the shaft diameter and the scour hole shape. Increase in the shaft diameter resulted in not only a deeper scour hole, but also a larger one. In the Figure, the area of the scour hole is determined from the area inside of the boundary between the scour hole and the flat bed level (Scour = 0). The effect of the stronger wake vortex for Case C is easily seen with the more pronounced color contour for scour depth 6 cm-7 cm.

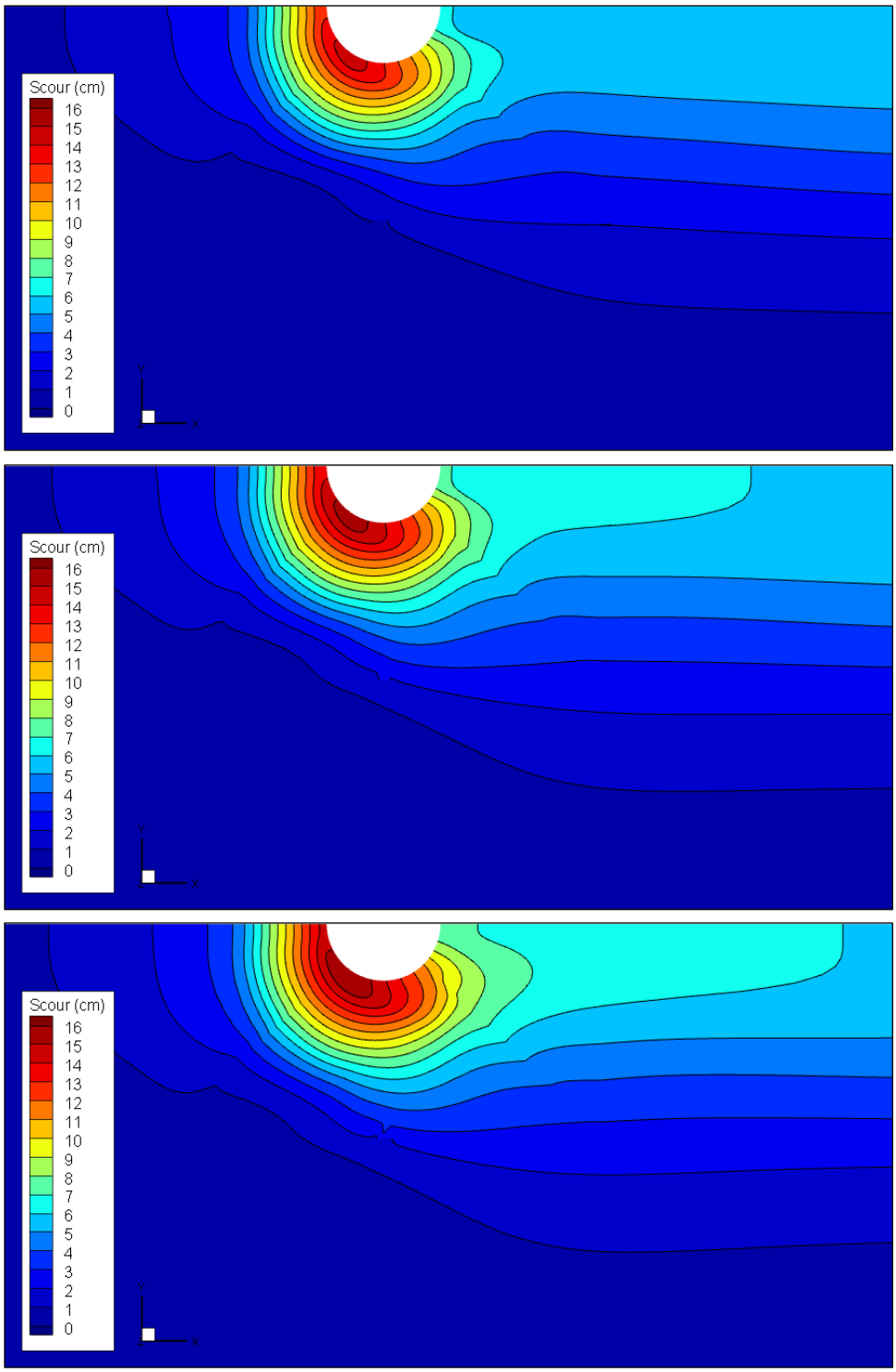

Fig. 5.38. Bed elevations at t = 700 min.: (from top to bottom) Cases A, B, and C. Flow direction is from left to right.

5.4.6. Conclusions and Future Works

This investigation showed that, for the present hybrid wind turbine support structure, larger shaft diameter leads to a deeper scour hole. The actual model's geometry was simplified using cylindrical components to facilitate simulation. An assumption was made on the scour environment as well (i.e., no sediment transport below the structure).

Regardless of the shaft diameter, horseshoe vortices formed in front of the vertical obstructions: the disc, the base, and the shaft. However, the height at which downward wash begins varied according to the shaft diameter. Also, larger shfat diameter generated higher shear velocity on the side of the structure, while lower values of shear velocity were observed immediately downstream and upstream. In summary, this investigation has made the following contributions to the research community:

i. The overset grid technique was employed to solve for the hydrodynamics and scour around a hybrid structure. The interpolation scheme was updated every time with PEGASUS.

ii. The effect of the shaft diameter on the vortex structures was analyzed. The fact that only the upper portion of the structure was varied, instead of the entire length, provides the novelty.

To further the understanding of flow and scour around such hybrid structures, following future studies are suggested:

i. Investigation on the effect of the base height on the scour processes. This will incorporate determining the threshold height over which varying the diameter of the shaft does not have any impact on the scour hole.

ii. Verification using different grid density and structures. In the present investigation, only one set of meshes were used, with the same number of grid points.

iii. Inclusion of a case where the shaft diameter equals that of the base. This was omitted in the present investigation because such geometry will inevitably require a considerably different grid structure.

Lastly, the author would like to acknowledge that part of the funding for this project was provided by KICT.

6. CONCLUSIONS

The CFD solver FANS3D was coupled with sediment transport models to develop a practical numerical tool, capable of simulating the physical processes in three dimensions. After validating the implementation against experimental measurements, the coupled solver was utilized to investigate several engineering problems involving transport of non-cohesive sediment as a plume or bed load. The overset grid technique was utilized with the pre-processor PEGASUS to generate CFD meshes for the complex flow domains.

The simulation of plume transport in channel bend using two different sediment diameters showed how the complex flow characteristics create zones where the sediment concentration is orders of magnitude higher than in the surroundings. Because of the settling velocity, the plume associated with the smaller diameter traveled considerably farther. In the case of scour around abutments, it was observed that although larger particles are heavier than the smaller ones, they can be more prone to incipient motion due to the increase in roughness. The third application proved that backfilling can occur if the approach flow velocity is high enough to cause particles to roll into an existing scour hole, but is below the critical threshold to bring the particles out of it. Lastly, the geometry of an offshore wind turbine support structure was varied to study its effect on the scour processes. The results show that the structure of the horseshoe vortex is affected even when the change is made far from the bed.

Nevertheless, the present numerical tool is without limitations. First, at the present state, it can only be applied to cases where the sediment is non-cohesive and homogeneous. Additional development is necessary to be able to simulate transport of mixed sediment types (e.g., mixture of clay and sand). Secondly, the current version neglects the effect of suspended sediment on bed elevation changes (see Section 5.1). Another assumption behind all applications presented herein are that the ambient fluid is fresh water. As the chemical and physical composition of water may affect the transport mechanism, attention must be given to the flow environment (e.g., salinity).

In summary, this dissertation presented interesting aspects of sediment mechanics through CFD. Through this effort, the capabilities of the newly coupled FANS3D and the applicability of the overset grid technique were demonstrated. Knowledge can be furthered, however, by implementing more advanced turbulence models or by considering larger scales, aided by parallel computing. In fact, the author intends to continue exploring sediment transport modeling through these and other new approaches and techniques.

REFERENCES

Adeel, M., Song, X., Wang, Y., Francis, D., and Yang, Y. 2017. Environmental impact of estrogens on human, animal and plant life: A critical review. *Environment International* 99: 107-119.

Ahmad, N., Bihs, H., Kamath, A. and Arntsen, Ø.A. 2015. Three-dimensional CFD modeling of wave scour around side-by-side and triangular arrangement of piles with REEF3D. *Proceedings of the 8th International Conference on Asian and Pacific Coasts*, Chennai, India.

Alberts, S., Fisher, P.L., Gibbes, B., and Grinham, A. 2015. Corals persisting in naturally turbid waters adjacent to a pristine catchment in Solomon Islands. *Marine Pollution Bulletin* 94(1-2): 299-306.

Amoudry, L.O., Hsu, T.-J., and Liu, P. L.-F. 2008. Two-phase model for sand transport in sheet flow regime. *Journal of Geophysical Research* 113, C03011.

Amoudry, L.O., and Liu, P.L.-F. 2009. Two-dimensional, two-phase granular sediment transport model with applications to scouring downstream of an apron. *Coastal Engineering* 56: 693-702.

Arneson, L.A., Zevenbergen, L.W., Lagasse, P.F., and Clopper, P.E. 2012. *Evaluating scour at bridges, fifth edition*, HEC-18, Report FHWA HIF 12-003, Washington, D.C., USA.

ASCE, 2013. *Report Card for America's Infrastructure (2013 Report Card)*. < http://www.infrastructurereportcard.org >.

Bagnold, R.A. 1956. The flow of cohesionless grains in fluids. *Royal Society of London Philosophical Transactions* 249(964): 235-297.

Baker, C.J. 1980. The turbulent horseshoe vortex. *Journal of Wind Engineering and Industrial Aerodynamics* 6: 9-23.

Barbhuiya, A.B., and Dey, S. 2004. Local scour at abutments: A review. *Sadhana* 29(5): 449-476.

Basser, H., Akib, S. Cheraghi, R., Karami, H., Jahangirzadeh, A., Amirmojahedi, M., and Naji, S. 2015. Experimental and numerical investigation of scour phenomena at rectangular bridge abutment. Scour and Erosion: *Proceedings of the 7th International Conference on Scour and Erosion*, Perth, Australia.

Bates, P.D., Lane, S.N., and Ferguson, R.I. 2005. *Computational Fluid Dynamics: Applications in environmental hydraulics*. John Wiley & Sons, West Sussex, England.

Baykal, C., Sumer, B.M., Fuhrman, D.R., Jacobsen, N.G., and Fredsøe, J. 2017. Numerical simulation of scour and backfilling processes around a circular pile in waves. *Coastal Engineering* 122: 87-107.

Benek, J.A., Dougherty, F.C., and Bunting, P.G. 1985. *Chimera: A Grid-Embedding Technique.* AEDC-TR-85-64.

Breusers, H.N.C., Nicollet, G., and Shen, H.W. 1977. Local scour around cylindrical piers. *Journal of Hydraulic Research* 15(3): 211-252.

Briaud, J.-L., Ting, F.C.K., Chen, H.-C., and Cao, Y. 2001. Erosion Function Apparatus for Scour Rate Predictions. *Journal of Geotechnical and Geoenvironmental Engineering* 127(2): 105-113.

Briaud, J.-L. 2006. *Erosion Tests on New Orleans Levee Samples*. Texas A&M University Internal Report.

Briaud, J.-L., Govindasamy, A.V., Kim, D., Gardoni, P., Olivera, F., Chen, H.-C., Mathewson, C., and Elsbury, K. 2009. *Simplified method for estimating scour at bridges*. Texas A&M Transportation Institute report to the Texas Department of Transportation, FHWA/TX-09/0-5505-1.

Briaud, J.-L. 2013. *Geotechnical engineering: unsaturated and saturated soils*. Wiley, Hoboken, NJ, USA.

Cebeci, T., and Bradshaw, P. 1977. *Momentum transfer in boundary layers*. Hemisphere, Washington, D.C., USA.

Chamoun, S., De Cesare, G., Schleiss, A.J. 2016. Managing reservoir sedimentation by venting turbidity currents: A review. *International Journal of Sediment Research* 31: 195-204.

Chapra, S.C. 2004. *Applied numerical methods*. McGraw-Hill, New York, NY, USA.

Chen, C.J., and Chen, H.C. 1984. Finite analytic numerical method for unsteady two-dimensional Navier-Stokes equations. *Journal of Computational Physics* 53: 209-226.

Chen, C.J., Bravo, R. H., Chen, H.C., and Xu, Z. 1995. Accurate discretization of incompressible three-dimensional Navier-Stokes equations. *Numerical Heat Transfer, Part B: Fundamentals* 27(4): 371-392.

Chen, C.R., and Chen, H.C. 2015. CFD simulation of bow and stern slamming on a containership in random waves. *International Journal of Offshore and Polar Engineering* 25(3): 185-193.

Chen, C.R., and Chen, H.C. 2016. Simulation of vortex-induced motions of a deep draft semi-submersible in current. *Ocean Engineering* 118: 107-116.

Chen, H.C., and Patel, V.C. 1988. Near-wall turbulence models for complex flows including separation. *AIAA Journal*, 26(6).

Chen, H.C., Patel, V. C., and Ju, S. 1990. Solutions of Reynolds-Averaged Navier-Stokes equations for three-dimensional incompressible flows. *Journal of Computational Physics* 88(2): 305-336.

Chen, H.C., and Korpus, R. 1993. A Multiblock finite-analytic Reynolds-averaged Navier-Stokes method for 3D incompressible flows. *Individual Papers in Fluids Engineering, edited by F. M. White, ASME FED-Vol. 150: 113-121, ASME Fluids Engineering Conference*, Washington, D.C., USA.

Chen, H.C. 2002. Numerical simulation of scour around complex piers in cohesive soil. *Proceedings of the First International Conference on Scour of Foundation*, College Station, Texas, USA.

Chen, X. 2008. *Numerical study of abutment scour in cohesive soils*. Ph.D. Dissertation, Department of Civil Engineering, Texas A&M University, College Station, Texas, USA.

Cheng, Z., Hsu, T.-J. 2014. *A multi-dimensional two-phase Eulerian model for sediment transport – TwoPhaseEulerSedFoam (Version 1.0)*. Research Report No. CACR-14-08, Ocean Engineering Laboratory, University of Delaware, Newark, Delaware, USA.

Colmenar-Santos, A., Perera-Perez, J., Borge-Diez, D., and de Palacio- Rodríguez, C. 2016. Offshore wind energy: A review of the current status, challenges, and future development in Spain. *Renewable and Sustainable Energy Reviews* 64: 1-18.

Dargahi, B. 1990. Controlling mechanism of local scouring. *Journal of Hydraulic Engineering* 116(10): 1197-1214.

Davies-Colley, R.J., and Smith, D.G. 2001. Turbidity, suspended sediment, and water clarity: A review. *Journal of American Water Resources Association* 37: 1085-1101.

Delft Hydraulics Laboratory. 1980. *Computation of siltation in dredged trenches: Mathematical model*. Report R 1267 V, Delft, The Netherlands.

Eckerle, W.A., and Langston, L.S. 1987. Horseshoe vortex formation around a cylinder. *Journal of Turbomachinery* 109: 278-285.

Engelund, F., and Fredsøe, J. 1976. A sediment transport model for straight alluvial channels. *Nordic Hydrology* 7: 293–306.

Escauriaza, C., and Sotiropoulos, F. 2011. Initial stages of erosion and bed form development in a turbulent flow around a cylindrical pier. *Journal of Geophysical Research* 116: F03007.

Ettema, R., Kirkil, G., and Muste, M. 2006. Similitude of large-scale turbulence in experiments on local scour at cylinders. *Journal of Hydraulic Engineering* 132(1): 33-40.

European Wind Energy Association. 2012. *The European offshore wind industry key 2011 trends and statistics*. < http://www.ewea.org >.

Finn, J. R., Li, M., and Apte, S. V. 2016. Particle based modelling and simulation of natural sand dynamics in the wave bottom boundary layer. *Journal of Fluid Mechanics* 796: 340-385.

Florida Department of Transportation. 2005. *Bridge Scour Manual*, Tallahassee, Florida, USA.

Fortunado, A.B., and Oliviera, A. 2007. Improving the stability of a morphodynamic modeling system. *Journal of Coastal Research, Special Issue* 50: 486 – 490.

Foti, S., and Sabia, D. 2011. Influence of foundation scour on the dynamic response of an existing bridge. *Journal of Bridge Engineering* 16(2): 295-304.

Fourtakas, G., and Rogers, B.D. 2016. Modelling multi-phase liquid-sediment scour and resuspension induced by rapid flows using Smoothed Particle Hydrodynamics (SPH) accelerated with a Graphics Processing Unit (GPU). *Advances in Water Resources* 92: 186-199.

Haun, S., Kjærås, S., Løvfall, S., and Olsen, N.R.B. 2013. Three-dimensional measurements and numerical modelling of suspended sediments in a hydropower reservoir. *Journal of Hydrology* 479: 180-188.

Hjelmfelt, A.T., and Lenau, C.W. 1970. Non-equilibrium transport of suspended sediment. *Journal of the Hydraulic Division, Proceedings of the American Society of Civil Engineers*, HY 7.

Hou, J., Li, Z., Liang, Q., Li, G., Cheng, W., Wang, W., and Wang, R. 2016. Effects of morphological change on fluvial flood patterns evaluated by a Hydro-geomorphological model. *Procedia Engineering* 154: 441-449.

Hsu, T.-J., Jenkins, J.T., and Liu, P.L.-F. 2003. On two-phase sediment transport: Dilute flow. *Journal of Geophysical Research* 108(C3), 3057.

Hsu, T.-J., Jenkins, J. T., and Liu, P. L.-F. 2004. On two-phase sediment transport: sheet flow of massive particles. *Proceedings of the Royal Society of London A* 460: 2223-2250.

Huang, K., Chen, H.C., and Chen, C.R. 2011. Numerical scheme for riser motion calculation during 3-D VIV simulation. *Journal of Fluids and Structures* 27(7): 947–961.

Hunt, B.E. 2009. *Monitoring scour critical bridges (NCHRP Synthesis 396),* Transportation Research Board, Washington, D.C., USA.

Jha, S. K., and Bombardelli, F. A. 2010. Toward two-phase flow modeling of nondilute sediment transport in open channels. *Journal of Geophysical Research* 115, F03015.

Jia, Y., Yichun, X., and Wang, S.S.Y. 2002. Numerical simulation of local scouring around a cylindrical pier. *Proceedings of the 1st International Conference on Scour of Foundations*, College Station, Texas, USA.

Kallehave, D., Byrne, B.W., Thilsted, C.L., and Mikkelsen, K.K. 2015. Optimization of monopoles for offshore wind turbines. *Philosophical Transactions of the Royal Society* A 373.

Kerssens, P. J. M., Prins, A., and van Rijn, L. C. 1979. Model for suspended sediment transport. *Journal of the Hydraulics Division, Proceedings of the American Society of Civil Engineers*, 105(HY5): 461-476.

Khosronejad, A., Kang, S., Borazjani, I., and Sotiropoulos, F. 2011. Curvilinear immersed boundary method for simulating coupled flow and bed morphodynamic interactions due to sediment transport phenomena. *Advances in Water Resources* 34: 829-843.

Khosronejad, A., Kang, S., and Sotiropoulos, F. 2012. Experimental and computational investigation of local scour around bridge piers. *Advances in Water Resources* 37: 73-85.

Kim, H., and Chen, H.C. 2014. Three-dimensional numerical analysis of sediment transport around abutments in channel bend. *Proceedings of the 34th International Conference on Coastal Engineering*, Seoul, Korea.

Koken, M., and Constantinescu, G. 2014. Flow and Turbulence Structure around Abutments with Sloped Sidewalls. *Journal of Hydraulic Engineering* 140(7).

Kulshreshtha, A., and Shanmugam, P. 2015. Estimation of Secchi transparency in turbid coastal waters. *Aquatic Procedia* 4: 1114-1118.

Kwan, R.T.F., and Melville, B.W. 1994. Local scour and flow measurements at bridge abutments. *Journal of Hydraulic Research* 32(5): 661-673.

Lança, R., Fael, C., and Cardoso, A.H. 2011. Effect of relative sediment size on clear-water equilibrium scour depth at single cylindrical piers. *Proceeding of the 34th IAHR World Congress*, Brisbane, Australia.

Lee, F.-Z., Lai, J.-S., Tan, Y.-C., and Sung, C.-C. 2014. Turbid density current venting through reservoir outlets. *KSCE Journal of Civil Engineering* 18(2): 694-705.

Lee, J.-H., Byun, N.-J., Kim, S.-H., Park, J.-H., and Kang, Y.-J. 2016. Experimental study for concrete base to sleeve connection of hybrid substructure for offshore wind turbine. *Journal of the Korea Academia-Industrial Cooperation Society* 17(1): 79-87 (in Korean).

Lee, S.O., and Sturm, T.W. 2009. Effect of sediment size scaling on physical modeling of bridge pier scour. *Journal of Hydraulic Engineering* 135(10): 793-802.

Lin, B., and Falconer, R.A. 1995. Modelling sediment fluxes in estuarine waters using a curvilinear coordinate grid system. *Estuarine, Coastal and Shelf Science* 41: 413:428.

Park, M.S., Jeong, Y.J., and You, Y.J. 2013. Numerical analysis of hybrid substructure with multi-cylinder for wind turbines. *The 2013 World Congress on Advances in Structural Engineering and Mechanics*, Jeju, Korea.

Mazumder, M.H., and Barbhuiya, A.K. 2014. Live-bed scour experiments with 45° wing-wall abutments. *Sadhana* 39: 1165.

Melville, B.W., and Chiew, Y.-M. 1999. Time scale for local scour at bridge piers. *Journal of Hydraulic Engineering* 125(1): 59-65.

Messer, W.C., Braune, G. M., and Menefee, F.N. 1916. Earth pressures: A practical comparison of theories and experiments. *Proceedings of the American Society of Engineers* 42(2): 191-221.

Muste, M., Yu, K., Fujita, I., and Ettema, R. 2005. Two-phase versus mixed-flow perspective on suspended sediment transport in turbulent channel flows. *Water Resources Research* 41, W10402.

Nordhaus, W.D. 2001. The progress of computing. *Cowles Foundation Discussion* Paper 1324.

Oh, S.J. 2008. *Experimental study of bridge scour in cohesive soils*. Ph.D. Dissertation, Department of Civil Engineering, Texas A&M University, College Station.

Olsen, N.R.B., and Melaaen, M.C. 1993. Three-dimensional calculation of scour around cylinders. *Journal of Hydraulic Engineering* 119(9): 1048-1054.

Olsen, N.R.B., and Kjellesvig, H.M. 1998. Three-dimensional numerical flow modeling for estimation of maximum local scour. *Journal of Hydraulic Research* 36(4): 579-590.

Pang, A.L.J., Skote, M., Lim, S.Y., Gullman-Strand, J., and Morgan, N. 2016. A numerical approach for determining equilibrium scour depth around a mono-pile due to steady currents. *Applied Ocean Research* 57: 114-124.

Petersen, T.U., Sumer, B.M., Fredsøe, J., Raaijmakers, T.C., and Schouten, J.-J. 2015. Edge scour at scour protections around piles in the marine environment – laboratory and field investigation. *Coastal Engineering* 106: 42-72.

Pontaza, J.P., Chen, H.C., and Reddy, J.N. 2005. A local-analytic-based discretization procedure for the numerical solution of incompressible flows. *International Journal for Numerical Methods in Fluids* 49(6): 657-699.

Pope, S.B. 2000. *Turbulent flows*. Cambridge University Press, Cambridge, UK.

Qi, Y., and Zhang, T.C. 2016. Transport of manure-borne testosterone in soils affected by artificial rainfall events. *Water Research* 93: 265-275.

Restrepo, J.D., Park, E., Aquino, S., and Latrubesse, E.M. 2016. Coral reefs chronically exposed to river sediment plumes in the southwestern Caribbean: Rosario Islands, Colombia. *Science of the Total Environment* 553: 316-329.

Rodrigues, S., Restrepo, C., Kontos, E., Pinto, R.T., and Bauer, P. 2015. Trends of offshore wind projects. *Renewable and Sustainable Energy Reviews* 49: 1114-1135.

Roulund, A., Sumer, B.M., Fredsøe, J., and Michelsen, J. 2005. Numerical and experimental investigation of flow and scour around a circular pile. *Journal of Fluid Mechanics* 534: 351-401.

Sheppard, D.M., Odeh, M., and Glasser, T. 2007. Large scale clear-water local pier scour experiments. *Journal of Hydraulic Engineering* 130(10): 957-963.

Shi, H., and Yu, X. 2015. An effective Euler-Lagrange model for suspended sediment transport by open channel flows. *International Journal of Sediment* Research 30: 361-370.

Shields, A. 1936. Anwendung der Aehnlichkeitsmechanik und der Turbulenzforschung auf die Geschiebebewegung. Mitteilungen der Preußischen Versuchsanstalt für Wasserbau (in German).

Simeonov, J.A., and Calantoni, J. 2012 Modeling mechanical contact and lubrication in direct numerical simulations of colliding particles. *International Journal of Multiphase Flow* 46: 38–53.

Suhs, N.E., and Tramel, R.W. 1991. *PEGASUS 4.0 User's Manual*. AEDC-TR-91-8.

Suhs, N.E., Rogers, S.E., and Dietz, W.E. 2002. PEGASUS 5: An automated pre-processor for overset-grid CFD. *32nd AIAA Fluid Dynamics Conference*, St. Louis, Missouri, USA.

Sumer, B.M., Christiansen, N., and Fredsøe, J. 1992. Time scale of scour around a vertical pile. *Proceedings of the 2nd International Offshore and Polar Engineering Conference,* San Francisco, USA.

Sumer, B.M., Christiansen, N., and Fredsøe, J. 1993. Influence of cross section on wave scour around piles. *Journal of Waterway, Port, Coastal, and Ocean Engineering* 119(5): 477-495.

Sumer, B.M., Petersen, T.U., Locatelli, L., Fredsøe, J., Musumeci, R.E., and Foti, E. 2013. Backfilling of a scour hole around a pile in waves and current. *Journal of Waterway, Port, Coastal, and Ocean Engineering* 139: 9-23.

Sumer, B.M., Baykal, C., Fuhrman, D.R., Jacobsen, N.G. and Fredsøe, J. 2014. Numerical calculation of backfilling of scour holes. *Proceedings of the 7th International Conference on Scour and Erosion*, Perth, Australia.

Sun, K., Gao, B., Zhang, Z., Zhang, G., Liu, X., Zhao, Y., and Xing, B. 2010. Sorption of endocrine disrupting chemicals by condensed organic matter in soils and sediments. *Chemosphere* 80(7): 709-715.

Sun, R., and Xiao, H. 2016. SediFoam: A general-purpose, open-source CFD-DEM solver for particle-laden flow with emphasis on sediment transport. *Computers and Geosciences* 89: 207-219.

Tonias, D.E., Zhao, J.J. 2007. *Bridge Engineering, 2nd edition*. McGraw-Hill Companies, New York, NY, USA.

van Rijn, L.C. 1981. *The development of concentration profiles in a steady, uniform flow without initial sediment load*. Report M1531, Part II, Delft Hydraulics Laboratory.

van Rijn, L.C. 1984. Sediment transport part III: Bed forms and alluvial roughness. *Journal of Hydraulic Division, Proceedings of the American Society of Civil Engineers* 110(12): 1733-1754.

van Rijn, L.C. 1987. *Mathematical modeling of morphological processes in the case of suspended sediment transport*. Delft Hydraulics Communication No. 382.

Villaret, C., and Davies, A.G. 1995. Modeling sediment-turbulent flow interactions. *Applied Mechanics Reviews* 48(9): 601–609.

Wang, Z.B., and Ribberink, J. S. 1986. The validity of a depth-integrated model for suspended sediment transport. *Journal of Hydraulic Research* 24(1): 53-67.

White, F. M. 2002. *Fluid Mechanics, 5th edition*, McGraw-Hill Education, New York, NY, USA.

Whitehouse, R.J.S., Harris, J.M., Sutherland, J., and Rees, J. 2015. The nature of scour development and scour protection at offshore windfarm foundations. *Marine Pollution Bulletin* 62(1): 73-88.

Wu, W, Rodi, W., and Wenka, T. 2000. 3D numerical modeling of flow and sediment transport in open channels. *Journal of Hydraulic Engineering* 126(1): 4-15.

Wu, W. 2008. *Computational River Dynamics*. Taylor and Francis Group, UK.

Zanke, U. 1977. Berechnung der Sinkgeschwindigkeiten von sedimenten, Mitt. Des Franzius-Instituts fuer Wasserbau, Heft 46, seite 243, Technical University, Hannover, Germany (in German).

Zhang, Y., and Jia, Y. 2013. Parallelized CCHE2D flow model with CUDA Fortran on Graphics Processing Units. *Computers and Fluids* 84: 359-368.

Zhao, M., Cheng, L., and Zang, Z. 2010. Experimental and numerical investigation of local scour around a submerged vertical circular cylinder in steady currents. *Coastal Engineering* 57: 709-721.